공학박사학위논문

Effects of the Space Characteristics of the Anode Materials on the High Performance of Lithium Ion Batteries under Fast Charging Conditions

음극재의 공간 특성이 리튬 이온 배터리의
고속 충전 조건에서의 성능 발현에 미치는 영향

2023년 2월

서울대학교 대학원
재료공학부
조 항 인

Effects of the Space Characteristics of the Anode Materials on the High Performance of Lithium Ion Batteries under Fast Charging Conditions

음극재의 공간 특성이 리튬 이온 배터리의
고속 충전 조건에서의 성능 발현에 미치는 영향

지도교수 박 종 래

이 논문을 공학박사 학위논문으로 제출함
2022년 10월

서울대학교 대학원
재료공학부
조 항 인

조 항 인의 박사학위논문을 인준함
2022년 12월

위 원 장 김 진 영 (인)
부 위 원 장 박 종 래 (인)
위 원 성 영 은 (인)
위 원 선 정 윤 (인)
위 원 김 태 훈 (인)

Abstract

Effects of the Space Characteristics of the Anode Materials on the High Performance of Lithium Ion Batteries under Fast Charging Conditions

Hang In Cho

Department of Materials Science and Engineering

The Graduate School

Seoul National University

Developing high-performance energy-storage systems has been considered key to efficiently store and manage energy to replace fossil fuels due to severe global environmental issues, such as air pollution, climate change and resource depletion. Among the various energy storage systems, an electrochemical energy storage represented by a lithium ion secondary battery is the most widely researched field due to its diverse applications. However, at the crossroads from small electronic devices such as smartphones to enormous electric-storage stations and electrical vehicles, fast charging, which supplies a higher capacity in a shorter time, is one of the most significant issues to solve. Especially in fast charging conditions, the electrochemical performance degrades more at the anode due to the various kinetic limits of

electrochemical species in the active material. Graphite, which has been widely used as anode material so far, has the disadvantages of a poor rate capability and cycle stability under fast charging conditions due to a slow solid-state diffusion, high tortuosity, and various side effects by a low redox potential. Therefore, there have been numerous efforts to develop an anode material for maintaining high electrochemical performance under fast charging conditions.

Part I provides a general review of energy storage materials and previous strategies on achieving high electrochemical performance under fast charging conditions. Current issues to solve were derived from state-of-the-art works and re-interpreted in terms of the electrochemical reaction between the electrochemical species and the anode material under fast charging conditions. Carbon nanofibers (CNFs) were introduced as an efficient 1D anode material to resolve the kinetic limits, and the ideal morphology of the CNFs to enhance the transport characteristics of the electrochemical species was proposed from the viewpoint of introducing various “spaces” within the anode material. By revisiting the fundamentals and necessities, the aim and scope of this study were derived.

Part II presents theoretical developments to rationally design fast-electrochemical species transportable CNFs. The dynamic size of the electrochemical species, especially solvated Li-ions under the fast charging condition, was calculated. Furthermore, the size and accessibility of the space where solvated Li-ions transport through are discussed in an effort to enhance the transport characteristics, finding the correlation between the state of the electrochemical species under fast charging conditions and the space characteristics of the active material.

Part III focuses on the rational design and synthesis of CNFs according to the theories presented

in Part II and verifies the theory by deriving the correlation between the space characteristics, the transport characteristics, and the electrochemical performance. Chapter 3 introduces immiscible polymer blend electrospinning to develop a fast electrochemical species transportable space such as ion channels and pores within CNFs. Phase separation behaviors are predicted with the ternary phase diagram based on the Flory-Huggins interaction parameter, and the space characteristics for fast solvated Li-ion transport is designed by interpreting the corresponding phase morphologies. A facile phase separation method to make solvated Li-ion transport channels with an immiscible polymer blend electrospinning system was investigated, and furthermore, the correlation between the space characteristics and the solvated Li-ion transport characteristics was derived to provide guidelines for designing anode materials suitable for fast charging.

In Chapter 4, N-doped hierarchical porous carbon with uniaxially packed carbon nanotubes (CNTs) was prepared, expanding the effect of the space characteristics from fast solvated Li-ion transport to rapid electron transport and subsequent maximized electrochemical reaction. The space characteristics of the anode material is hierarchically modified from developing a core-shell transport channel to a KOH activated lithiophilic surface finding the correlations with the electrochemical performance under fast charging condition. In addition, the effect of the CNTs was investigated from a new perspective on modifying the space characteristics of the anode materials and improving electrical conductivity.

Part IV suggests perspectives on fast charging anode materials and future energy storage devices as concluding remarks.

In summary, this study presented anode material design guidelines for the fast charging condition through theoretical studies and correlations between variables related to the electrochemical performance. CNFs, which guarantee fast ion and electron transport, were

successfully prepared, and the correlation between the actual space characteristics and the transport characteristics, and the effect on electrochemical performance were verified. The material design guidelines presented in this study have great academic and practical significance in researching next-generation energy storage materials that can overcome the gap between theoretical and practical energy storage performance under fast charging conditions and improve electrochemical performance.

Keywords: Energy storage materials, Electrochemistry, Batteries, Electrospinning, Phase separation, Carbon nanofiber

Student Number: 2015-20864

Contents

List of Figures

List of Tables

Part I. General Introduction

Chapter 1. Introduction

1.1 General introduction to electrochemical energy storage

1.1.1 Overview of electrochemical energy storage

Developing high-performance energy-storage systems has been considered as an important issue to efficiently store and manage energy to replace fossil fuels due to severe global environment issues, such as air pollution, climate change and resource depletion (Fig. 1.1). Among various energy storage systems, an electrochemical energy storage represented by lithium ion secondary battery is most widely researched field due to its diverse application. Electrochemical energy storage is an efficient method to store electrical energy by converting it into a chemical form, since both electrical and chemical energy utilize the electron as the same carrier. Therefore, research into the electrochemical energy storage has dramatically expanded during the past decades.

Figure 1.1 Global issues including global warming, air pollution and environmental pollution

1.1.2 Demand of fast charging anode materials for next-generation batteries

Rechargeable batteries have been widely used in mobile devices and changed the technology landscape. At the crossroads from small electronic devices such as smartphones to enormous electric-storage stations and electrical vehicles (Fig. 2.2), the next-generation battery materials require both high energy density and power density. Therefore, it is urgently needed to develop high performance energy storage material which satisfy the requirement of next targeted applications such as grid energy storage and electrical transportation fields (EV, HEV). Furthermore, considering the energy density of next-generation batteries, fast charging, which supplies a higher capacity in a shorter time, is one of the most significant issues to replace the existing energy storage systems efficiently.

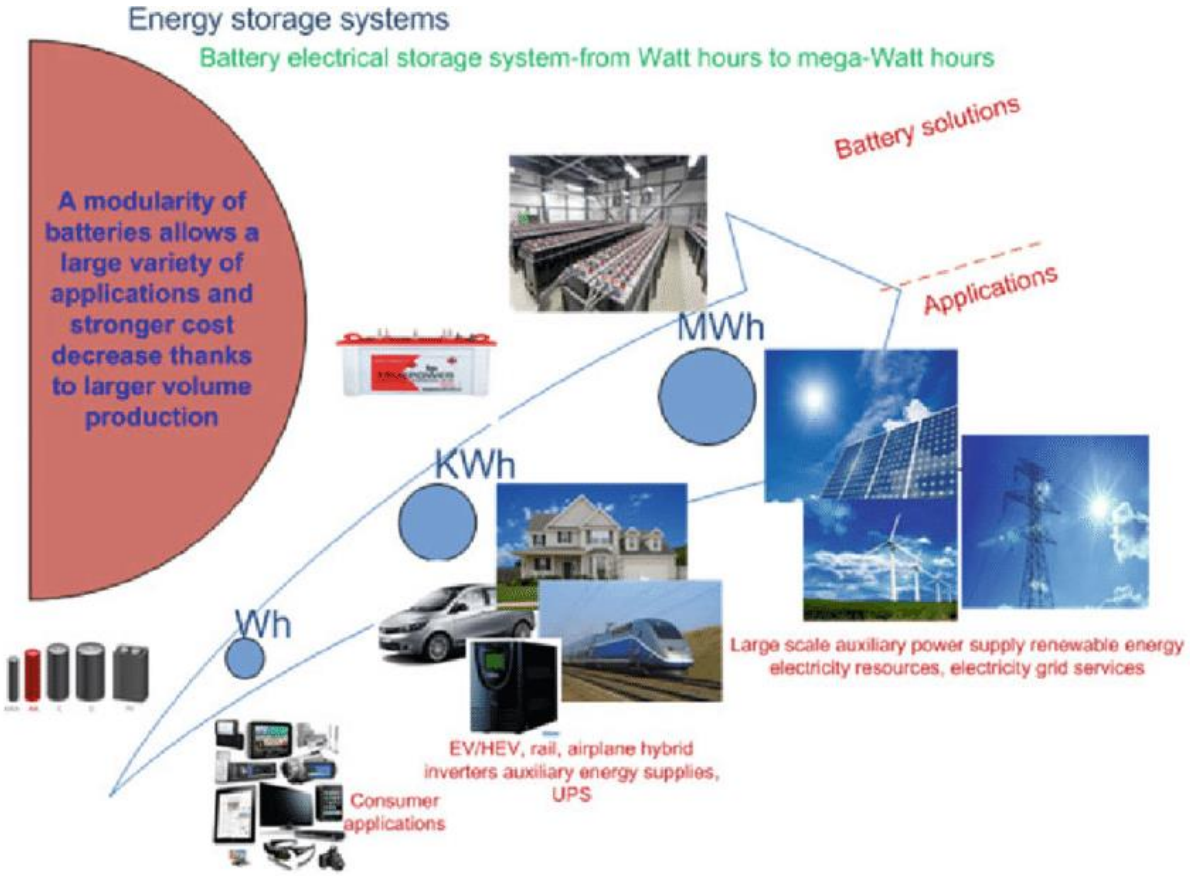

Figure 1.2 Next target of electrochemical energy storage systems and applications [1]

1.2 Performance parameters in electrochemical energy storage

1.2.1 Capacity

The capacity (Q) is total charge stored in an active material, which can be calculated by the total amount of charge per unit mass of the electrode material theoretically.

$$Q = \frac{nF}{3.6M} \text{ [mAh g}^{-1}\text{]}$$

(n is the number of charges, F is the Faraday constant)

1.2.2 Energy density

The energy density (ED) is the amount of energy stored in an active material per unit volume or mass. The energy stored in an electrochemical system can be calculated by the product of capacity and voltage. Since the voltage (V) is changed by the degree of charge/discharge state, the energy density is determined by the area of voltage profile according to capacity.

For volumetric energy density (Wh L^{-1})

$$\text{ED} = \frac{\int V dq}{Vol.}$$

For gravimetric energy density (Wh kg^{-1})

$$\text{ED} = \frac{\int V dq}{M}$$

1.2.3 Power density

The power density of electrochemical energy storage system refers to "how fast energy can be stored per unit time". The power density (PD) is a product of operating current and voltage divided by volume or mass.

For volumetric power density (W L^{-1})

$$\mathrm{PD} = \frac{VI}{Vol.}$$

For gravimetric power density (W kg^{-1})

$$\mathrm{PD} = \frac{VI}{M}$$

Power density is closely related to the kinetics of the electrochemical energy storage since it is the energy transfer rate. Therefore, it is crucial to design the active materials to maintain high energy density at high operating currents, under the fundamental understanding of the fast charging/discharging conditions.

1.3 Rational design of anode active material for fast charging conditions

Because there are increasing demands for high-power driven applications such as electrical vehicles (EVs) and energy storage systems, there have been tremendous efforts to achieve an efficient energy storage ability with both a high specific capacity and rate capability in lithium-ion battery materials (Fig. 1.3) [2-5]. Among the various requirements for next-generation batteries, fast-charging without capacity decay and stable cycle stability are two of the most important issues to solve [6]. The U.S Department of Energy (DOE) requires a fast charging condition, providing a 10~15 minute (4~6 C) charging time with 180 Wh kg^{-1} for achieving a full charge state and 80% cycle stability at 500 cycles in EVs [6-8]. Under the fast charging condition with a high current density, anode areal capacity decay is much higher than that of the cathode due to various kinetic issues (Fig. 1.4) [9]; therefore, it is more important to overcome the electrochemical performance degradation of the anode material.

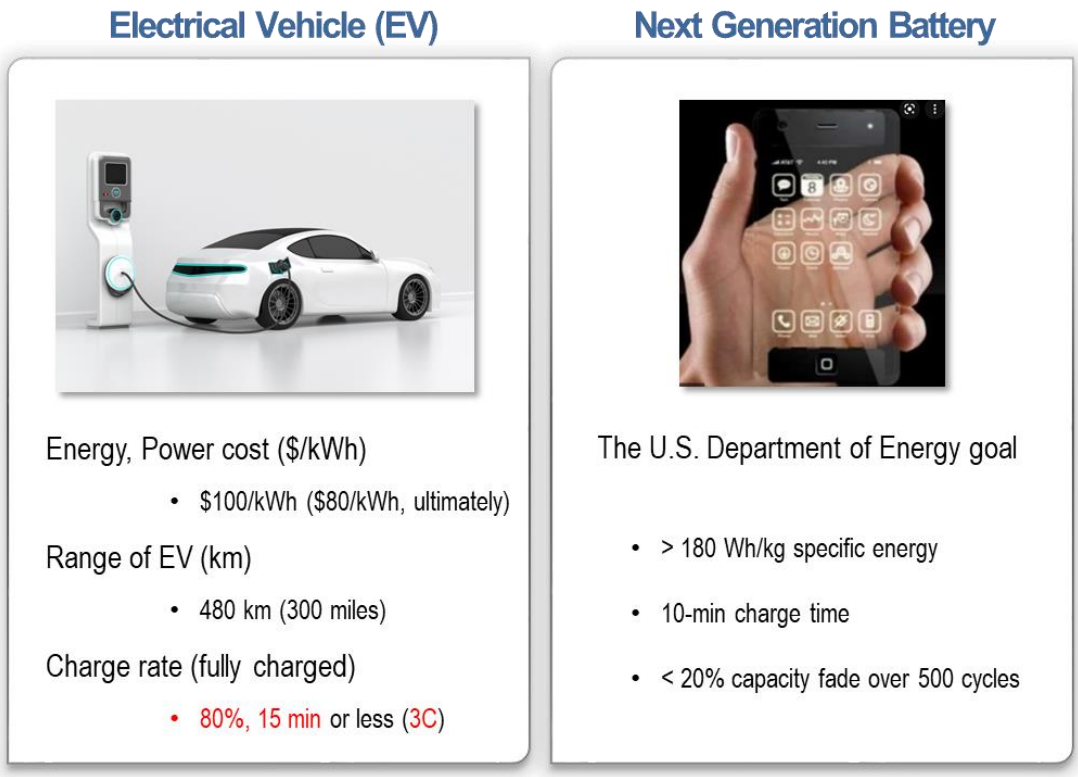

Figure 1.3 DOE target of next generation batteries

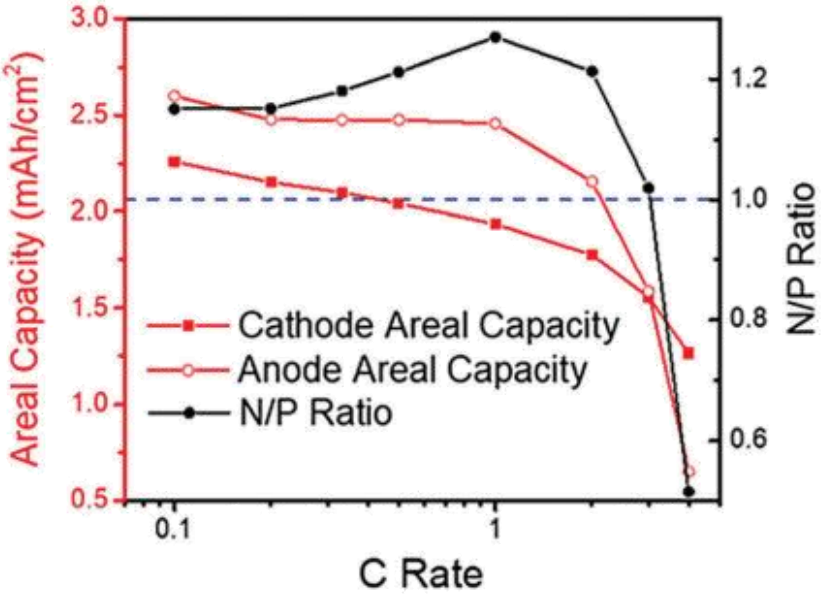

Figure 1.4 Anode areal capacity degradation is severe than the cathode areal capacity as C-rate increases [10]

However, graphite, which has been dominantly used as an anode material, shows a poor rate capability and cycle stability under fast charging conditions due to its slow solid-state diffusion, high tortuosity, and various side effects by its low redox potential [11]. Therefore, there have been numerous efforts to develop anode material for maintaining high electrochemical performance under the fast charging conditions. For example, other carbonaceous materials such as graphene composite materials, carbon nanotubes (CNTs) composite, carbon nanofiber (CNF) were anticipated to replace graphite for a fast charging anode material. Among various carbonaceous anode material, 1-dimensional (1D) carbonaceous material has both fast ion (referred as diffusion coefficient) and electron (referred as charge transfer resistance) transport due to its dimensional advantages such as high aspect ratio, high surface area, open structure for fast electron transport, shortened ion transport pathway (State-of-the-art is summarized in Fig. 1.5).

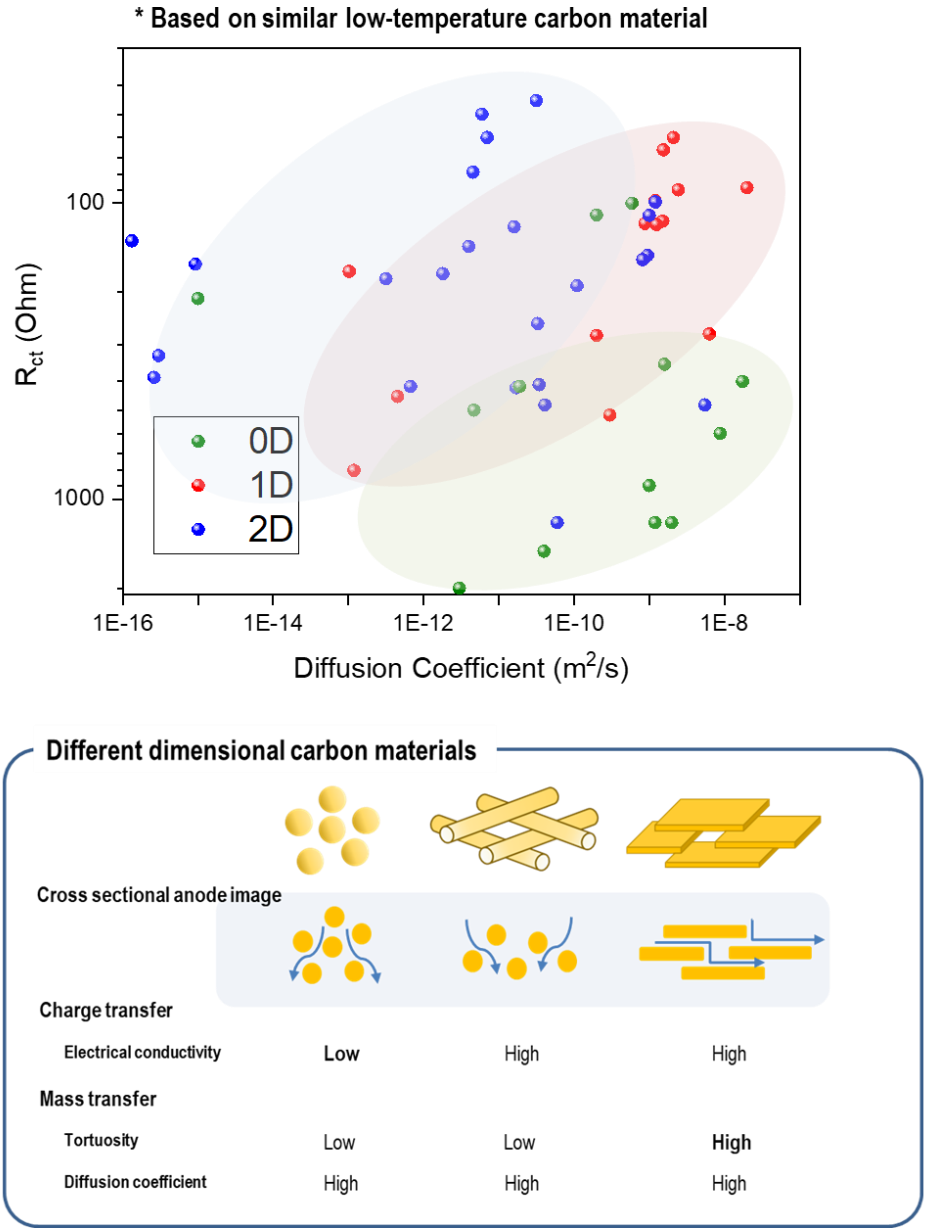

Figure 1.5 Summarized State-of-the-art of charge transfer resistance and diffusion coefficient of different dimensional carbonaceous material.

1.3.1 State-of-the-art of porous carbon nanofibers based anode materials for electrochemical energy storage

Among 1-dimensional (1D) carbonaceous materials, porous carbon nanofibers (PCNFs), which have been modified with various types of spaces (pores, channels, and voids) on CNFs, have many advantages such as a fast electron conductive 3D network, fast Li^+ ion-transport channel [12, 13], high surface area of space with facile electrolyte penetration and low tortuosity [14, 15] making it a good candidate for a fast charging anode material (Fig. 1.6). These 1D PNCF can be prepared by a variety of methods with various morphology and space types.

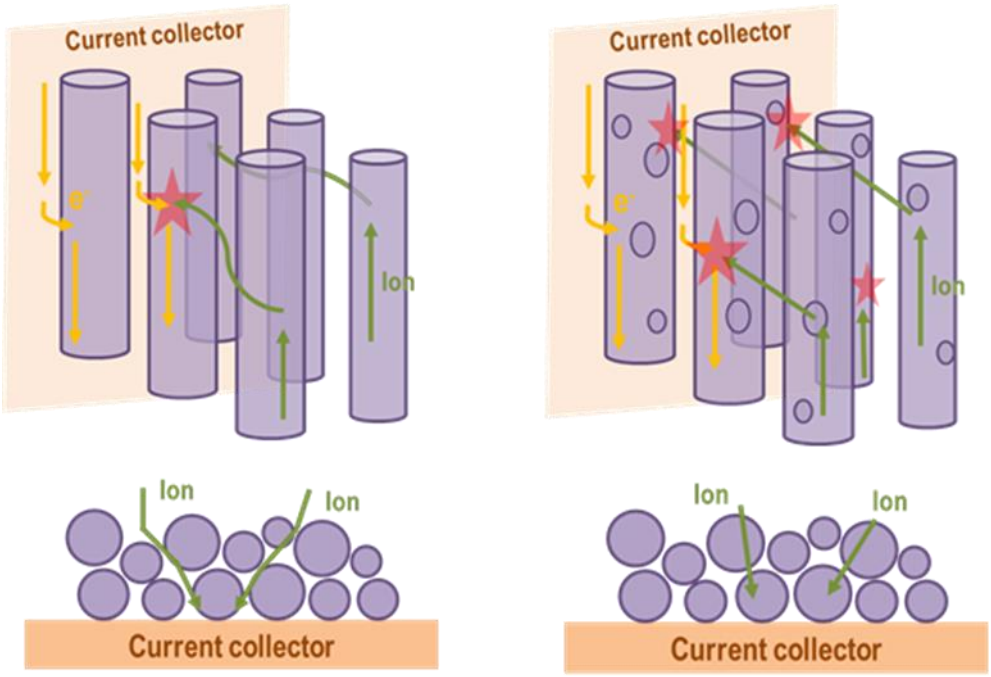

Figure 1.6 Comparison between non-porous CNF and porous CNF

1.3.1.1 Microporous carbon nanofibers

One of the most common methods to prepare porous carbon nanofibers is the activation method, which involves either a physical or chemical activation method. After activation, the nanofibers have abundant micropores and a large surface area, which is favorable for Li-ion storage (Fig. 1.7). The physical activation method generally uses oxidizing gases such as CO_2 and air to react with carbon, compared with chemicals such as $Zncl_2$ and KOH for the chemical activation method. The as-obtained activated porous carbon nanofibers are stimulated to have surface oxygen functional groups and a high specific surface area up to 1~2000 m^2g^{-1} depending on the activation method and temperature [16-18]. This is apparently helpful for maximizing the capacitive storage behavior due to the enlarged number of redox sites at the normal charging condition. However, pores derived from the activation process are mainly confined to micro-size ones, which are too small for fast electrolyte penetration. Furthermore, those micropores are located mainly on the surface of nanofibers; subsequently, it is hard to utilize the inner part of the CNFs. The lack of various sizes of pores could lead to a severe degradation in electrochemical performance under the fast charging condition, which requires fast electrolyte penetration and rapid utilization of the whole part of the active material [19].

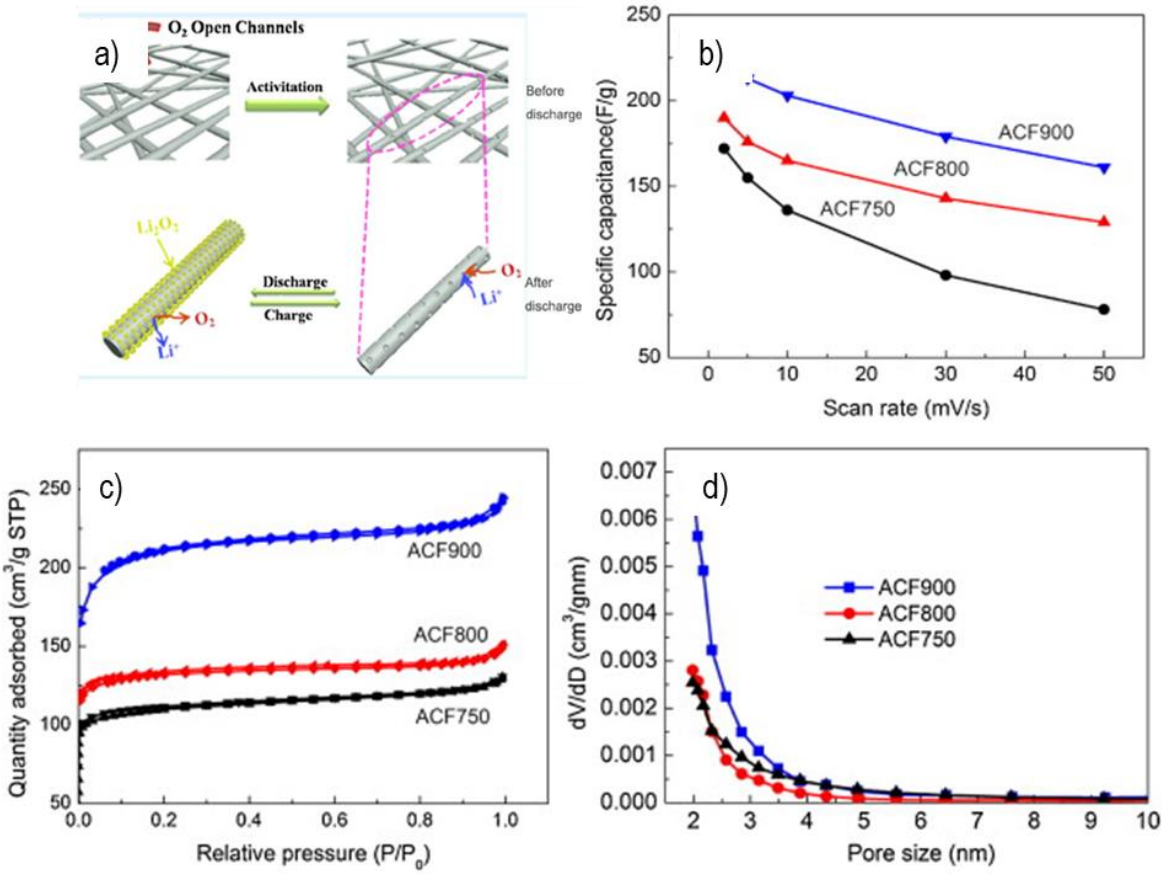

Figure 1.7 a) Schematic illustration of a CO_2-activated carbon nanofibers network b) specific gravimetric capacitance as a function of the voltage scan rates; c) nitrogen adsorption and desorption isotherms and d) pore size distributions [19]

1.3.1.2 Mesoporous carbon nanofibers

The requirements of a fast electrolyte penetration space, ion transport channel, and additional space to embody other nanomaterials for enhancing the electrochemical performance have brought about the necessity to adopt a larger size of pore (Fig. 1.8) [20, 21]. Especially, relatively large mesopores on CNFs are anticipated to have both the advantages of a fast 1D electron transport path and a short Li-ion transport path due to the adoption of an electrolyte containing porous space. Various morphologies exist such as mesoporous hollow carbon nanofibers [22] (Fig. 1.9) and template-based mesoporous carbon nanofibers [23, 24]. As the size of the pore (space) present in the carbon nanofibers increases, the space can infiltrate more electrolyte into the inner part of the active material, enhancing the interfacial area between the electrolyte and the active material. Subsequently, Li-ion transport can become low-tortuous and be shortened, which is beneficial for an effective ion conduction and redox reaction.

a)

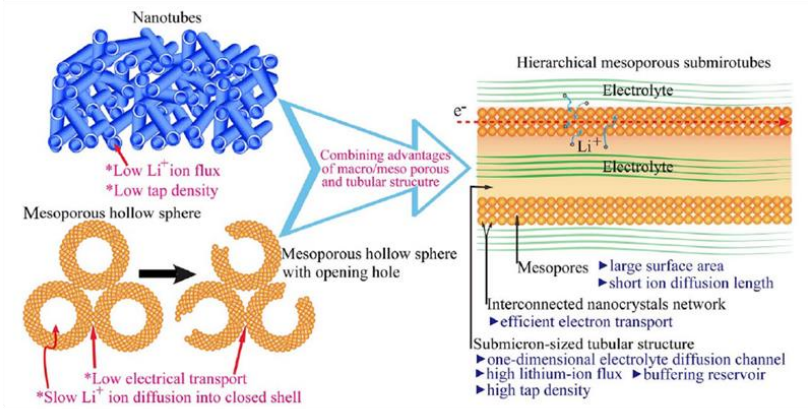

b)

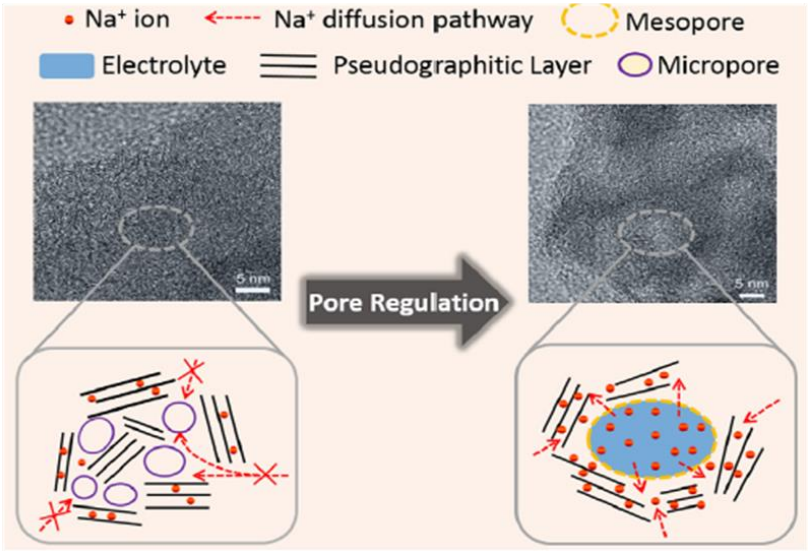

Figure 1.8 a) Mesoporous hollow sphere act as reservoir of electrolyte for large ion flux to active sites [21]; b) mesopore provide fast electrolyte penetration and subsequently facilitate ion to reach carbon interlayers [20]

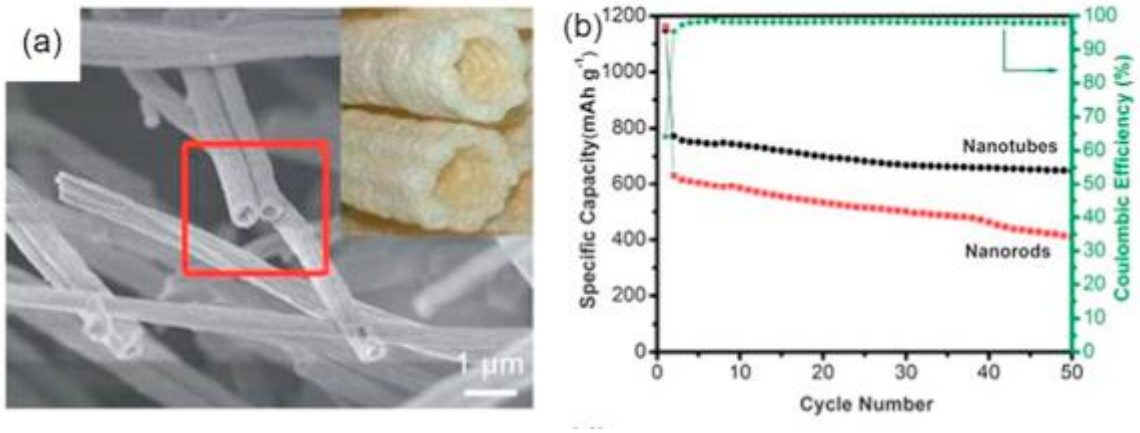

Figure 1.9 a) SEM image of hollow nanofibers, b) Capacity and Coulombic efficiency versus cycle number of the nanomaterials (current density = 60 mA g^{-1}) [22]

To examine the size effect of the pore on the electrochemical performance, I derived the parameter ‘critical pore diameter;’ it is the specific pore diameter of a sample with the highest rate capability and ‘current density,’ which is the current density before the rate capability decreases below 40% from previous PCNF based researches (Fig. 1.10). In the normal charging condition under approximately 1000 mA/g, small micropores could act as critical pores to enhance the performance. However, under the fast charging condition, studies that have showed superior rate capabilities suggested that pores whose sizes were larger than 10 nm are the critical pore, which is larger than the existing standard for the mesopore size. Furthermore, not only the size of the pore, but also other morphological characteristics of the pore, which will be introduced as the space characteristics in this study, also affect the electrochemical performance of the PCNFs.

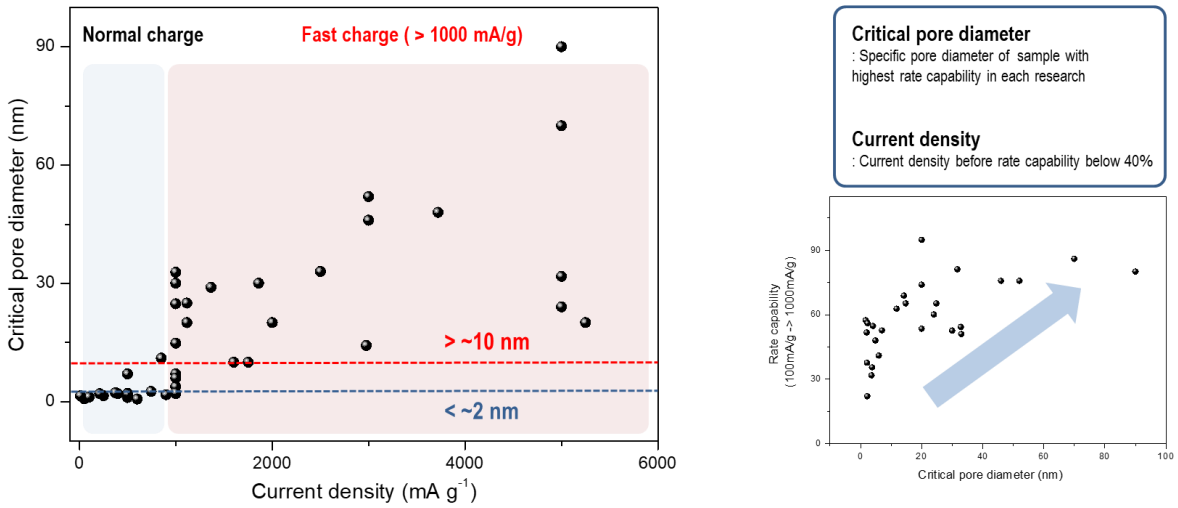

Figure 1.10 Summarized state-of-the-art: Critical pore diameter according to current densities and subsequent rate capabilities

1.3.2 Performance gap between normal and fast charging conditions

However, despite the high performance in normal charging conditions, these materials still did not maintain a high performance even under a fast charging condition. In fast charging conditions, morphological characteristics such as various spaces adopted to modify the CNFs cannot act as the intended role as in normal conditions [25]. This difference in the charging rate should be considered because electrochemical species can transport differently in the space of the PCNFs according to the charging conditions. Therefore, the rational design of a fast-charging PCNF anode material requires a fundamental comprehension of the effect of the space characteristics on the transport characteristics of electrochemical species (ion, electron) and electrochemical performance.

1.4 Aim and scope of this research

In this study, I revisited the fundamentals of the transport characteristics of electrochemical species under fast charging conditions in terms of the correlation with the space characteristics of anode materials. Part II presents the kinetic limits that occur by the transport of electrochemical species under fast charging conditions as the overpotential in a battery system. Fundamental studies devised a method to improve the transport characteristics of the electrochemical species by modifying the space characteristics, and ultimately lowering the overpotential of the system to maintain a superior electrochemical performance even under fast charging conditions. The ideal morphology for a fast charging anode material was suggested to be 1D carbon nanofibers, and a subsequent electrospinning method to design CNFs with an ion-transportable space was investigated with interpretation of the phase separation behavior. As a result, a guideline was derived for a fast electrochemical species transportable anode material for various electrochemical energy storage devices. Part III focuses on the rational design and synthesis of CNF based anode materials according to the guidelines presented in Part II. The importance of controlling solvated Li-ion transport in the space within the CNFs was presented to reduce the overpotential during the fast charging, and a facile phase separation method to form fast ion transport channels with an immiscible polymer blend electrospinning system was investigated through the interpretation of the ternary phase diagram. Furthermore, N-doped hierarchical porous carbon with uniaxially packed carbon nanotubes (CNTs) was prepared. Core-shell structure and aligned CNTs enabled the ideal morphology of the CNT-CNF composite anode material, which provided not only a fast electrochemical species transportable space but also enhanced the Li-ion storage behavior on the lithiophilic surface. Effects of the hierarchical space characteristics of the CNFs on both the transport characteristics of the electrochemical species and the subsequent electrochemical performance

were investigated. Finally, Part IV provides perspectives on fast charging anode materials and future energy storage devices as concluding remarks

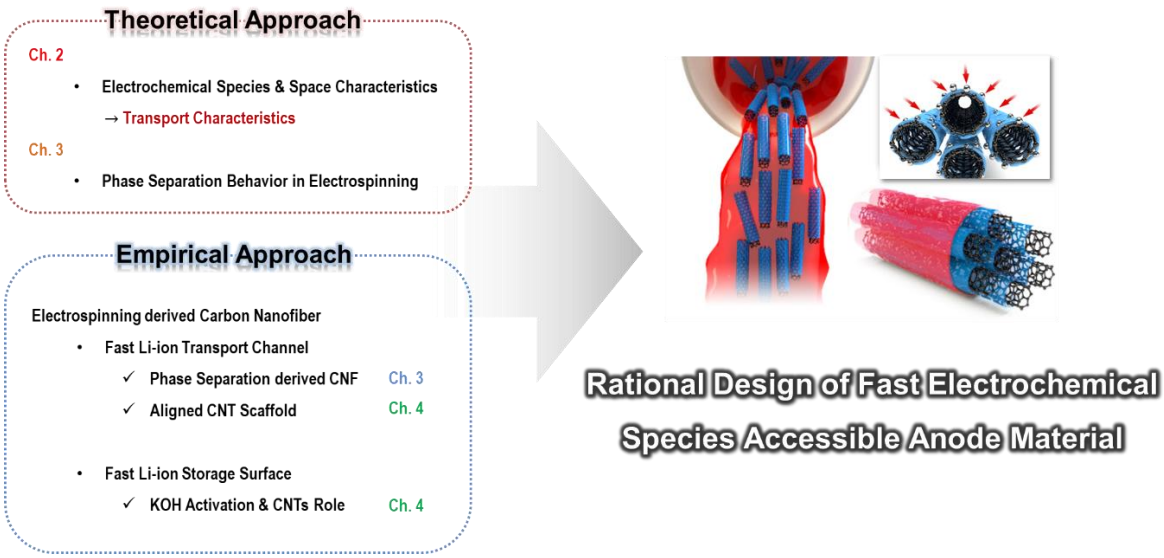

Figure 1.11 Aim and scope of this research

1.5 References

[1] A. Awasthi, V. Karthikeyan, V. Das, S. Rajasekar, A. Singh, Energy Storage Systems in Solar-Wind Hybrid Renewable Systems, 2017, pp. 189-222.

[2] M. Armand, J.M. Tarascon, Building better batteries, Nature 451(7179) (2008) 652-657.

[3] J.P. Pender, G. Jha, D.H. Youn, J.M. Ziegler, I. Andoni, E.J. Choi, A. Heller, B.S. Dunn, P.S. Weiss, R.M. Penner, C.B. Mullins, Electrode Degradation in Lithium-Ion Batteries, ACS Nano 14(2) (2020) 1243-1295.

[4] L. Xie, C. Tang, Z. Bi, M. Song, Y. Fan, C. Yan, X. Li, F. Su, Q. Zhang, C. Chen, Hard Carbon Anodes for Next-Generation Li-Ion Batteries: Review and Perspective, Advanced Energy Materials 11(38) (2021) 2101650.

[5] B.-R. Koo, K.-W. Sung, H.-J. Ahn, Boosting Ultrafast Lithium Storage Capability of Hierarchical Core/Shell Constructed Carbon Nanofiber/3D Interconnected Hybrid Network with Nanocarbon and FTO Nanoparticle Heterostructures, Advanced Functional Materials 30(32) (2020) 2001863.

[6] K.-H. Chen, V. Goel, M.J. Namkoong, M. Wied, S. Müller, V. Wood, J. Sakamoto, K. Thornton, N.P. Dasgupta, Enabling 6C Fast Charging of Li-Ion Batteries with Graphite/Hard Carbon Hybrid Anodes, Advanced Energy Materials 11(5) (2021) 2003336.

[7] L.-L. Jiang, C. Yan, Y.-X. Yao, W. Cai, J.-Q. Huang, Q. Zhang, Inhibiting Solvent Co-Intercalation in a Graphite Anode by a Localized High-Concentration Electrolyte in Fast-Charging Batteries, Angewandte Chemie International Edition 60(7) (2021) 3402-3406.

[8] L. Li, D. Zhang, J. Deng, Y. Gou, J. Fang, H. Cui, Y. Zhao, M. Cao, Carbon-based materials for fast charging lithium-ion batteries, Carbon 183 (2021) 721-734.

[9] A.M. Colclasure, A.R. Dunlop, S.E. Trask, B.J. Polzin, A.N. Jansen, K. Smith, Requirements for Enabling Extreme Fast Charging of High Energy Density Li-Ion Cells while

Avoiding Lithium Plating, Journal of The Electrochemical Society 166(8) (2019) A1412-A1424.

[10] K.-H. Chen, M.J. Namkoong, V. Goel, C. Yang, S. Kazemiabnavi, S.M. Mortuza, E. Kazyak, J. Mazumder, K. Thornton, J. Sakamoto, N.P. Dasgupta, Efficient fast-charging of lithium-ion batteries enabled by laser-patterned three-dimensional graphite anode architectures, J Power Sources 471 (2020) 228475.

[11] S. Li, K. Wang, G. Zhang, S. Li, Y. Xu, X. Zhang, X. Zhang, S. Zheng, X. Sun, Y. Ma, Fast Charging Anode Materials for Lithium-Ion Batteries: Current Status and Perspectives, Advanced Functional Materials 32(23) (2022) 2200796.

[12] C. Liu, N. Xiao, Y. Wang, Y. Zhou, G. Wang, H. Li, Y. Ji, J. Qiu, Electrospun nitrogen-doped carbon nanofibers with tuned microstructure and enhanced lithium storage properties, Carbon 139 (2018) 716-724.

[13] R. Fang, K. Chen, L. Yin, Z. Sun, F. Li, H.-M. Cheng, The Regulating Role of Carbon Nanotubes and Graphene in Lithium-Ion and Lithium–Sulfur Batteries, Advanced Materials 31(9) (2019) 1800863.

[14] L. Borchardt, D. Leistenschneider, J. Haase, M. Dvoyashkin, Diffusion: Revising the Concept of Pore Hierarchy for Ionic Transport in Carbon Materials for Supercapacitors (Adv. Energy Mater. 24/2018), Advanced Energy Materials 8(24) (2018) 1870108.

[15] X.-K. Wang, J. Shi, L.-W. Mi, Y.-P. Zhai, J.-Y. Zhang, X.-M. Feng, Z.-J. Wu, W.-H. Chen, Hierarchical porous hard carbon enables integral solid electrolyte interphase as robust anode for sodium-ion batteries, Rare Metals 39(9) (2020) 1053-1062.

[16] Y. Chen, X. Li, K. Park, J. Song, J. Hong, L. Zhou, Y.-W. Mai, H. Huang, J.B. Goodenough, Hollow Carbon-Nanotube/Carbon-Nanofiber Hybrid Anodes for Li-Ion Batteries, Journal of the American Chemical Society 135(44) (2013) 16280-16283.

[17] D. Nan, Z.-H. Huang, R. Lv, L. Yang, J.-G. Wang, W. Shen, Y. Lin, X. Yu, L. Ye, H. Sun, F. Kang, Nitrogen-enriched electrospun porous carbon nanofiber networks as high-performance free-standing electrode materials, Journal of Materials Chemistry A 2(46) (2014) 19678-19684.

[18] C. Kim, K.S. Yang, Electrochemical properties of carbon nanofiber web as an electrode for supercapacitor prepared by electrospinning, Applied Physics Letters 83(6) (2003) 1216-1218.

[19] G. Wang, C. Pan, L. Wang, Q. Dong, C. Yu, Z. Zhao, J. Qiu, Activated carbon nanofiber webs made by electrospinning for capacitive deionization, Electrochim Acta 69 (2012) 65-70.

[20] C. Chen, Y. Zhang, Y. Li, Y. Kuang, J. Song, W. Luo, Y. Wang, Y. Yao, G. Pastel, J. Xie, L. Hu, Highly Conductive, Lightweight, Low-Tortuosity Carbon Frameworks as Ultrathick 3D Current Collectors, Adv Energy Mater 7(17) (2017) 1700595.

[21] L. Xin, Y. Liu, B. Li, X. Zhou, H. Shen, W. Zhao, C. Liang, Constructing hierarchical submicrotubes from interconnected TiO2 nanocrystals for high reversible capacity and long-life lithium-ion batteries, Scientific Reports 4(1) (2014) 4479.

[22] L. Li, S. Peng, J.K.Y. Lee, D. Ji, M. Srinivasan, S. Ramakrishna, Electrospun hollow nanofibers for advanced secondary batteries, Nano Energy 39 (2017) 111-139.

[23] Q. Wang, Q. Cao, X. Wang, B. Jing, H. Kuang, L. Zhou, Dual template method to prepare hierarchical porous carbon nanofibers for high-power supercapacitors, Journal of Solid State Electrochemistry 17(10) (2013) 2731-2739.

[24] N. Li, C.R. Martin, A High-Rate, High-Capacity, Nanostructured Sn-Based Anode Prepared Using Sol-Gel Template Synthesis, J Electrochem Soc 148(2) (2001) A164.

[25] J. Kim, H.I. Cho, Y.S. Cho, S.H. Lee, C.R. Park, New insights into the effects of available space characteristics within graphite-based anodes on the accessibility of solvated Li-ions

under fast charging conditions, Carbon (2022).

Part II. Theoretical Study:

Electrochemical Species Transport in Active Material under Fast Charging Condition

Chapter 2 Correlation between Electrochemical Species and Space Characteristics of Anode Material

2.0 Major symbols

$\tilde{\mu}_{e-}^{c}$: Cathode potential

$\tilde{\mu}_{e-}^{a}$: Anode potential

F : Faraday constant

V : Voltage of battery cell

V_{OC} : open circuit potential

$\Delta\varphi^{c}$: Cathode overpotential

$\Delta\varphi^{a}$: Anode overpotential

$\Delta\varphi_{AM}^{a}$: Solid-state overpotential

$\Delta\varphi_{CT}^{a}$: Charge transfer overpotential

$\Delta\varphi_{EL}^{a}$: Electrolyte overpotential

$\mu_{Li^{+}}$: Half-cell potential

$\mu_{Li^{+}}^{0}$: Standard half-cell potential

R : Gas constant

T : Absolute temperature

$j_{applied}$: Applied current density

j_{lim} : Limit current density

A : Specific surface area

$\widetilde{D}_{Li^+}^{EL}$: Diffusion coefficient

$c_{Li^+,0}^{EL}$: Li^+ concentration

t_{Li^+} : Li^+ transference number

L_{EL} : Electrode thickness

I : interfacial current density

j_0 : exchange current density

E_a : activation energy

α : charge-transfer coefficient

$\mu_{Li^+}(x = L)$: Overpotential at surface

$\mu_{Li^+}(x = 0)$: Overpotential at center of active material

a_{Li^+} : Li^+ activity

c_{Li^+} : Total Li^+ concentration

$\Delta c_{Li^+} = c_{Li^+}(x = L) - c_{Li^+}(x = 0)$

$c_{Li^+}(x = L)$: Li^+ Concentration at surface

$c_{Li^+}(x = 0)$: Li^+ Concentration center of active material

$$W = \frac{\partial \ln(a_{Li^+})}{\partial \ln(c_{Li^+})}$$

2.1 Fundamental study of electrochemical kinetic limits under fast charging conditions

Fast-charging in a Li-ion battery system means more charge per time; accordingly, higher ionic and electronic transports are both required to make a fast redox reaction [1]. Because carbonaceous materials have an intrinsic high electrical conductivity, enhancing ion-transport has been considered as the main issue for a high rate performance [2-4]. In a normal charging process, Li^+ is extracted from the cathode and migrates to the anode solvated with the electrolyte and then approaches the active material and meets electrons for a redox reaction [5]. However, in a fast charging condition, if Li-ions cannot be transported to the active material fast enough to meet the fast-supplied electrons, the Li^+ concentration on the active material/electrolyte interface decreases approximately to zero [6, 7]. This phenomenon causes a concentration gradient along the active material (Fig. 2.1) and results in low utilization of the active material, low capacity retention, and subsequently a need for more voltage to obtain the theoretical capacity, which occurs as an overpotential in a fast-charging battery system (Fig. 2.2).

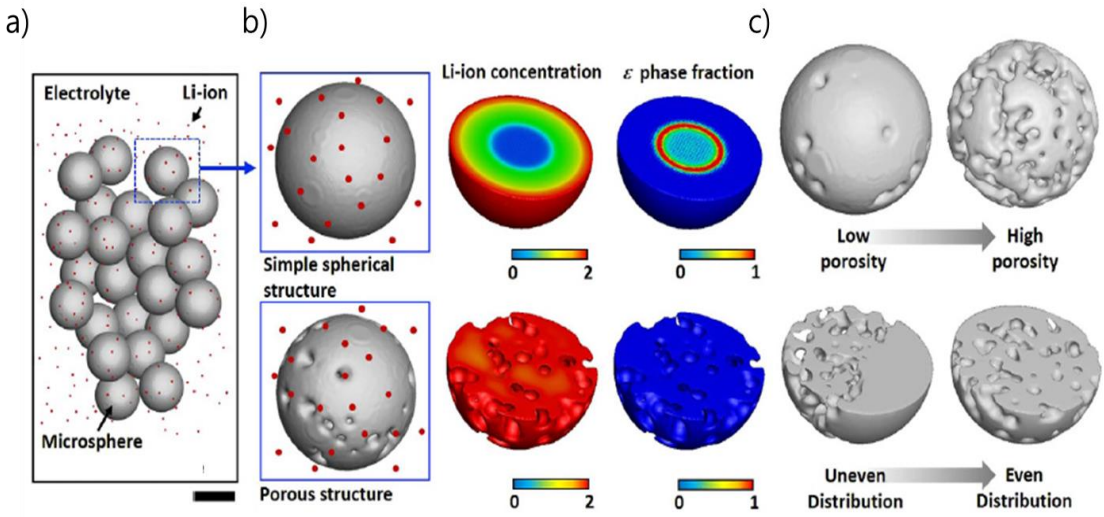

Figure 2.1 Design of the porous structure in the active material for ultrahigh performance. a) Illustration of the active material in a Li-ion battery consisting of a microsphere structure, Li-ion, and an electrolyte. Scale bar: 500 nm. b) Li-ion concentration and the ε phase fraction of a simple spherical structure and a porous structure in the active material. c) design of a porous active material with respect to porosity and the distribution of pores [8].

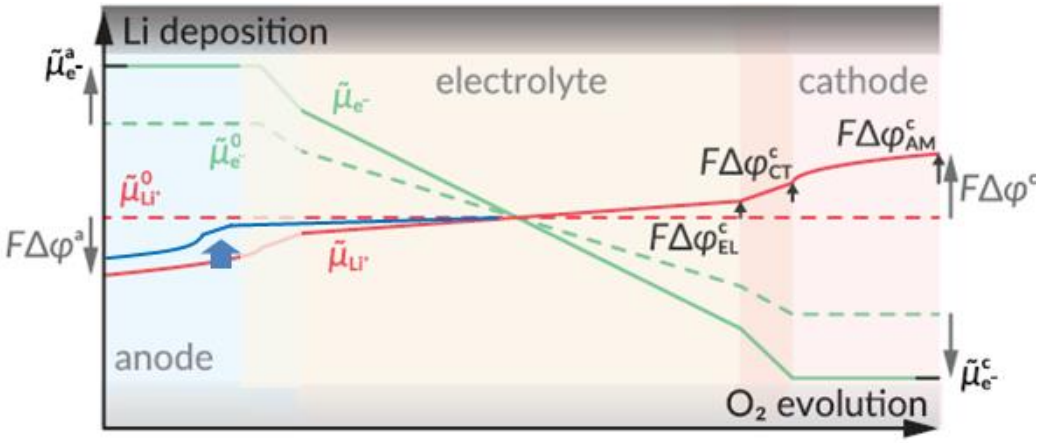

Figure 2.2 Schematic representation of the electrochemical potential profiles during charging (solid lines) and in equilibrium (dashed lines) [9].

Considering the difference between normal charge and fast charge conditions, kinetic models show the overpotential is affected mainly by the transport characteristics of the electrochemical species [10]. Especially, Li^+ ion transport mainly determines the overpotential since electrons are relatively faster and readily available.

$$V = -\frac{1}{F}(\tilde{\mu}_{e-}^{c} - \tilde{\mu}_{e-}^{a}) = V_{OC} + \Delta\varphi^{c} + \Delta\varphi^{a} \qquad (2.1)$$

$$\varphi^{a} = \Delta\varphi_{AM}^{a} + \Delta\varphi_{CT}^{a} + \Delta\varphi_{EL}^{a} \qquad (2.2)$$

The entire Li-ion transport mechanism within the anode material occurs in the following order: 1) solvated Li-ion transport to the active material/electrolyte interface, 2) solvated Li-ion desolvated at the interface with the charge transfer reaction and 3) diffusion through the solid-state in the active material [11, 12]. The concentration gradient caused by each step's transport limits in anode and subsequent overpotential is expressed in equation (2.2) and divided into transport steps as (2) overpotential needed to drive solvated Li-ion transport in an electrolyte-containing active material space ($\Delta\varphi_{EL}^{a}$), (3) overpotential to drive charge transfer between electrolyte/electrode ($\Delta\varphi_{CT}^{a}$) and (4) the overpotential to drive the solid-state diffusion in active material ($\Delta\varphi_{AM}^{a}$) by Weiss et al. [10].

$$\Delta\boldsymbol{\varphi_{EL}} = \boldsymbol{\mu_{Li^+}} - \boldsymbol{\mu^0_{Li^+}} = \frac{\boldsymbol{RT}}{\boldsymbol{F}}\mathbf{ln}\left(\mathbf{1} - \frac{\boldsymbol{I}}{\boldsymbol{j_{lim}A_{\emptyset}}}\right) \sim \boldsymbol{I}\frac{\boldsymbol{T}}{\boldsymbol{j_{lim}A_{\emptyset}}}\ ,\boldsymbol{j_{lim}} = \frac{\boldsymbol{F\tilde{D}^{EL}_{Li^+}c^{EL}_{Li^+,0}}}{\boldsymbol{(1-t_{Li^+})L_{EL}\beta}} \quad (2.3)$$

$$\Delta\boldsymbol{\varphi_{CT}} \sim \boldsymbol{I}\frac{\mathbf{1}}{\boldsymbol{Aj_0}}\ ,\ \boldsymbol{I} = \boldsymbol{j_0A}[\mathbf{exp}\left(\frac{\boldsymbol{\alpha F}}{\boldsymbol{RT}}\Delta\boldsymbol{\varphi_{CT}}\right) - \mathbf{exp}\left(-\frac{\boldsymbol{(1-\alpha)F}}{\boldsymbol{RT}}\Delta\boldsymbol{\varphi_{CT}}\right)]\ ,\ \boldsymbol{j_0} = \boldsymbol{j'_0}\,\mathbf{exp}\left(-\frac{\boldsymbol{E_a}}{\boldsymbol{RT}}\right) \quad (2.4)$$

$$\Delta\varphi^a_{AM} = -\frac{1}{F}[\mu_{Li^+}(x=L) - \mu_{Li^+}(x=0)] = \frac{RT}{F}\left(\frac{\partial\ln(a_{Li^+})}{\partial\ln(c_{Li^+})}\right)\Delta\ln(c_{Li^+}) = \frac{\mathrm{R}T}{F}W\frac{\Delta c_{Li^+}}{c_{Li^+}} \quad (2.5)$$

Considering eq. 2.5, overpotential in active material is proportional to the concentration gradient along the length of material (L). Therefore, in many previous battery studies, nano-sizing of active materials to shorten the diffusion length, overcoming sluggish solid-state diffusion and fully utilize the active material (eq.2.7, [13]) was a common approach to achieve a high specific capacity under fast charging conditions [14, 15].

$$\Delta\varphi^a_{AM} = -\frac{1}{F}[\mu_{Li^+}(x=L) - \mu_{Li^+}(x=0)] = \frac{RT}{F}\left(\frac{\partial\ln(a_{Li^+})}{\partial\ln(c_{Li^+})}\right)\Delta\ln(c_{Li^+}) = \frac{\mathrm{R}T}{F}W\frac{\Delta c_{Li^+}}{c_{Li^+}}$$

$$\Delta c_{Li^+} = c_{Li^+(x=L)} - c_{Li^+(x=0)} \quad (2.6)$$

Condition to fully utilize active material: $\mathrm{L} < \sqrt{t_{charge}D_{Li}}$ (2.7)

However, in the case of the anode material, nano-sizing is also accompanied by a large specific surface area (SSA) which leads to severe side reactions such as a large amount of SEI layer formation (Fig. 2.3) [16-18]. The SEI layer is an electrochemically inactive component (decrease A in eq. 2.8 and 2.9), which has a low electrical conductivity, and induces an additional overpotential due to a deteriorated charge transfer reaction [19].

$$R_{CT} = \frac{RT}{zFAj_0} \tag{2.8}$$

$$\Delta\varphi_{CT} \sim I\frac{1}{Aj_0} \tag{2.9}$$

For these reasons, simple nano-sizing has drawbacks to increase the overpotential in the other term, especially in an anode system under fast charging conditions.

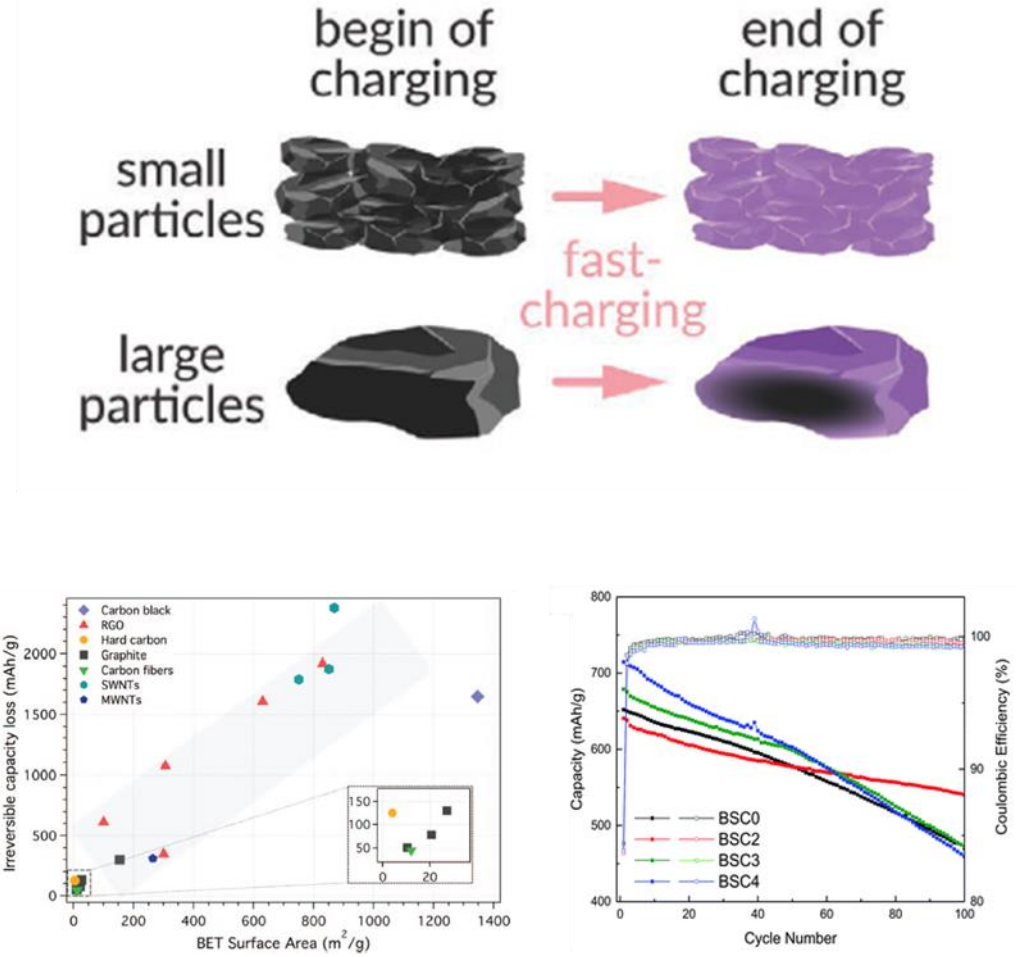

Figure 2.3 Nano-sizing of active material to fully utilize and subsequent side effects [18, 20]

Therefore, controlling transport characteristics of solvated Li-ion, rather than slow solid state diffusion, could be a good strategy to reduce the overpotential, especially for an anode material under fast charging conditions (eq. 2.3). At the surface of the active material or in electrolyte-containing space such as pore, solvated Li-ions in the electrolyte approach, and ions continuously react with the supplied electrons and consumed by the active materials. As mentioned above, the Li-ion concentration might decrease if solvated Li-ions are not transported and replenished from the bulk electrolyte to the surface as fast as the electrons that are provided under the fast charging condition [10]. This kinetic unbalance between the redox reaction rate and transport of solvated Li-ions to the active material causes a concentration polarization and subsequent overpotential [7, 11]. When this concentration polarization occurs on the active material/electrolyte interface where electrons and ions meet [21], the current density is unevenly distributed [6, 22, 23] and affects to interfacial current (I) which subsequently affect to exchange current density (j_0) [10, 11].

$$I = j_0 A \left[\exp\left(\frac{\alpha F}{RT}\Delta\varphi_{CT}\right) - \exp\left(-\frac{(1-\alpha)F}{RT}\Delta\varphi_{CT}\right)\right] \quad (2.10)$$

$$j_0 = j_0' \exp\left(-\frac{E_a}{RT}\right) \quad (2.11)$$

$$\Delta\varphi_{CT} \sim I\frac{1}{Aj_0} \quad (2.12)$$

Here, j_0' is a prefactor that is dependent on the concentrations of Li ions, vacancies, and electrons in the active material and the electrolyte. Consequently, slow transport of solvated Li-ion could induce concentration polarization and subsequent overpotential, which has a significant impact on the anode system under fast charging conditions, so the factors that affect the transport of Li-ion with electrolyte should be more clarified. In Fick's law with modification by a term that accounts for the consumption of Li-ion flux is as follows.

$$\frac{\partial c_{Li^+}^{EL}}{\partial t} = D_{Li^+}^{EL}\frac{\partial c_{Li^+}^{EL}}{\partial x^2} + \frac{I}{FAd}(1 - t_{Li^+}) \quad (2.13)$$

When concentration of fully depleted due to slow transport of solvated Li-ion, limiting current (j_{lim}) is occurred (eq. 2.14).

$$j_{lim} = \frac{FD_{Li^+}^{EL}c_{Li^+,0}^{EL}}{(1-t_{Li^+})L_{EL}\beta} \quad (2.14)$$

As seen in eq. 2.15, the limiting current (j_{lim}) and diffusion-limited current density (DLC) are the current and current density at which an overpotential begins to occur and this diffusion-limited current density should be high for reducing overpotential and maintaining electrochemical performance under fast charging condition [7] (Fig. 2.4).

$$\textit{Diffusion-limited Current density (DLC)} = \frac{j_{lim}}{Q_{areal}} = \frac{F\tilde{D}_{Li^+}^{EL} c_{Li^+,0}^{EL}}{(1-t_{Li^+})L_{EL}\beta Q_{areal}} \qquad (2.15)$$

$$\Delta\boldsymbol{\varphi_{EL}} = \boldsymbol{\mu_{Li^+}} - \boldsymbol{\mu_{Li^+}^0} = \frac{\boldsymbol{RT}}{\boldsymbol{F}}\mathbf{ln}\left(\mathbf{1} - \frac{\boldsymbol{I}}{\boldsymbol{j_{lim}A_{\emptyset}}}\right) \sim \boldsymbol{I}\frac{\boldsymbol{T}}{\boldsymbol{j_{lim}A_{\emptyset}}} \;, \quad \boldsymbol{j_{applied}} < \boldsymbol{j_{lim}} = \frac{\boldsymbol{F\tilde{D}_{Li^+}^{EL} c_{Li^+,0}^{EL}}}{(\mathbf{1}-\boldsymbol{t_{Li^+}})\boldsymbol{L_{EL}\beta}}$$

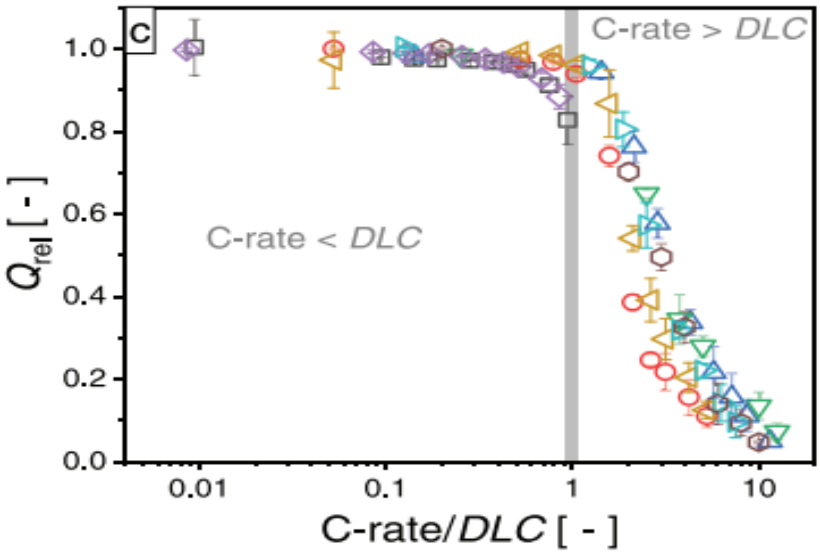

Figure 2.4 When the current density is higher than DLC, capacity drops dramatically [7].

Limiting current (j_{lim}) is expressed as a diffusion coefficient in the electrolyte phase and β value. In the case of active material which have some space large enough to contain electrolyte and solvated Li-ion inside, a diffusion coefficient in electrolyte should be modified to an effective diffusion coefficient of solvated Li-ion and it is related to the morphological characteristics of electrolyte containing space, considering the bruggman equation.

$$D_{eff} = \frac{\varepsilon D}{\tau} \tag{2.16}$$

$$\tau = \varepsilon^{-brugg} \tag{2.17}$$

Consequently, it indicates that overpotential occurred by concentration polarization of solvated Li-ion at electrolyte contacting interface can be controlled by the morphological characteristics of the space in active material which the solvated Li-ion transport through [14, 15]. In the case of PCNFs, this is closely related to both the morphology of the CNFs and various types of ion-transportable spaces in the CNFs such as pores, voids, and ion channels (Fig. 2.5). Therefore, modifying suitable space characteristics that consider the dynamic size of the ions, the morphology, and the solvated-ion path is the key to improving solvated Li-ion transport and reducing the overpotential by mitigating the concentration gradient in fast charging conditions [24, 25].

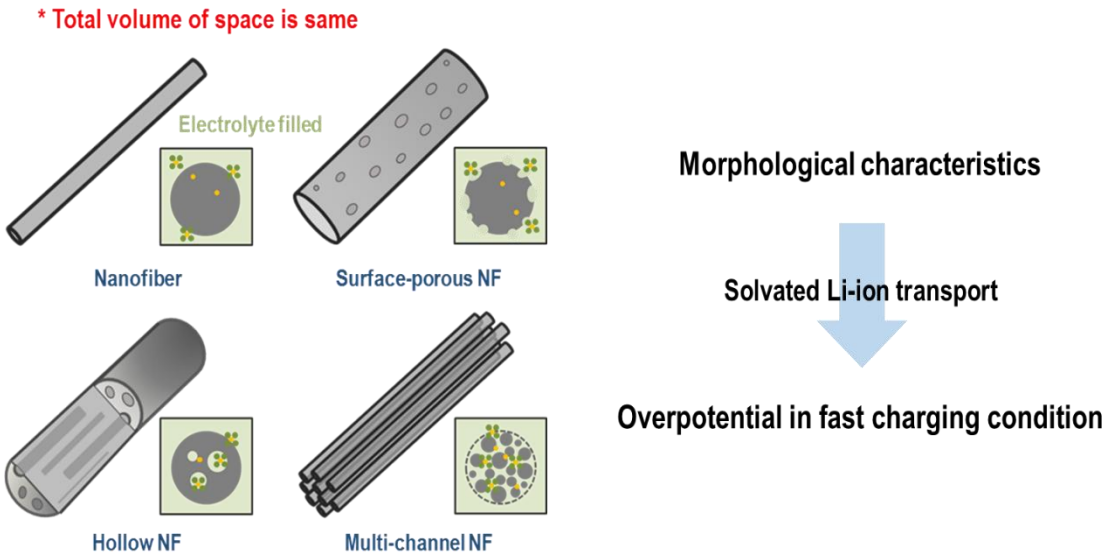

Figure 2.5 In the case of PCNFs, Li-ion transport is closely related to both the morphology of the CNFs and various types of ion-transportable spaces in the CNFs such as pores, voids, and ion channels

2.2 Interaction between electrochemical species and space characteristics of anode material

In terms of Li-ions, the entire process of lithium storage in an active material can be largely divided into mass transfer and charge transfer, in which solvated Li-ions move toward the active material and are reduced to Li after desolvation through the solid electrolyte interphase (SEI) layer. Notably, in the case of carbon nanofibers (CNFs), due to the intrinsic high electrical conductivity, it is reasonable to assume that the charge transfer variable is relatively minor. Accordingly, the mass transfer, in which lithium ions transport to the redox sites through various 'spaces' in the active material, is a more important issue for a fast (dis)charging rate. In fast charging conditions, there is a concentration polarization when solvated Li-ions are not transported fast enough because they are continuously consumed by the active materials. The Li-ion concentration near the surface decreases because Li-ions are mostly at the cathode part whereas only electrons are waiting for the Li-ions to come to the anode part [26]. Particularly, when these polarized circumstances are not flat but consist of a space surrounded by a surface of active material such as pores or voids, it is plausible to say that the solvated Li-ions move to the surface of the porous active material slowly as the space becomes smaller by the Bosanquet equation [26, 27]. Therefore, ion transport through a space within an active material is crucial considering side reactions such as Li metal plating and capacity decay which are mainly caused by slowly moving Li-ions accumulating on the surface of the active material [28, 29]. There are various sorts of 'space' that Li ions could move through in the anode material from micro-pores whose sizes are about 1~2 nm to voids whose sizes are up to a micrometer. (Fig. 2.6).

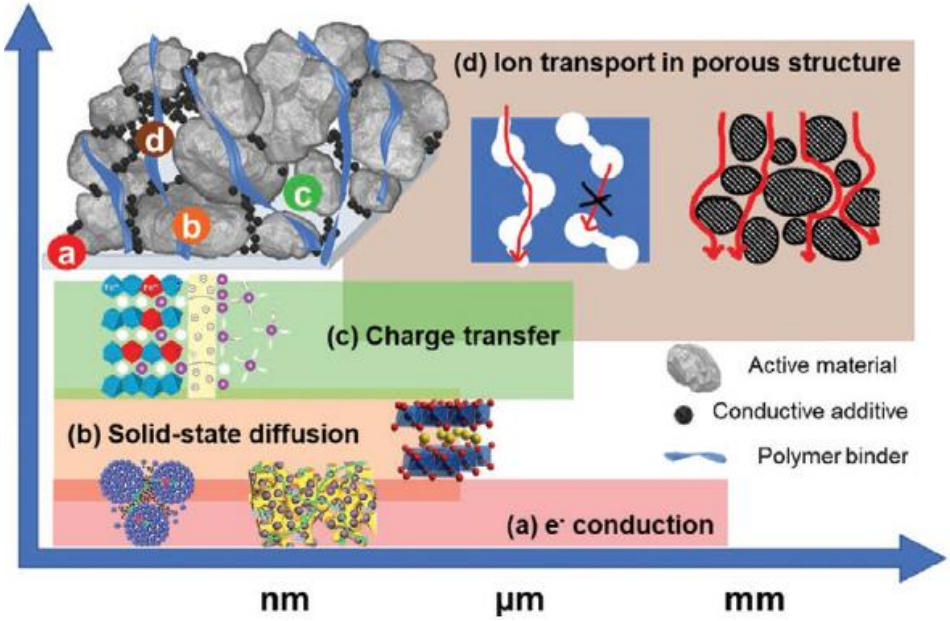

Figure 2.6 Various sorts of 'space' that Li ions could move through in the anode material from micro-pores whose sizes are about 1~2 nm to voids whose sizes are up to a micrometer

Chmiola *et al.* reported that when the space size is larger than the solvated ions, the ion transfer is faster, and if the size of the space is not larger than twice the size of the solvated ions, they prefer to be adsorbed rather than passing through the pores. (Fig. 2.7). When the size of the space is large enough to accommodate a few ions with their solvation shells across the space, the transport is mainly governed by the space size and tortuosity regardless of the charge of the transporting species [30-32]. This phenomenon implies that the solvated Li-ion transportable space could be sorted according to its size. In this study, a space that could act as a pathway where solvated Li-ions move through CNFs is named as 'channels.' Channels imply a space in the CNFs where a couple of solvated Li-ions move with the electrolyte before meeting electrons, whose size is too large for the solvated Li-ions to adsorb.

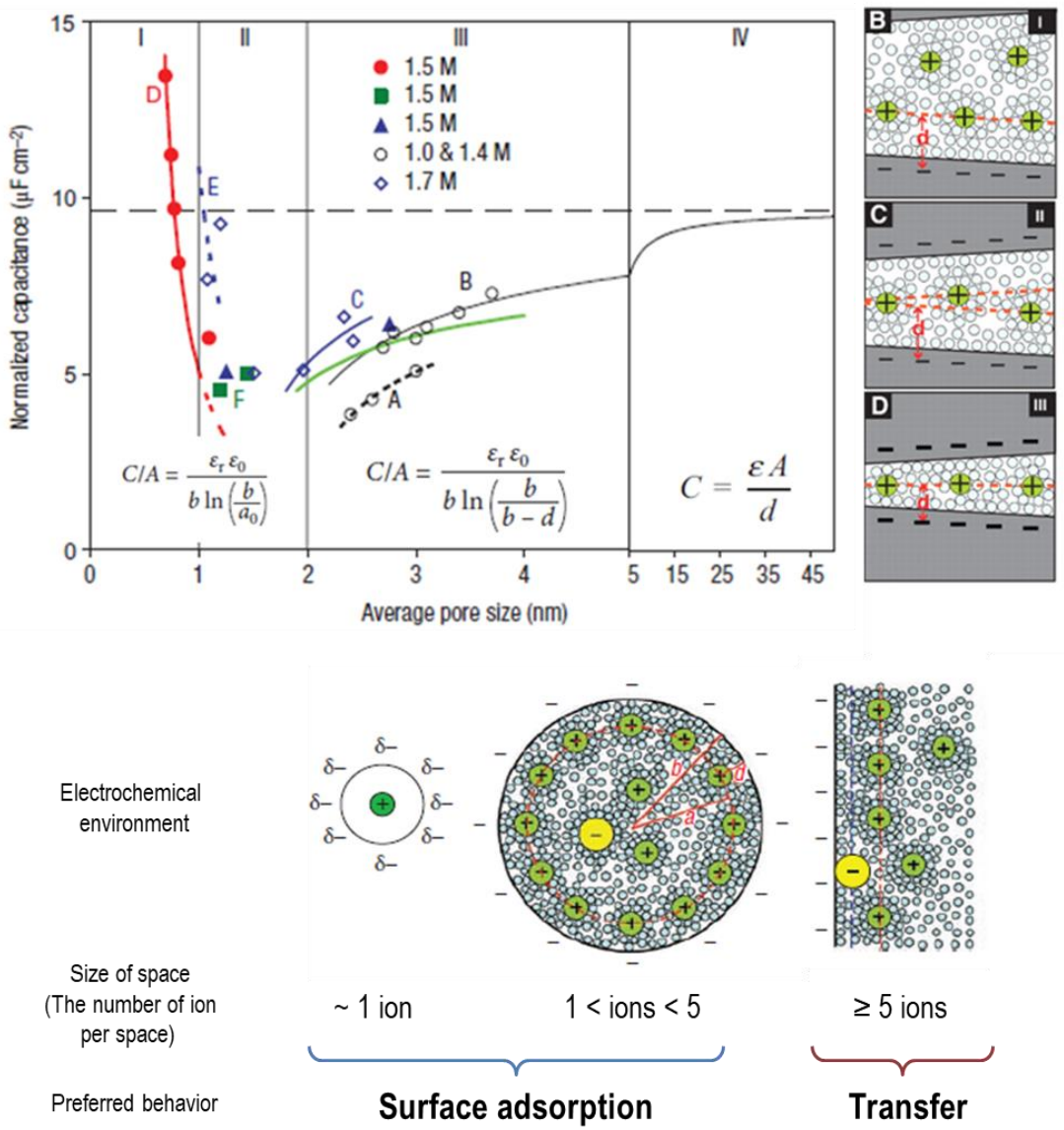

Figure 2.7 Space size effect on the transport and adsorption of Li ion

For the sake of enhancing the accessibility in each space, perceiving the characteristics of both the solvated Li-ions and space and the interactions between them are essential. In terms of static solvated Li-ions, there are 1st and 2nd solvation shell around Li^+ ion. Generally, there are three candidates to solvate Li^+ ion, which are 1) cyclic carbonate such as ethylene carbonate (EC), 2) linear carbonate such as diethyl carbonate (DEC) or dimethyl carbonate (DMC), and 3) anion such as $PF6^-$. 1st solvation shell participates in solvating a Li^+ ion and contributes to form lithium-solvents complexes and 2nd solvation shell serves as media for Li^+ ion-solvents complexes to transport in the electrolyte (Fig. 2.8)

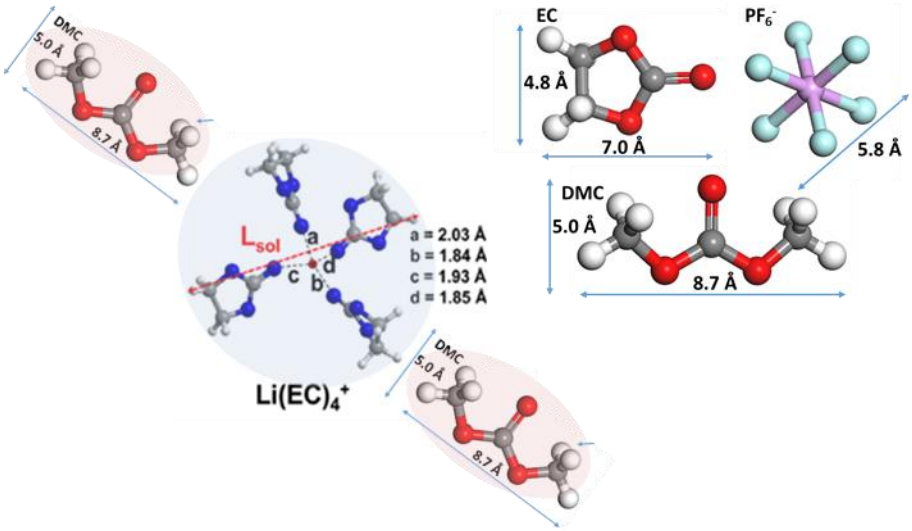

Figure 2.8 A schematic image of solvated Li-ion

Depending on which of the three candidates constitutes the solvation shell, the size of the solvated Li-ion is determined. Especially in fast charging condition, there is a change in solvent ion concentration due to transport of solvated Li-ion, enhancing viscosity of electrolyte (Fig. 2.9 a) and subsequently increasing dynamic size of solvated Li-ion according to stokes radius equation (Fig. 2.9 b). Furthermore, relatively larger electrolyte such as dimethyl carbonate (DMC: 8.7 Å) is preferably located at the first solvation shell position to a greater degree compared to the anion (PF_6^-: 5.8 Å) making the dynamic size of the solvated Li-ions even larger (Fig. 2.9 c d) [33-37]. Because surface adsorption is likely to happen when the space is not large enough to transfer with a bunch of electrolyte and Li-ions, it is plausible to assume the criterion for the channel could be several or up to tens of nanometers, unlike the previously used IUPAC classification.

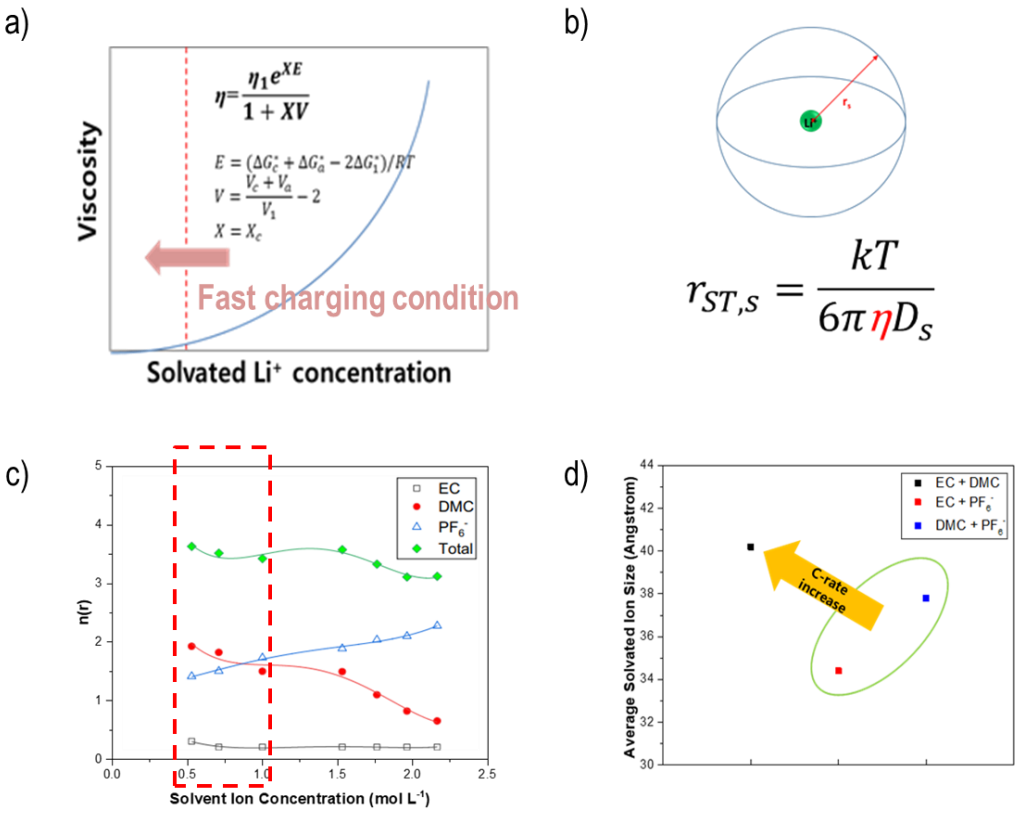

Figure 2.9 a) Correlation between solvated Li-ion concentration and viscosity b) Schematic diagram of stokes radius [36], c) relation between solvent ion concentration and coordination number of EC, DMC, and PF_6^- [38], and d) relation between solvent ion concentration and solvated ion size.

Furthermore, it should be assumed that not all channels are 'accessible' to let solvated Li-ions move through them. When there are various spaces in active material with different transport characteristics, it is expected that the more the active material has a fast ion transportable space, the faster the overall transport characteristics of the electrochemical species in the battery system.

$$D_{expected} = \rho_{slow} D_{slow} + \rho_{fast} D_{fast} \qquad (2.18)$$

$$(\rho_x = \frac{V_x}{V_{Total}})$$

However, this assumption is valid only as fast molecular exchange is guaranteed between slow and fast ion transportable space [32]. When there is another kinetic limits from slower-ion transportable space to faster one, ions can't transport as expected. To ensure actual fast ion transport in the appropriate space, how easy it is to access the space is important, which is conceptualized as the "accessibility" of space. The difference between 'accessible' space and 'inaccessible' space is whether the space is open or closed for an electrolyte to penetrate into, or the size of the space is large enough for solvated Li-ions to be in.

$$\text{Diffusion time}: \ \tau d = \frac{\lambda^2}{D_{eff}} \qquad (2.19)$$

$$D_{eff} = D_0 \, X \, \frac{\varepsilon}{\tau} \qquad (2.20)$$

$$\tau = -\frac{R_{ion} A k \varepsilon}{2d} \qquad (2.21)$$

Regarding to equations above, good accessibility, which can be represented as the parameter tortuosity (τ) quantitatively, affects actual transport behavior (D_{eff})of electrochemical species in the space. Collectively, the more directly ion can transport (low-tortuous), the lower solvated ion get resist in electrolyte-containing space (lower R_{ion} value) and subsequently diffusion time goes shorter. Therefore, the ion-transportable space should guarantee 1) fast electrolyte penetration, 2) low-tortuous pathways for solvated Li^+ ion, 3) high ionic diffusivity for high accessibility (Fig. 2.10).

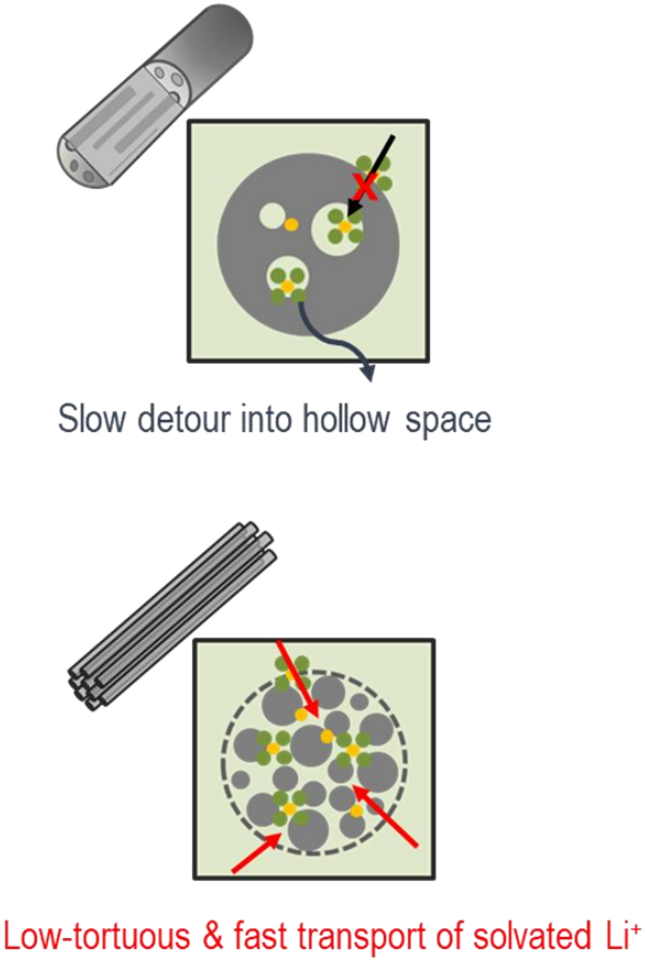

Figure 2.10 A schematic images of slow ion transportable space and fast ion transportable space

The accessibility of the space affects the utilization of the space and, in the case of an anode system, the subsequent charge transfer reaction too. When the space is not accessible and solvated Li-ions cannot be transported to the redox sites quickly, a concentration gradient occurs on the active material/electrolyte interface where electrons and ions meet. The concentration gradient induces an inhomogeneous consumption of Li-ions [21], and subsequently, the current density is unevenly distributed [6, 22, 23] and eventually affects the interfacial current [10, 11]. Furthermore, the unevenly distributed surface charge on the active material affects the formation of the SEI layer and results in an irregular, continuous SEI layer [23, 39] (Fig. 2.11). This thick SEI layer causes clogging of the electrolyte-contacting space and limits the further transport of lithium ions.

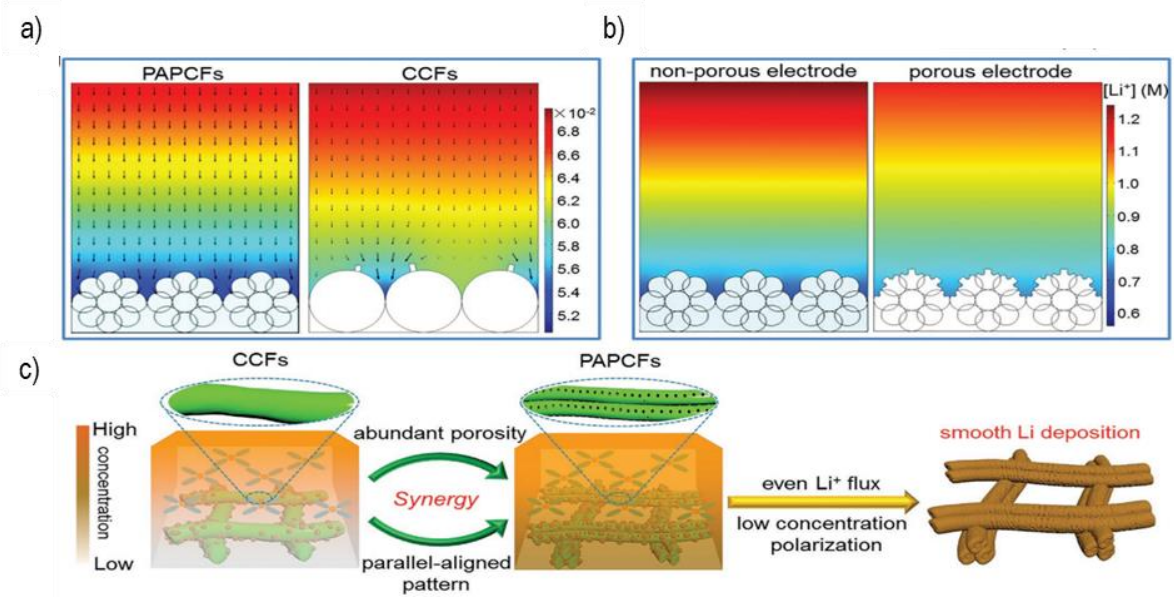

Figure 2.11 Adoption of space in active material results in enhanced Li-ion accessibility and even Li-ion concentration

The importance of channel accessibility in CNFs was suggested in my previous study using a basic graphite material [40]. To determine whether the created space is accessible, cross-analysis of BET with SAXS was conducted, in which gas-adsorption based BET analysis could present information on where N_2 gas molecules could access pores, while small-angle X-ray scattering (SAXS) analysis is sensitive to both accessible and inaccessible (closed) pores. Considering all samples in this study were made from the same material and the only difference in the SSA came from the same modifying process (as graphite powder made into a slurry with various nano-sized additives, a space was newly generated, and this space was identified to be the solvated Li-ion pathway), it was the creation of the space within the active material that caused the increase in the SSA. This phenomenon arises because some pores in the active material have an opening smaller than N_2 molecules preventing access (sealed) or even have no opening (closed), which are inaccessible. Therefore, the difference in tendency of the SSA between the two methods could be a result of the existence of inaccessible pores which are detectable only through the two phase model in SAXS. To find the correlation between the accessibility of pores and the solvated Li-ion transport, we approximated the expected degree of inaccessible pore (space not acting as an ion channel) generation, making the 'inaccessible pore increase' parameter described by the following equation.

Inaccessible pore increase (%)

$$= \frac{(\text{SAXS SSA of Sample} - \text{SAXS SSA of G powder})*100}{\text{SAXS SSA of G powder}} - \frac{(\text{BET SSA of Sample} - \text{BET SSA of G powder})*100}{\text{BET SSA of G powder}}$$

The difference between the degrees of SSA increase from the powder to electrode state for both analysis methods could suggest the creation of inaccessible pores. Consequently, it linearly matched with both the tortuosity and coulombic efficiency (%), indicating that inaccessible pores, which are hardly accessible to solvated Li-ions, reduced the efficiency level of the active material (Fig. 2.12).

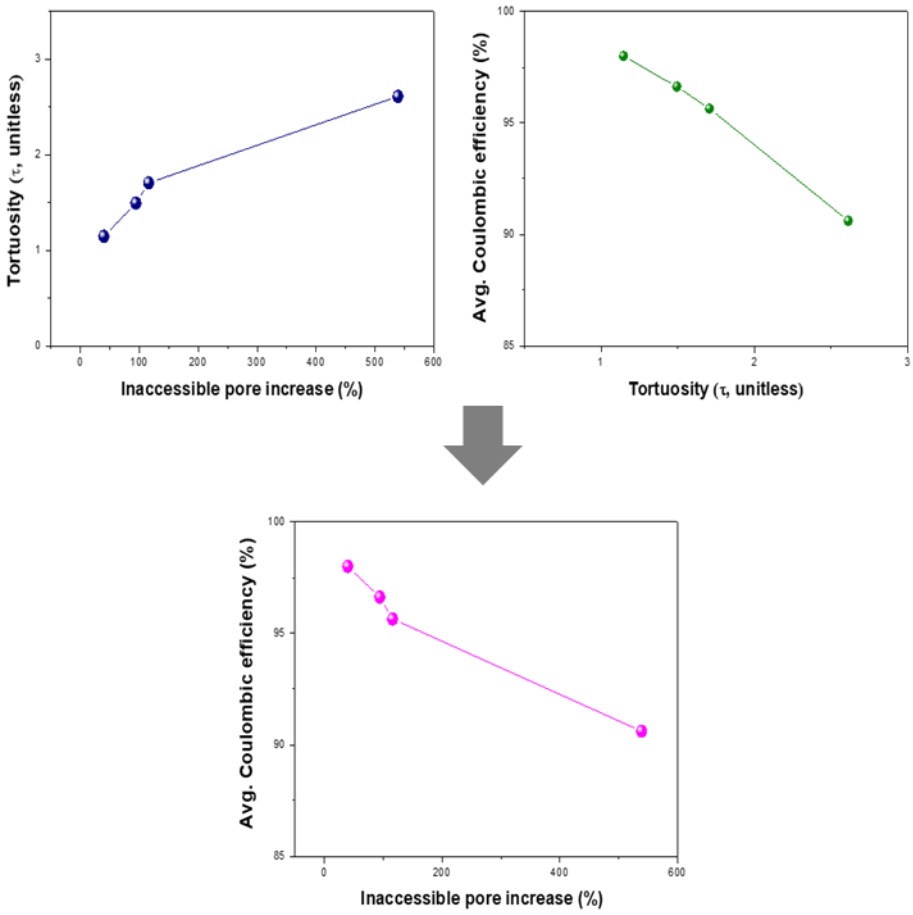

Figure 2.12 Importance of accessibility of space on transport characteristics of Li-ion and subsequent electrochemical performance

Regarding these results and the fundamental studies above, a rational design of a fast-charging CNF anode material should guarantee an accessible space where solvated Li-ions move as a channel, considering both the dynamic size of the solvated Li-ions and the accessibility of the space to enhance both transport of electrochemical species and subsequent charge transfer and Li-ion storage behavior (Fig. 2.13).

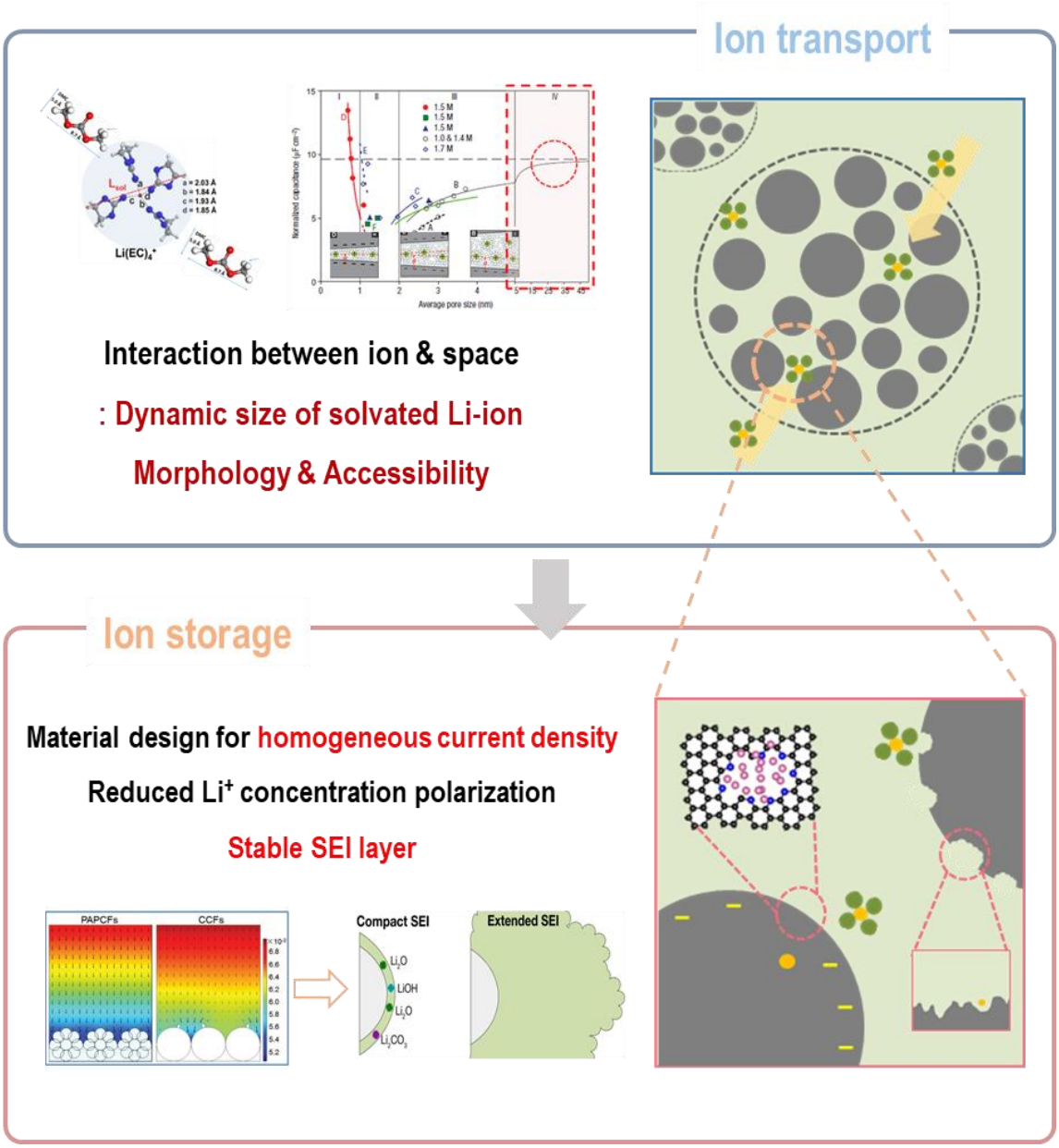

Figure 2.13 Effects of space characteristics of active material on both transport characteristics and storage behavior of electrochemical species

2.3 Summary

Fast-charging in a Li-ion battery system means more charge per time. In an anode system, enhancing the transport of Li-ions is considered the main issue to solve because a slow ion transport induces a concentration polarization and subsequent overpotential. Considering kinetic models, enhancing the transport characteristics of solvated Li-ions could efficiently solve kinetic limits under fast charging conditions. The transport characteristics of solvated Li-ions can be controlled by morphological characteristics such as the 'space' in the active material which the solvated Li-ions transport through. Therefore, a proper 'space' should be adopted in the active material in terms of enhancing the Li-ion accessibility and even the Li-ion concentration, considering the kinetic size of the solvated Li-ions and the accessibility of the space. The kinetic size of the solvated Li-ions varies dependent on the fast charging condition, which requires a new classification of space size rather than the previous IUPAC one. Furthermore, the morphological characteristics of the space, including the tortuosity, dimension and accessibility, affect the transport characteristics of the electrochemical species. Consequently, the rational design of the fast-charging anode material should guarantee 1) fast electrolyte penetration, 2) low-tortuous pathways for solvated Li^+ ions, and 3) high ionic diffusivity for high accessibility to reduce the overpotential by mitigating the concentration polarization in fast charging conditions

*** Part of result and discussion of Chapter 2 was published in**

Carbon 203 (2023) 152–160

2.4 References

[1] L. Li, D. Zhang, J. Deng, Y. Gou, J. Fang, H. Cui, Y. Zhao, M. Cao, Carbon-based materials for fast charging lithium-ion batteries, Carbon 183 (2021) 721-734.

[2] A.S. Ho, D.Y. Parkinson, D.P. Finegan, S.E. Trask, A.N. Jansen, W. Tong, N.P. Balsara, 3D Detection of Lithiation and Lithium Plating in Graphite Anodes during Fast Charging, ACS Nano 15(6) (2021) 10480-10487.

[3] F. Jiang, P. Peng, Elucidating the Performance Limitations of Lithium-ion Batteries due to Species and Charge Transport through Five Characteristic Parameters, Scientific Reports 6(1) (2016) 32639.

[4] D.P. Finegan, A. Quinn, D.S. Wragg, A.M. Colclasure, X. Lu, C. Tan, T.M.M. Heenan, R. Jervis, D.J.L. Brett, S. Das, T. Gao, D.A. Cogswell, M.Z. Bazant, M. Di Michiel, S. Checchia, P.R. Shearing, K. Smith, Spatial dynamics of lithiation and lithium plating during high-rate operation of graphite electrodes, Energy & Environmental Science 13(8) (2020) 2570-2584.

[5] G.-L. Zhu, C.-Z. Zhao, J.-Q. Huang, C. He, J. Zhang, S. Chen, L. Xu, H. Yuan, Q. Zhang, Fast Charging Lithium Batteries: Recent Progress and Future Prospects, Small 15(15) (2019) 1805389.

[6] X. Lu, A. Bertei, D.P. Finegan, C. Tan, S.R. Daemi, J.S. Weaving, K.B. O'Regan, T.M.M. Heenan, G. Hinds, E. Kendrick, D.J.L. Brett, P.R. Shearing, 3D microstructure design of lithium-ion battery electrodes assisted by X-ray nano-computed tomography and modelling, Nature Communications 11(1) (2020) 2079.

[7] C. Heubner, M. Schneider, A. Michaelis, Diffusion-Limited C-Rate: A Fundamental

Principle Quantifying the Intrinsic Limits of Li-Ion Batteries, Adv Energy Mater 10(2) (2020) 1902523.

[8] J. Song, J. Kim, T. Kang, D. Kim, Design of a Porous Cathode for Ultrahigh Performance of a Li-ion Battery: An Overlooked Pore Distribution, Scientific Reports 7(1) (2017) 42521.

[9] M. Weiss, R. Ruess, J. Kasnatscheew, Y. Levartovsky, N.R. Levy, P. Minnmann, L. Stolz, T. Waldmann, M. Wohlfahrt-Mehrens, D. Aurbach, M. Winter, Y. Ein-Eli, J. Janek, Fast Charging of Lithium-Ion Batteries: A Review of Materials Aspects, Adv Energy Mater 11(33) (2021).

[10] M. Weiss, R. Ruess, J. Kasnatscheew, Y. Levartovsky, N.R. Levy, P. Minnmann, L. Stolz, T. Waldmann, M. Wohlfahrt-Mehrens, D. Aurbach, M. Winter, Y. Ein-Eli, J. Janek, Fast Charging of Lithium-Ion Batteries: A Review of Materials Aspects, Advanced Energy Materials 11(33) (2021) 2101126.

[11] T. Gao, Y. Han, D. Fraggedakis, S. Das, T. Zhou, C.-N. Yeh, S. Xu, W.C. Chueh, J. Li, M.Z. Bazant, Interplay of Lithium Intercalation and Plating on a Single Graphite Particle, Joule 5(2) (2021) 393-414.

[12] L. Borchardt, D. Leistenschneider, J. Haase, M. Dvoyashkin, Diffusion: Revising the Concept of Pore Hierarchy for Ionic Transport in Carbon Materials for Supercapacitors (Adv. Energy Mater. 24/2018), Advanced Energy Materials 8(24) (2018) 1870108.

[13] T. Abe, H. Fukuda, Y. Iriyama, Z. Ogumi, Solvated Li-Ion Transfer at Interface Between Graphite and Electrolyte, Journal of The Electrochemical Society 151(8) (2004) A1120.

[14] Q. Cheng, Y. Zhang, Multi-Channel Graphite for High-Rate Lithium Ion Battery, Journal of The Electrochemical Society 165(5) (2018) A1104-A1109.

[15] Q. Cheng, R. Yuge, K. Nakahara, N. Tamura, S. Miyamoto, KOH etched graphite for fast chargeable lithium-ion batteries, Journal of Power Sources 284 (2015) 258-263.

[16] F. Joho, B. Rykart, A. Blome, P. Novák, H. Wilhelm, M.E. Spahr, Relation between surface properties, pore structure and first-cycle charge loss of graphite as negative electrode in lithium-ion batteries, Journal of Power Sources 97-98 (2001) 78-82.

[17] T. Placke, V. Siozios, R. Schmitz, S.F. Lux, P. Bieker, C. Colle, H.W. Meyer, S. Passerini, M. Winter, Influence of graphite surface modifications on the ratio of basal plane to "non-basal plane" surface area and on the anode performance in lithium ion batteries, Journal of Power Sources 200 (2012) 83-91.

[18] K. Omichi, G. Ramos-Sanchez, R. Rao, N. Pierce, G. Chen, P.B. Balbuena, A.R. Harutyunyan, Origin of Excess Irreversible Capacity in Lithium-Ion Batteries Based on Carbon Nanostructures, J Electrochem Soc 162(10) (2015) A2106.

[19] S.J. An, J. Li, C. Daniel, D. Mohanty, S. Nagpure, D.L. Wood, The state of understanding of the lithium-ion-battery graphite solid electrolyte interphase (SEI) and its relationship to formation cycling, Carbon 105 (2016) 52-76.

[20] S. Wu, B. Yu, Z. Wu, S. Fang, B. Shi, J. Yang, Effect of particle size distribution on the electrochemical performance of micro-sized silicon-based negative materials, Rsc Advances 8(16) (2018) 8544-8551.

[21] C.-Y. Fan, D. Xie, X.-H. Zhang, W.-Y. Diao, R. Jiang, X.-L. Wu, Homogeneous Li+ Flux Distribution Enables Highly Stable and Temperature-Tolerant Lithium Anode, Advanced Functional Materials 31(32) (2021) 2102158.

[22] H. Chen, A. Pei, J. Wan, D. Lin, R. Vilá, H. Wang, D. Mackanic, H.-G. Steinrück, W.

Huang, Y. Li, A. Yang, J. Xie, Y. Wu, H. Wang, Y. Cui, Tortuosity Effects in Lithium-Metal Host Anodes, Joule 4(4) (2020) 938-952.

[23] J. Man, K. Liu, H. Zhang, Y. Du, J. Yin, X. Wang, J. Sun, Dendrite-free lithium metal anode enabled by ion/electron-conductive N-doped 3D carbon fiber interlayer, Journal of Power Sources 489 (2021) 229524.

[24] W. Cai, C. Yan, Y.-X. Yao, L. Xu, R. Xu, L.-L. Jiang, J.-Q. Huang, Q. Zhang, Rapid Lithium Diffusion in Order@Disorder Pathways for Fast-Charging Graphite Anodes, Small Structures 1(1) (2020) 2000010.

[25] S. Uchida, T. Kiyobayashi, What differentiates the transport properties of lithium electrolyte in ethylene carbonate mixed with diethylcarbonate from those mixed with dimethylcarbonate?, Journal of Power Sources 511 (2021) 230423.

[26] N. Gao, S. Kim, P. Chinnam, E.J. Dufek, A.M. Colclasure, A. Jansen, S.B. Son, I. Bloom, A. Dunlop, S. Trask, K.L. Gering, Methodologies for Design, Characterization and Testing of Electrolytes that Enable Extreme Fast Charging of Lithium-ion Cells, Energy Storage Mater 44 (2022) 296-312.

[27] C.J. Ridgway, P.A.C. Gane, J. Schoelkopf, Effect of capillary element aspect ratio on the dynamic imbibition within porous networks, J Colloid Interf Sci 252(2) (2002) 373-382.

[28] K.H. Xue, G.L. Plett, A convective transport theory for high rate discharge in lithium ion cells, Electrochim Acta 87 (2013) 575-590.

[29] A. Mistry, F.L.E. Usseglio-Viretta, A. Colclasure, K. Smith, P.P. Mukherjee, Fingerprinting Redox Heterogeneity in Electrodes during Extreme Fast Charging, J Electrochem Soc 167(9) (2020).

[30] P. Simon, Y. Gogotsi, Materials for electrochemical capacitors, Nat Mater 7(11) (2008) 845-854.

[31] J. Chmiola, G. Yushin, Y. Gogotsi, C. Portet, P. Simon, P.L. Taberna, Anomalous increase in carbon capacitance at pore sizes less than 1 nanometer, Science 313(5794) (2006) 1760-1763.

[32] L. Borchardt, D. Leistenschneider, J. Haase, M. Dvoyashkin, Revising the Concept of Pore Hierarchy for Ionic Transport in Carbon Materials for Supercapacitors, Advanced Energy Materials 8(24) (2018).

[33] A. Mallarapu, V.S. Bharadwaj, S. Santhanagopalan, Understanding extreme fast charge limitations in carbonate mixtures, Journal of Materials Chemistry A 9(8) (2021) 4858-4869.

[34] M.J. Boyer, L. Vilčiauskas, G.S. Hwang, Structure and Li+ ion transport in a mixed carbonate/LiPF6 electrolyte near graphite electrode surfaces: a molecular dynamics study, Physical Chemistry Chemical Physics 18(40) (2016) 27868-27876.

[35] M. Okoshi, Y. Yamada, S. Komaba, A. Yamada, H. Nakai, Theoretical Analysis of Interactions between Potassium Ions and Organic Electrolyte Solvents: A Comparison with Lithium, Sodium, and Magnesium Ions, J Electrochem Soc 164(2) (2017) A54-A60.

[36] Christopher, D. Lemordant, P. Porion, L. Timperman, G. Schmidt, M. Anouti, Ionic association analysis of LiTDI, LiFSI and LiPF₆ in EC/DMC for better Li-ion battery performances, Rsc Advances 9(8) (2019) 4599-4608.

[37] H.G. Steinruck, C.T. Cao, Y. Tsao, C.J. Takacs, O. Konovalov, J. Vatamanu, O. Borodin, M.F. Toney, The nanoscale structure of the electrolyte-metal oxide interface, Energ Environ Sci 11(3) (2018) 594-602.

[38] H. Haghkhah, B.G. Choobar, S. Amjad-Iranagh, Effect of salt concentration on properties of mixed carbonate-based electrolyte for Li-ion batteries: a molecular dynamics simulation study, J Mol Model 26(8) (2020).

[39] Z. Lv, M. Yue, M. Ling, H. Zhang, J. Yan, Q. Zheng, X. Li, Controllable Design Coupled with Finite Element Analysis of Low-Tortuosity Electrode Architecture for Advanced Sodium-Ion Batteries with Ultra-High Mass Loading, Advanced Energy Materials 11(17) (2021) 2003725.

[40] J. Kim, H.I. Cho, Y.S. Cho, S.H. Lee, C.R. Park, New insights into the effects of available space characteristics within graphite-based anodes on the accessibility of solvated Li-ions under fast charging conditions, Carbon (2022).

Part III. Empirical Verification of Rationally Designed Fast Electrochemical Species Transportable Anode Material

Chapter 3. Correlation between the Space Characteristics of CNF and Li^+ ion Transport

3.1 Phase separation derived electrospinning for building fast electrochemical species transportable space in carbon nanofiber

3.1.1 General introduction of electrospinning

Electrospinning has been studied as the most effective and simplest technique to fabricate continuous nanofiber due to its capability and feasibility to generate nanofibers with well-defines topologies at low cost [1-3]. Fig. 3.1 shows a schematic image of the setup for electrospinning. Various type of space has been adopted on the nanofiber to modify performance of the nanofiber such as porous [4], hollow [5], core-shell [6] from diverse methods. Among such methods, polymer blend electrospinning has an advantage of capability to control the morphology of space. As one polymer is removed by post-fabrication after electrospinning and subsequently making corresponding empty space at the place where the polymer was, the characteristics of the space in nanofiber can be designed and controlled by phase separation behavior of the two immiscible polymers in the nanofiber [7-9]. (Fig. 3.2).

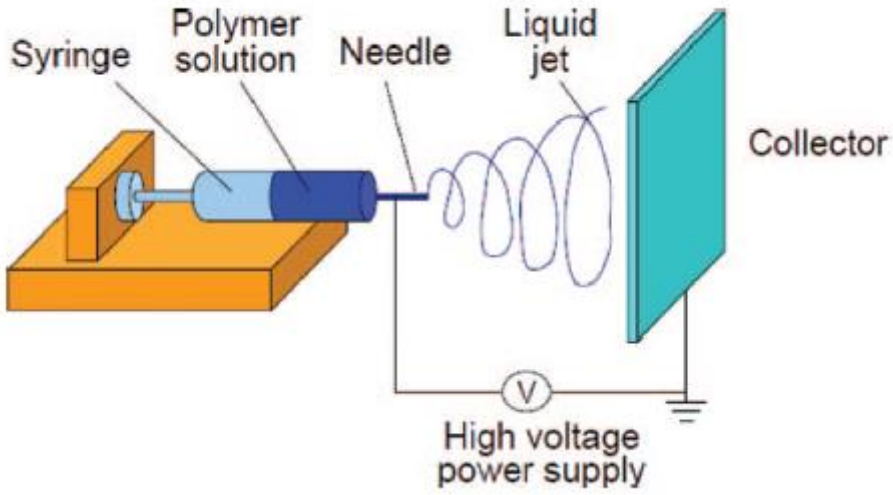

Figure 3.12 Schematic of an electrospinning setup. The electrically-charged jet undergoes an elongation and-whipping process, which is accompanied by the rapid evaporation of the solvent to reduce the jet diameter [10]

Method	Pros	Cons	Material	SSA	Electrochemical Performance
Polymer blend	Easy & cost-effective Size and structure of pore are controllable	Confined on few polymer-solvent Fundamental study is still needed	PAN, PMMA/DMF	306	354 mAh g^{-1} after 100 cycles at 200 mA g^{-1}
			PAN, SAN/DMF	13	391 mAh g^{-1} after 10 cycles at 200 mA g^{-1}
			PAN, PLLA/DMF	235	435 mAh g^{-1} after 50 cycles at 50 mA g^{-1}
Hard template	Hierarchical porous structure	Expensive & environmentally unfriendly Structural instability	PAN/SiO_2/DMF	91.8	454 mAh g^{-1} after 10 cycles at 50 mA g^{-1}
			PAA/SiO_2/DMAc	950	445 mAh g^{-1} after 50 cycles at 50 mA g^{-1}
			PAN/Zn/DMF	438	385 mAh g^{-1} after 10 cycles at 100 mA g^{-1}
Activation	Abundant micropore to enhance SSA Stimulate the surface oxygen functional groups	Confined on micropore, surface Structural instability	PAN + H_2O	1056	513 mAh g^{-1} after 50 cycles at 50 mA g^{-1}
			PAN + Air	583	1550 mAh g^{-1}
			PAN–$Fe(acac)_3$ + Air	542.6	717.2 mAh g^{-1}
Dual nozzle	Complex morphology with nozzle configuration	Complicated experimental parameters	TiO_2/PVP HNF	-	-
			$Ti(OC_4H_9)_4$/PVP	108.4	-

Figure 3.13 Various methods to fabricate porous carbon nanofiber

3.1.2 Phase separation behavior in immiscible polymer blend electrospinning

In order to control and design phase-separated electrospun nanofibers, understanding the phase separation process that arises from the electrospinning process is crucial. Phase separation of the immiscible polymers is a complicated phenomenon which depends on thermodynamic parameters (temperature and pressure), molecular parameters (miscibility of two polymers, solvent and concentration) and processing parameters (electrospinning setup parameters such as flow rate and collector distance) [11]. From a thermodynamic view, phase separation depends on the Gibbs free energy, and the thermodynamic phase diagram provides a useful guide for predicting the behavior of the immiscible polymer blend during electrospinning.

$$\Delta G_m = \Delta H_m - T\Delta S_m$$

$$\Delta G_m = \frac{RT}{V_r}\left[\frac{\varphi_A \ln \varphi_A}{V_A/V_r} + \frac{\varphi_B \ln \varphi_B}{V_B/V_r} + \chi_{AB}\varphi_A\varphi_B\right]$$

(Here, V_A and V_B are the molar volume and φ_A and φ_B are the molar fractions of

A and B, respectively. V_r is the molar volume of the unit cell or the repetitive unit of the polymer, commonly referred as the reference volume)

Fig. 3.3 is a schematic image of the phase separation behavior of a binary polymer blend system when it is electrospun at a given temperature. Commonly, the ternary phase diagram of an immiscible polymer blend system is divided by a binodal line into one- and two-phase regions

[12]. Ideally, the phase diagram could be expected to be further divided by a spinodal curve into a metastable region and an unstable phase-separated region. It is crucial to predict the phase morphology of the blend depending on the location of the blend composition, whether it is in the stable phase region or unstable phase region, because the morphology of nanofibers is derived from the elongation of the corresponding phase morphology. During the electrospinning process, solvent is rapidly evaporated, and the state of the polymer blend is changed from a homogeneous one-phased system to two separated phases. Phase separation occurs immediately on entering the "metastable" region bound by binodal and spinodal curves and separates into two phases: one phase containing more of polymer 1 (defined as the Polymer 1-rich phase) and the other more of polymer 2 (defined as the Polymer 2-rich phase).

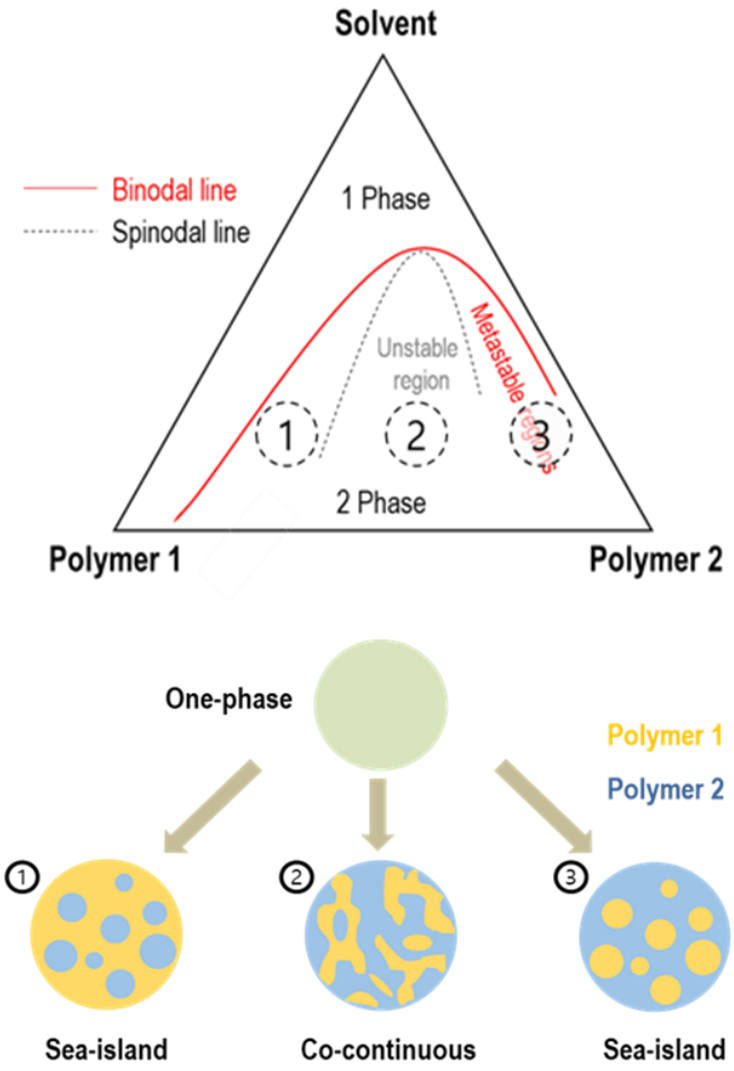

Figure 3.14 A schematic image of the phase separation behavior of a binary polymer blend system when it is electrospun at a given temperature

The phase separation behavior is divided into two major categories: (1) the co-continuous phases that are interpenetrated with each of the other phases when the system enters the unstable phase-separated region bound by the spinodal curve and spinodal decomposition occurs (region 2 in Fig. 3.3) and (2) nucleation & growth in which one polymer forms a continuous phase (sea structure) and the other polymer forms a concentrated dispersed phase (island structure), typically a "sea-island" morphology (region 1,3 in Fig. 3.3) [13]. Among the diverse variables that affect the phase diagram of a blend system, solubility or miscibility, which are determined by Flory-Huggins interaction parameter (χ), is one of the most important properties that enable us to interpret and predict the phase separation behavior and the morphology of nanofibers which are elongated from the separated phase [11].

$$\chi_{ij} = V A_{i,j} / RT \qquad A_{i,j}=[(\delta_{dj}-\delta_{di})^2 +0.25(\delta_{pj}-\delta_{pi})^2 +0.25(\delta_{hj}-\delta_{hi})^2]$$

A high χ value means a strong driving force for phase separation due to a low miscibility. For example, in the case of region 1 in Fig. 3.3, nucleation of polymer 2 takes place in the polymer 2 -rich phase with the further separation of the blend system because the solvent favors moving to the more familiar polymer 1, forming a "sea," and the other, polymer 2, is densified to become the nuclei, the so-called "island" structure, decreasing the surface tension and interfacial area with a less familiar solvent. Once the nuclei are formed, the system decomposes with a decrease in the free energy, and the nuclei start to grow.

The aim of this study was adopting a space that can contain the electrolyte and solvated Li-ions and modifying that space into a fast ion-transportable channel. The space is created from eliminating the sacrificial polymer component by the post treatment. Therefore, due to difficulties in maintaining a stable 1D fiber structure in a co-continuous phase morphology after eliminating one polymer, the sea-island phase morphology is more suitable for building nanofibers for a fast-charging anode material. Therefore, predicting the phase separation behavior by a ternary phase diagram is crucial for designing fast-ion transportable nanofibers. In general, solvent-evaporation derived phase separation is depicted on a ternary phase diagram as a simple vertical moving of the system composition. However, in the electrospinning system, the actual mechanism that the polymer blend system goes through is more complicated as follows. As the voltage supply to the electrospinning solution increases and surpasses the critical voltage (Vc), the repulsion within the charged polymer overcomes its surface tension; charged jets are ejected from the Taylor cone, and polymer solution is elongated into nanofibers as the solvent is evaporated (Fig. 3.4).

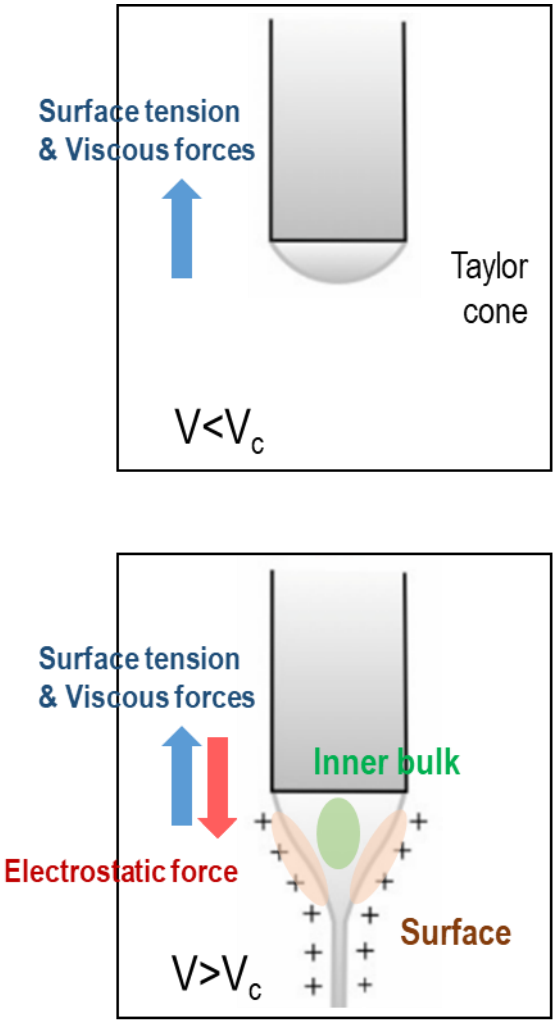

Figure 3.15 A schematic images of the Taylor cone in electrospinning system

In the phase separation process, the Taylor cone is divided into two parts. At the surface of the Taylor cone, the solvent is rapidly evaporated, and the actual polymer blend is phase-separated according to the tie line. However, in the inner part of the Taylor cone, solvent evaporation is not fast enough to separate the phase, and the inner bulk solution replenishes the solvent to the surface of the Taylor cone. As depicted in the ternary phase diagram (Fig. 3.5), the inner bulk solution system is vertically moving downward as the solvent is decreased to replenish the surface, and the phase on the surface is separated. Therefore, when the phase separation occurs as a sea-island structure as we anticipate, the states of each separated sea and island phase are predictable.

a)

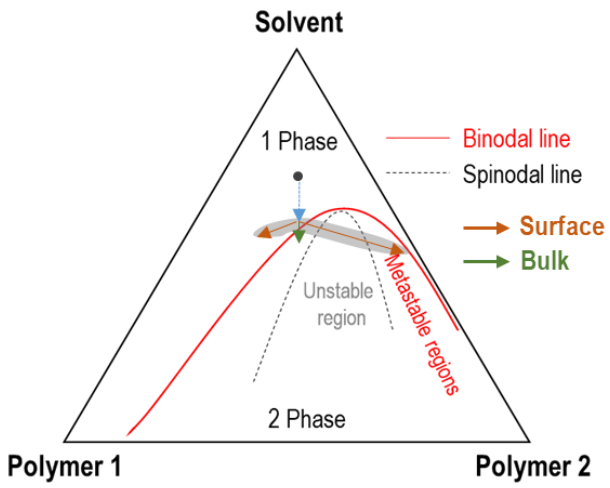

b)

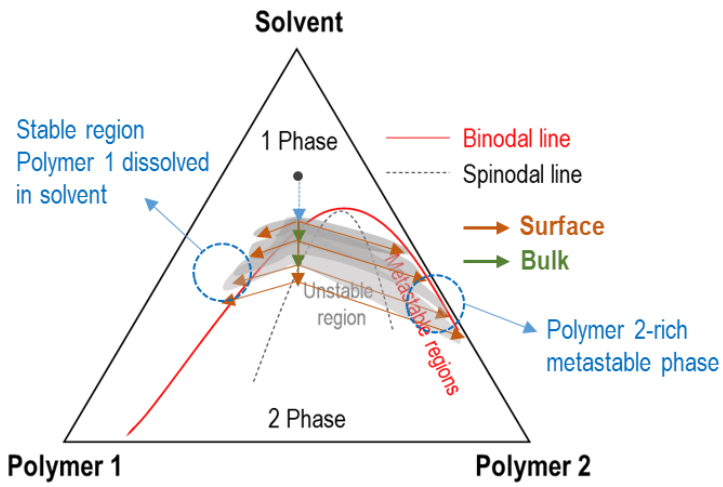

Figure 3.16 Phase separation behavior of immiscible polymer blend system by solvent evaporation (a → b) and subsequent composition change in phase diagram

For example, when the difference of the Flory-Huggins-interaction parameter of two polymers and the same solvent is large between polymer 1 and polymer 2 (when solvent is a better solvent for polymer 1 than for polymer 2), the phase diagram would be asymmetric, highly skewed (Fig. 3.6 b) [14] and expected to have a wide metastable region near the polymer 2 region. In this case, when the polymer 2-rich phase is separated from the polymer blend, it might be in a metastable region unlike polymer 1 which will be in a relatively stable one phase region. This separated metastable phase consist of primarily polymer 2 and also the sub-inclusions of "guest" polymer 1 because the phase is actually not pure with a sole polymer component. This appearance of a guest polymer has an additionally role in the design of carbon nanofibers, such as smaller redox sites or extra ion channels in the nanofibers. Therefore, interpreting the phase separation behavior especially in electrospinning step and considering an additional secondary-micro phase separation enable designing nanofibers with a more complicated morphology.

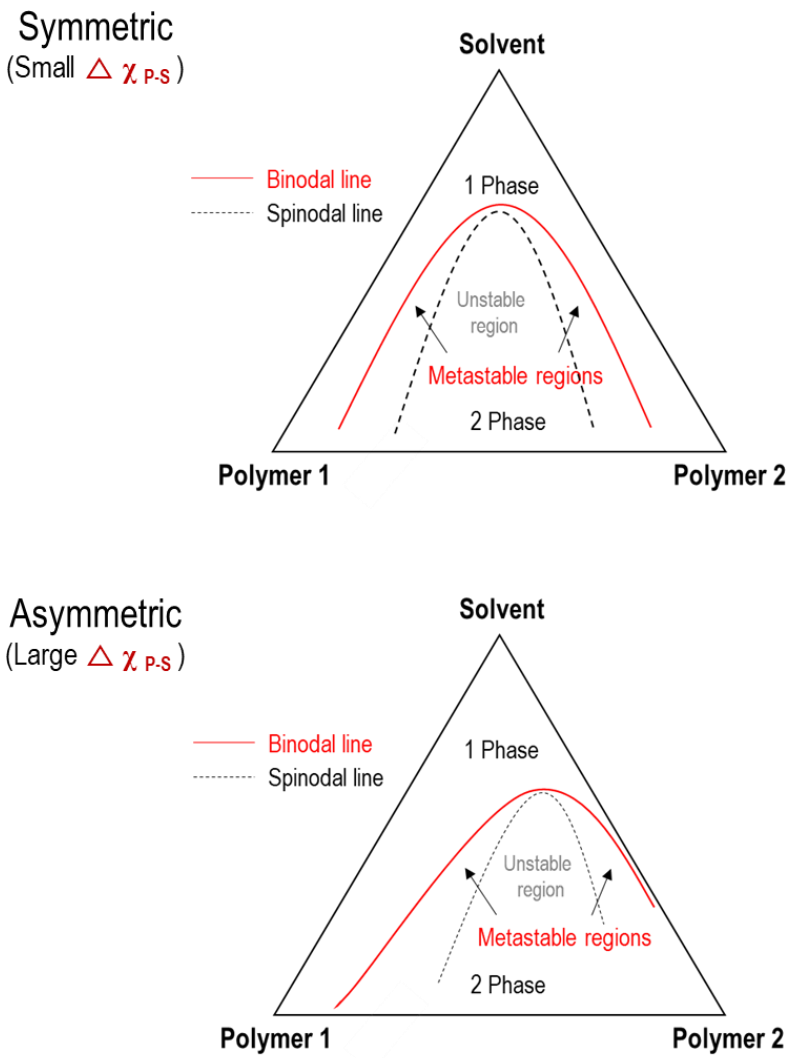

Figure 3.17 A schematic images of ternary phase diagram of polymer blends with (a) high compatibility (low difference in the Flory-Huggins parameter) and (b) low compatibility (high difference in the Flory-Huggins parameter)

Consequently, predicting the phase morphology of an immiscible polymer blend with the Flory-Huggins parameter could be a useful method to design eletrospun nanofibers suitable for fast-charging anode materials. It helps to determine how a polymer blend should be phase separated for electrospinning fast ion transportable CNFs and what kind of polymer and solvent should be used to obtain the ideal phase morphology (Fig. 3.7).

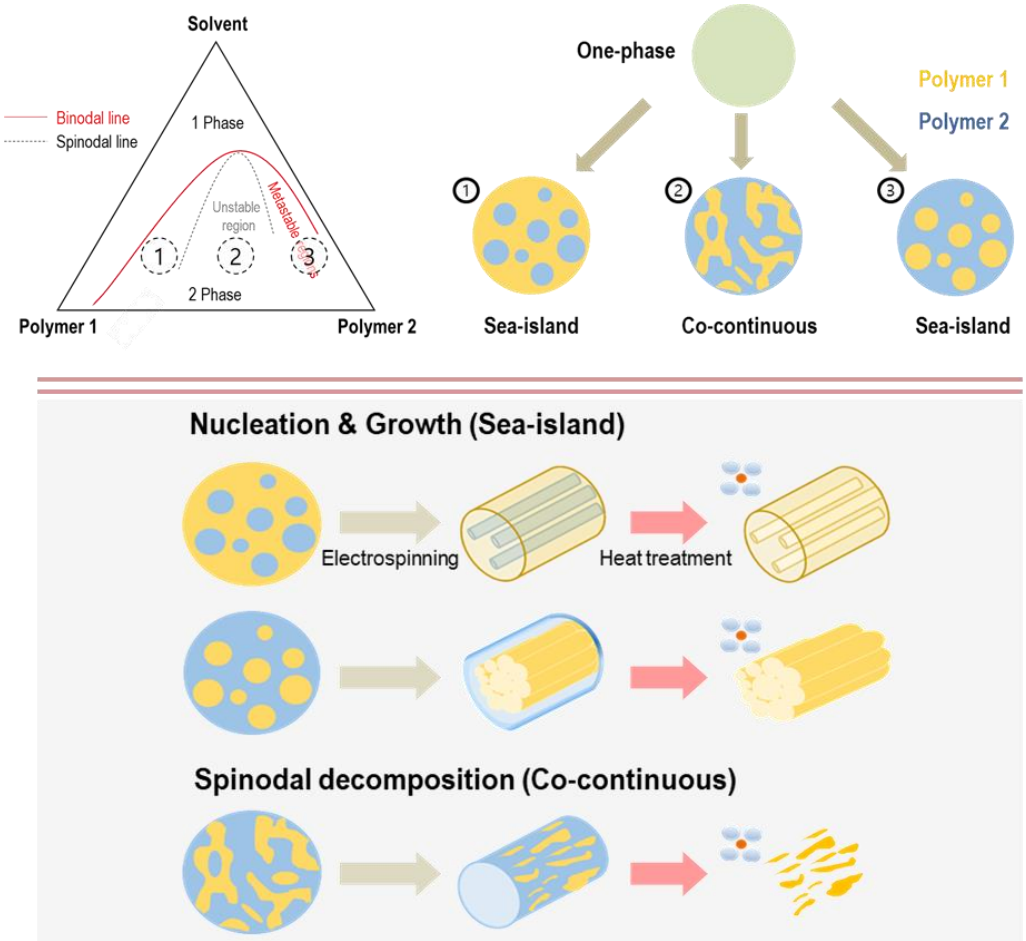

Figure 3.18 Solvent evaporation induced phase separation and subsequent morphology of electrospun nanofiber

3.2 Preparation and characterization of fast solvated Li^+ ion transportable space in CNF

3.2.1 Introduction

Herein, we prepared three types of CNFs with different morphologies, non-porous CNFs, hollow-ion channel CNFs, and CNFs with multi-ion channels, to investigate the effects of the space characteristics of the CNFs on the transport characteristics of the electrochemical species. The CNFs made by single-nozzle electrospinning and a facile method to control the morphology of the CNFs and to make an ion transport channel with an immiscible polymer blend system were investigated through the interpretation of a ternary phase diagram. Through cross-analysis of Brunauer–Emmett–Teller (BET) and the tortuosity value calculation by symmetric cell, the correlation between ion channels made by different phase separation morphologies and the accessibility of each channel was verified. Consequently, the effects of the space characteristics of each of the CNF types on the electrochemical performance such as the rate capability and cycle stability under fast charging conditions are discussed in terms of the transport characteristics of the electrochemical species.

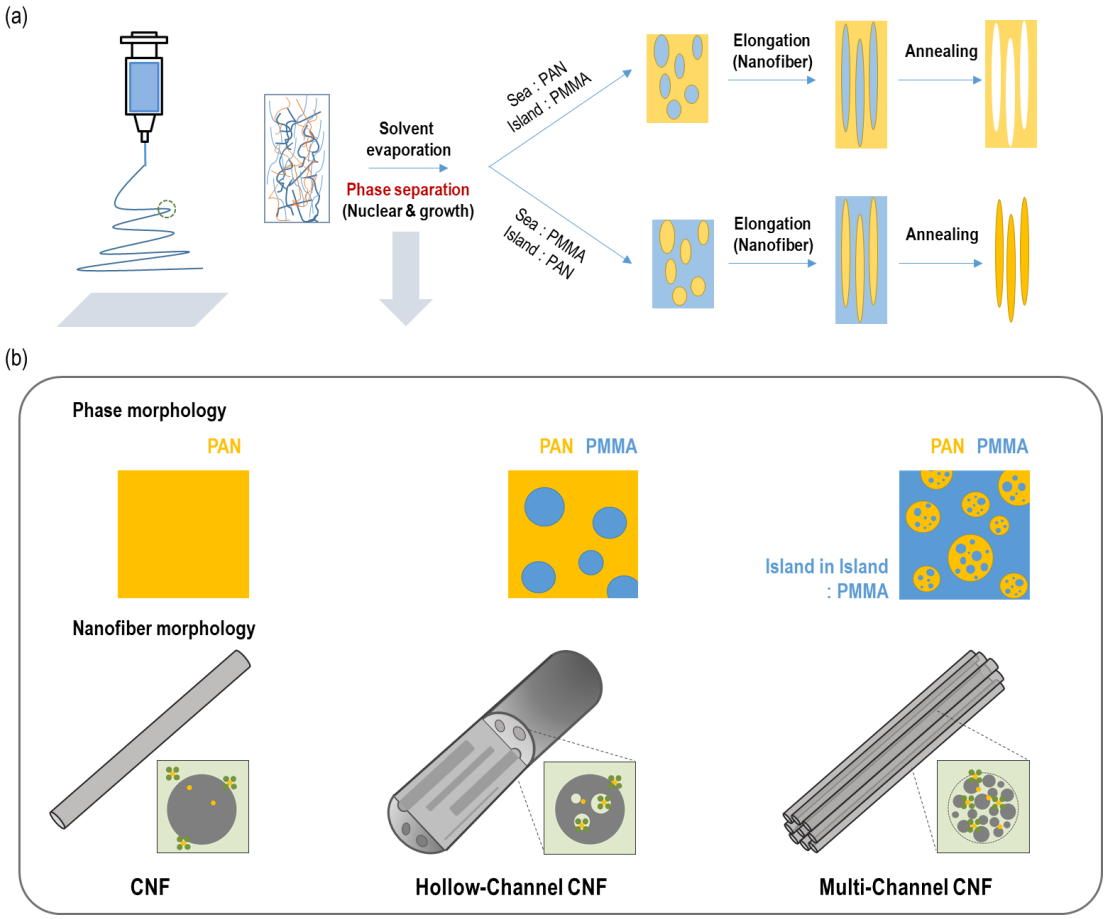

Figure 3.8 Schematic illustration of the (a) electrospinning, subsequent phase separation, elongation and annealing process (b) differences in the both phase and nanofiber morphological properties of the prepared samples

3.2.2 Results and discussion

To investigate the effects of the morphology and space characteristics of the CNFs on the transport characteristics of solvated Li-ions and the subsequent electrochemical performance, CNFs with different morphologies were prepared with the electrospinning method. Additionally, a facile immiscible polymer blend electrospinning method to control the morphology of the CNFs and make solvated Li-ion transport channels in the CNFs was studied. In this study, the main purpose of designing the nanofibers was achieving both fast-ion transport channels and an electron transfer path within porous carbon nanofibers after eliminating one polymer by heat treatment. Polyacrylonitrile (PAN) and poly(methyl methacrylate) (PMMA) were dissolved in N,N′-dimethylformamide (DMF) for an immiscible binary-polymer blend solution. The Flory-Huggins-interaction parameter between PAN and DMF was calculated to be 0.662 and PMMA-DMF 0.229. This value predicts that DMF will be a better solvent for PMMA than for PAN. Because of this large difference in the Flory-Huggins interaction parameter, the phase diagram would be highly skewed [14] and expected to have a wide metastable region near the PAN region (corresponding to polymer 2 in Fig. 3.9).

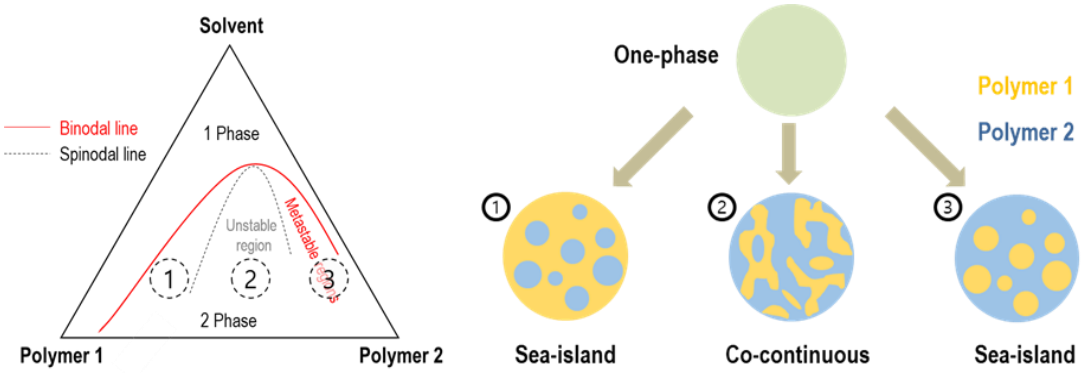

Figure 3.9 Schematic image of ternary phase diagram and subsequent phase separation morphology

As the solvent is rapidly evaporated and the composition changed, the polymer solution will cross the metastable region and separate into 2 phases, each of which constitutes the DMF and PAN or PMMA. To compare with opposite phase morphology, Dimethyl sulfoxide (DMSO) was also selected as a solvent whose Flory-Huggins interaction parameter with PAN is 0.365 and PMMA 0.301 which has a similar χ value. Between two distinguishable kinds of phase morphology (sea-island and co-continuous), there is a problem in that the co-continuous phase has difficulty maintaining the continuous 1D-nanofiber structure after removing the PMMA because it is hard to precisely locate the position of the PMMA in the nanofibers. If PMMA is located too concentrically at a certain point of the nanofiber, its continuous 1D structure would be disconnected after the heat-treatment (Fig. 3.10).

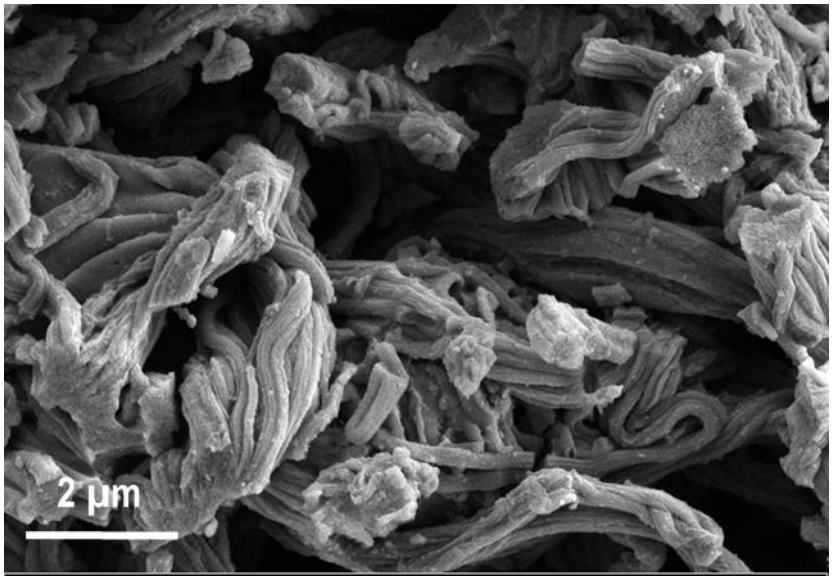

Figure 3.10 Disconnected nanofiber derived from co-continuous phase morphology

Therefore, it is more reasonable to drive the phase separation behavior to be a sea-island structure, as both two expected nanofiber structures in Fig. 3.8a are suitable for a fast-ion and electron transferable structure. When PMMA is the island structure and PAN the sea structure, the obtained nanofibers after heat-treatment are expected to be hollow carbon nanofibers (HC CNF, upper image in Fig. 3.8 a). In contrast, in the case of the PAN-island and PMMA-sea structure, the PMMA can act as a template shell to fabricate elongated PAN islands to become core-located nanofibers. After heat-treatment, the PMMA shell is removed, and elongated thin PAN islands inside the PMMA shell are anticipated to be a bundle of thin carbon nanofibers which could act as redox sites for Li^+ ion storage with much ion-transferable space made by the PMMA (MC CNF, below image in Fig. 3.8 a). To elucidate the role of the ion transferable channels in the nanofibers, non-porous CNFs (CNFs) made with only PAN and DMF solution were also prepared.

The development of the phase separation morphology with solvent evaporation of the PAN/PMMA blend solution was captured using an optical microscope (OM) by spin-coating, whose solvent evaporation process is similar with electrospinning (Fig. 3.11 a-c). The concentration of the PAN/PMMA were 10wt% of PAN and 10wt% of PMMA in both the DMF and DMSO solvent which has an appropriate viscosity for electrospinning. Additionally, the concentration and ratio for both blends were set to be the same to control the amount of each polymer forming nanofibers similarly and to see the effect of the different phase morphologies only. Pure PAN/DMF solution showed a homogeneous 1 phase (Fig. 3.11 a) and the DMSO polymer blend showed the sea (PAN)/ island (PMMA) phase which will be discussed with the corresponding SEM image (Fig. 3.14 b) a little later.

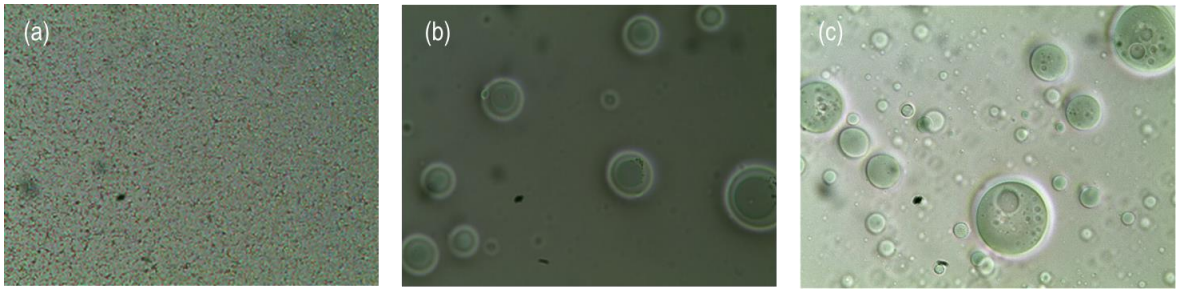

Figure 3.11 Optical micrographs of the phase's morphology of the (a) CNF (PAN 10wt%), (b) HC CNF (PAN 10wt%/PMMA 10wt% in DMSO) (c) MC CNF (PAN 10wt%/PMMA 10wt% in DMF). DMF sample was taken from the opaque (metastable) part at the middle of the solution in a vial after 15 hours when the solution was phase separated.

Noteworthy, in the case of the DMF polymer blend (Fig. 3.11 c), the solution was electrospun not right after stirring but after some time had passed for macro phase separation. Before discussing the phase morphology shown in Fig. 3.11 c, the normal DMF polymer blend should be discussed first. As seen in Fig. 3.12, some of the PAN island have other small phase islands which are secondarily-separated from the PAN islands. This phenomenon is the so called 'phase-in-phase' separation as a result of a viscoelastic micro phase separation process due to strong dynamic asymmetry arising from the glass transition temperature (T_g) and molecular weight differences between the component polymers [14, 15]. This phenomenon is derived from the fact that each separated polymer phase is not "pure" one-phase, which has only one polymer component, but has both primary polymer and sub-inclusions of the other "guest" polymer [14].

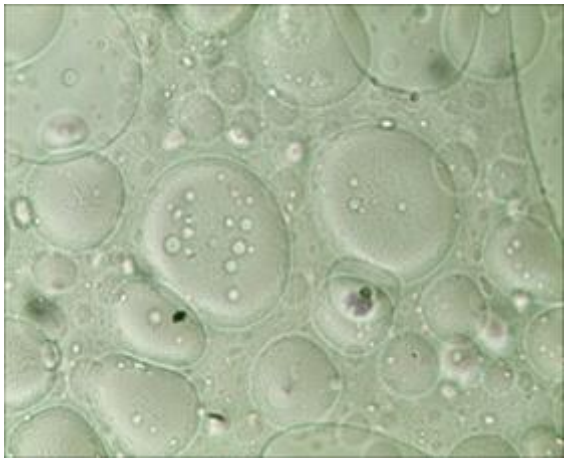

Figure 3.12 Optical micrographs of the phase's morphology of PAN/PMMA/DMF right after stirring

When the solvent is evaporated and the system reaches the metastable region, the phase-separated primary polymer phase continues to expel the guest polymer. In the case of a system whose sea structure consists of a PMMA-rich phase that is more familiar with the solvent and island structure is composed of a PAN-rich phase that is less familiar with the solvent, there is a small amount of guest PMMA in the PAN island. PAN solidifies earlier than PMMA according to their solubility between DMF [16] and starts to freeze as the system reaches the T_g. In this situation, the solvent tends to move from solidifying PAN to PMMA, expelling the guest PMMA from the PAN island, and PMMA is trapped as a small island in the frozen PAN island. This phenomenon is expected to occur in the PAN-island and PMMA-sea case more easily because in the opposite phase, the PMMA island would have a purer phase with less amount of guest PAN inclusions than its counterpart when considering the solubility parameter and phase diagram with the DMF solvent. This phase-in-phase separation of PMMA is anticipated to form additional ion transport channels inside the carbon nanofibers after electrospinning and heat treatment. To maximize this phenomenon which separated the PAN island and included more guest PMMA inside, we simply modified the state of the PAN/PMMA/DMF solution by letting it spontaneously macro phase separate according to time. Before it is completely separated with the pure PAN and PMMA phase, three layers were temporarily separated from the solution (Fig. 3.13). (Because a metastable and unstable solution is thermodynamically unstable, it is spontaneously phase separated over time being stopped to be mixed and then left still.). Interestingly, between the separated PAN and PMMA phases, the intermediate layer of the solution is opalescent in contrast with the transparent PAN and PMMA phase in the upper and bottom layer of the solution, respectively.

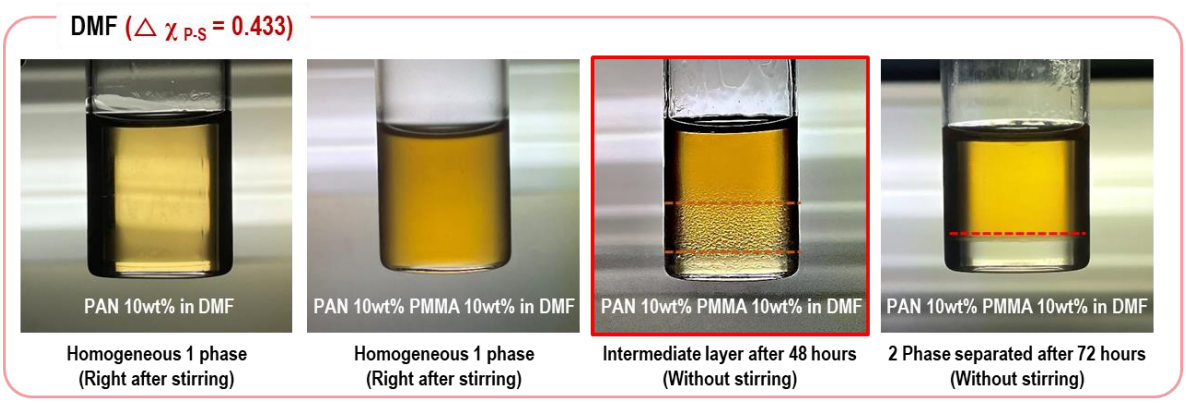

Figure 3.13 Intermediate layer appearance in PAN/PMMA/DMF sample

According to previous turbidity point-based phase diagram research, as incompatibility and instability of the solution arises, the NTU value that quantitatively shows the cloudiness increases, and the solution looks opalescent [17-19]. This phenomenon occurs only when the Flory-Huggins interaction parameter difference between the two polymers and solvent is large as in the case of DMF in this study. Considering 1) the opalescent color of a solution is known for the metastable state in a binary polymer blend (Fig. 3.14) [20] and 2) the intermediate layer is located between the upper PAN phase (low-density) and bottom PMMA (high-density) due to its medium density, it is reasonable to say that the intermediate layer is in the metastable region which has PAN, PMMA and DMF. Furthermore, the PMMA phase was separated early, and there was little change in the height of the bottom layer, but the pure PAN layer was separated upward from the intermediate layer gradually. *Negi et al*. reported this similar phenomenon that among two immiscible polymers, the more compatible polymer with the solvent is separated first, and the other one is gradually separated to one-phase, crossing the metastable region on the ternary phase diagram as the solvent evaporates [21].

(a)

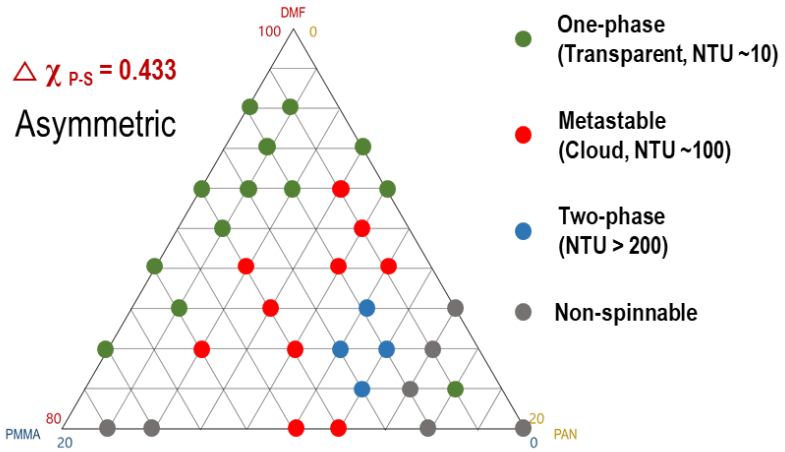

(b)

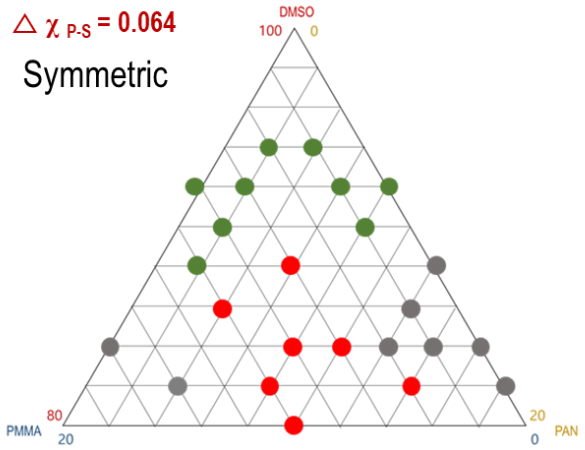

Figure 3.14 NTU-based ternary phase diagram of (a) DMF/PAN/PMMA and (b) DMSO/PAN/PMMA

Therefore, we assumed that this intermediate level in solution might be the concentrated metastable state whose PAN-rich phase still has PMMA inside. As we hypothesized, Fig. 3.11 c shows that the phase in the phase separation of PMMA has increased when the solution is acquired from the intermediate layer, and this result is consistent with the TGA analysis (Fig. 3.15), in that a relative amount of PMMA slightly increased in the MC CNF sample considering that PMMA is decomposed at 3-400 ℃. In Fig. 3.16 a-b, when the island phase is frozen as the solvent is evaporated, there is a coffee ring effect for which the height is high on both sides. However, the phase-in-phase, which is inside of the island phase, does not show the coffee ring effect (Fig. 3.16 c-d). Because this phenomenon is caused by the relocation of the solvent when the primary polymer is frozen as the solvent is evaporated, the coffee ring effect is not visible due to the remaining solvent.

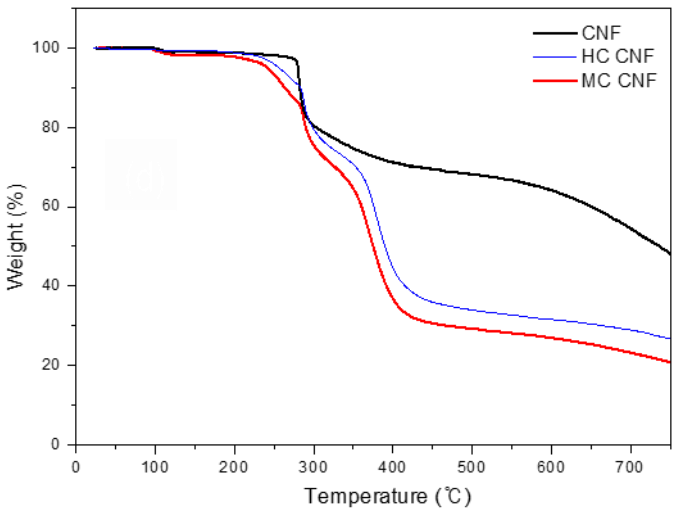

Figure 3.15 TGA plot of the mass loss of each sample

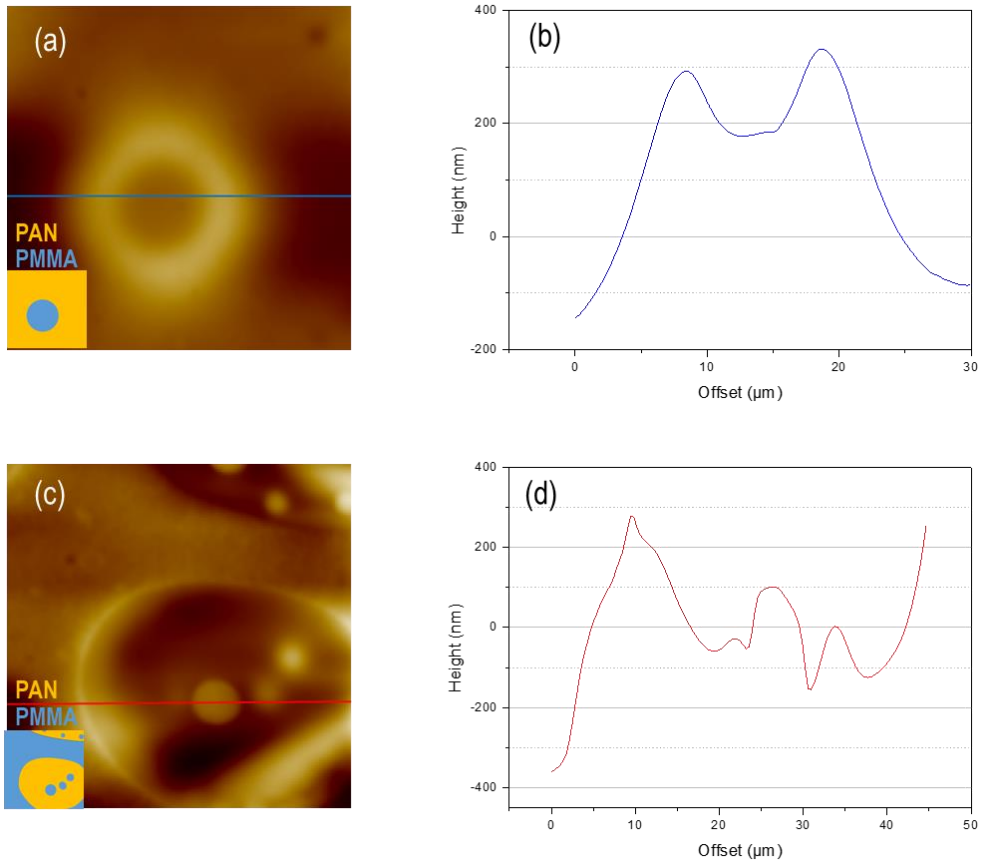

Figure 3.16 Atomic force microscopy (AFM) image and line scan of (a, b) HC CNF and (c, d) MC CNF. Each sample was prepared by spin coating with a similar solvent evaporation condition during electrospinning.

Consequently, three nanofibers were prepared with distinctly different morphologies (Fig. 3.17), corresponding with each phase morphology. The MC CNFs are a bundle of thin nanofibers containing an empty space between each nanofiber. The HC CNFs have a hollow space confined in the nanofibers. CNFs were electrospun with PAN only which have no ion channels inside for comparison. Both sets of empty space in the MC CNFs and HC CNFs are expected to act as transport channels for solvated Li-ions. However, even if both nanofibers have empty space in each of them, the accessibility to the ion channels is expected to be different. As seen in Fig. 3.17 d, the MC CNFs have extra space between the individual nanofibers which is anticipated to connect the bulk electrolyte with the ion channels inside the nanofibers. However, even though the HC CNFs have empty space inside the nanofibers, if the nanofibers are not cut accidently, solvated-Li ions cannot easily access the inside of the nanofibers because the HC CNFs have no additional pores to connect the ion channels with the bulk electrolyte. This space characteristics of the HC CNFs could make the solvated Li-ions path more tortuous, subsequently needing more time to make redox reactions or even worse, the space might not be utilized in fast-charging conditions.

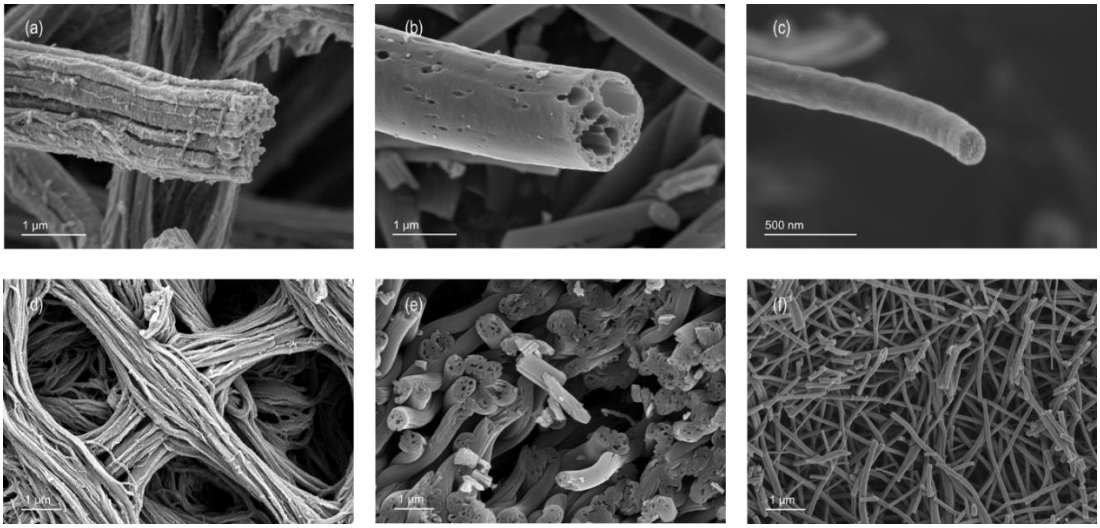

Figure 3.17 FE SEM images of (a, d) MC CNF, (b, e) HC CNF and (c, f) CNF in (a, b, c) high resolution and (d, e, f) low resolution, respectively

To measure the space characteristics of each nanofiber sample, BET analysis was conducted. It could provide hints on ion accessibility because whether gas molecules could access the absorbent would be applied to the case of solvated Li^+ ions. Subsequently, pores originating from various spaces in the nanofibers were confirmed by the pore size distribution based on the Original Density Functional Theory (Fig 3.18), N_2 adsorption/desorption isotherm characterization (Fig. 3.19 a-c). An analysis of the BET SSA and pore volume data (Fig. 3.18 and Table 1) revealed that the elongated PMMA phase in the electrospun nanofibers successfully decomposed into empty space in the nanofibers, considering that pore size distribution is distinguishable based on the criteria of 10 nm depending on the presence of PMMA in the polymer blend.

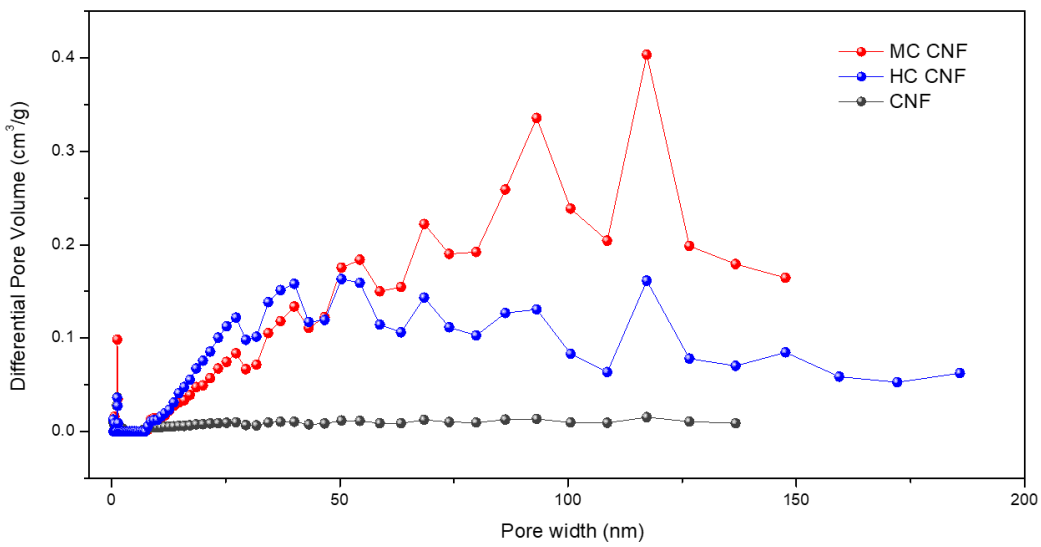

Figure 3.18 Differential pore volume vs pore width for each sample based on the original density functional theory

Table 3.2 Specific Surface Area and Pore Volume of each sample

	Specific surface area (m^2 g^{-1})	Pore volume (cm^3 g^{-1})
CNF	10.16	0.02
HC CNF	23.151	0.15
MC CNF	47.47	0.21

These newly generated space should be interpreted as a Li-ion transportable channel when considering the size of solvated Li^+ ions [22]. Furthermore, the MC CNFs have a larger surface area and pore volume compared to the HC CNFs (Table 1), especially pores whose sizes are above approximately 50 nm (Fig. 3.18). Considering the MC CNFs and HC CNFs are collected from the same amount of polymer and the empty space in the nanofibers is a result of the decomposition of the phase separated PMMA, this morphological difference is caused by the phase morphology. This structural difference was consistent with the SEM images in Fig. 3.17 a-f in which the MC CNFs have many 'exposed' spaces that gas molecules can access more directly, and the HC CNFs have channels inside the CNFs, but molecules might have difficulties accessing them to get inside the nanofibers

To identify the geometrical characteristics of each nanofiber, the adsorption/desorption isotherm was collected (Fig. 3.19 a-c). Except for the CNF sample which has little pores inside, both the MC CNFs/HC CNFs show common characteristics of H1 type hysteresis for which the adsorption/desorption curve increases rapidly and synchronously at a P/P_0 = 0.8 approaching to 1.0 [23]. This type suggests that the reduced distribution of the pore diameter, corresponding to cylindrical pores with a pore size distributed in the 50–200 nm range [24, 25], is a reasonable result because the elongated PMMA phase in the nanofibers would be converted to a cylindrical space in the CNFs after the heat treatment.

Interestingly, there is difference in the closure of the hysteresis loop below P/P_0=0.8. The adsorption curve and desorption curve meeting as pore filling is done at P/P_0=1, and the mechanism of desorption moves from meniscus development to recovery of multilayer adsorption [26]. Therefore, where the loop closes indicates the presence of additional pores which have a corresponding size and shape in the material [27, 28]. In Fig. 5 c-d, the adsorption curve and desorption curve of the HC CNFs meets at approximately P/P_0=0.8. However, the MC CNFs still have an unclosed hysteresis loop below P/P_0=0.8. In this range of relative pressure, the shape of the pore is known for a parallel or tapered plate and slit-shape [29, 30], whose size is smaller than a cylindrical pore considering that pore filling occurs on a continuum. These pores are assumed to be made by the phase-in-phase separated PMMA because it only appears in the MC CNFs even though the HC CNFs have the same amount and ratio of PAN/PMMA.

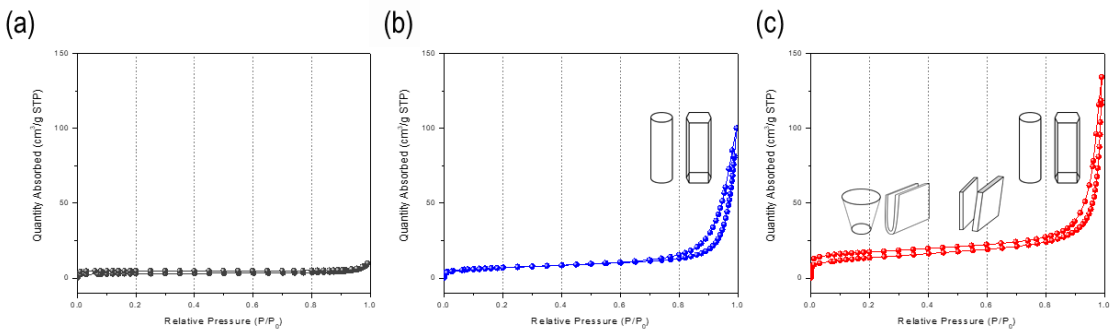

Figure 3.19 N_2 adsorption/desorption isotherm of (a) CNF, (b) HC CNF, (c) MC CNF

To elucidate whether the presence and accessibility of the ion channel actually affects the transport of the solvated Li-ions under the fast-charging condition, Fig 3.20 presents data we prepared showing the transport characteristics of each sample. Electrochemical impedance spectroscopy (EIS) was conducted for two types of cells; symmetric cell (CF electrode||CF electrode) and half cell (Li||CF electrode). Symmetric cell EIS was measured for calculating the tortuosity (τ), and half-cell was measured for calculating the impedance and Li-ion diffusion coefficient [22]. The difference between the tortuosity and diffusion coefficient is that the tortuosity describes the behavior of solvated Li-ions in the electrolyte phase, and the diffusion coefficient (D_{Li}) describes the behavior of both desolvated and solvated Li-ions [31]. Fig. 3.20 a shows a Nyquist plot for a symmetric cell, and $R_{ion}/3$, which describes the ionic resistance in an electrolyte containing space, was derived to be 2.82, 3.90 and 3.49 Ω for the MC CNFs, HC CNFs and CNFs, respectively. The tortuosity value was calculated by Equation 5 and shown in Fig. 3.20 d. Tortuosity is the ratio between the thickness of the electrode and the length of the pore path. In this study, the electrode thickness was set to be same, and this dimensionless parameter indicates how the solvated Li-ions are transport through the space in an active material more directly.

$$\tau = \frac{R_{ion}\, A\, \kappa\, \varepsilon}{2d}$$

The tortuosity of each sample is 9.36 for the CNFs, 6.16 for the HC CNFs and 3.90 for the MC CNFs, indicating the MC CNFs have the shortest and direct solvated Li-ion transport path. Considering the SEM images (Fig. 3.17) and BET data (Fig. 3.18-12), multi exposed ion channels in the MC CNFs helped to transport quickly the successfully solvated Li-ions. In the case of the HC CNFs whose ion channels are confined in the CNFs, the solvated Li-ions had to take a detour to access the active sites because there is no other space to connect the bulk electrolyte and hollow inner space. Additionally, considering the diffusion coefficient is expressed with the tortuosity ($\tau^2 = D/D_e$, where τ is tortuosity; D is the diffusion coefficient in the electrode species in the electrolyte, and D_e is the effective diffusion coefficient [32]) and the diffusion coefficient value (Fig. 3.13 e-h) with the corresponding Nyquist plot through the half cell (Fig. 3.13 b-c), it is reasonable to say that fast-transport of solvated Li-ions to the interface affects the transport behavior after the desolvation process too.

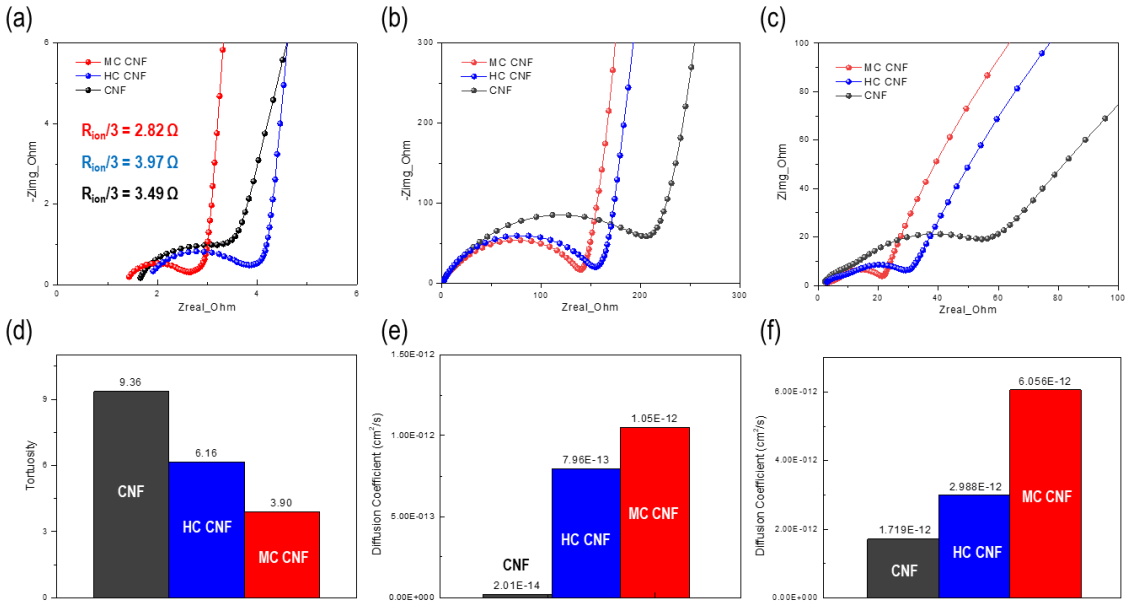

Figure 3.20 (a) Electrochemical impedance spectroscopy (EIS) of symmetric cells of each sample for R_{ion} and (d) subsequent tortuosity calculation; EIS analysis of each sample for Li ion diffusion coefficient calculation of (b, e) before cycling, and (c, f) after cycling

Cyclic voltammetry of each sample at 5mV s^{-1} (Fig. 3.21 a), and corresponding tafel plot (Fig. 3.21 b) show that the exchange current density (j_0) of the MC CNFs (0.681 mA cm^{-2}) is higher than those of the others (0.123 mA cm^{-2} for the CNFs and 0.136 mA cm^{-2} for the HC CNFs). This is consistent with the fact that the transport of solvated Li-ions to the surface of an active material affects the uniformity of the surface charge distribution. Accordingly, the MC CNFs, which are anticipated to have the most even concentration gradient and current distribution, had an enhanced charge transfer reaction and subsequently a stable SEI layer formation (Table 2 and Fig. 3.22 a-c). These results are meaningful in that the charge transfer and SEI layer formation are enhanced by the Li ion transport not the electrical conductivity as previously known. As shown in Fig. 3.22 a-c, the electrodes after 500 cycles under the fast charging condition (1000 mA g^{-1}) show that the MC CNFs have the most stable and thin SEI layer with no channel clogging compared to that of the CNFs and HC CNFs whose SEI layers seemed thick and irregular, clogging the existing channels and pores.

Table 3.2 Charge transfer resistance (R_{CT}) and SEI resistance (R_{SEI}) before and after cycling

	R_{CT} (before cycling)	R_{CT} (After cycling)	R_{SEI}
CNF	257.60	132.99	47.76
HC CNF	168.13	53.20	23.79
MC CNF	149.58	35.85	16.88

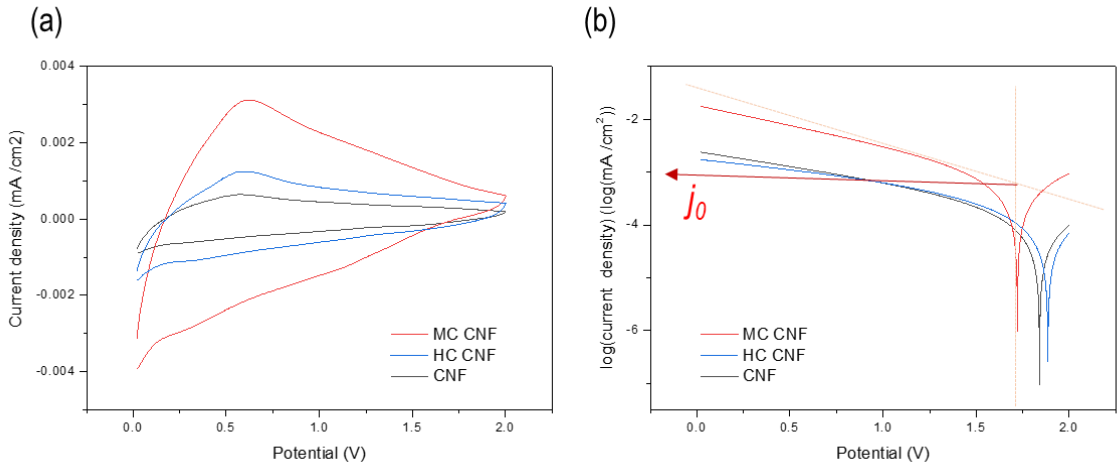

Figure 3.21 (a) Cyclic voltammograms (CVs) of each sample at 5mV s^{-1}**; (b**) Tafel plot of each sample plot (j_0 stands for exchange current density)

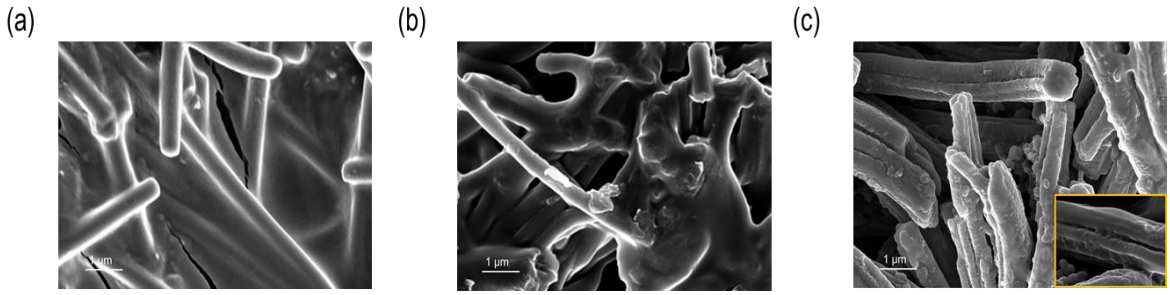

Figure 3.22 FE-SEM images of electrodes after 500 cycles under fast charging conditions (1000mA g^{-1}) for (a) CNF, (b) HC CNF, and (c) MC CNF

The rate performance from 0.1 to 2 A g^{-1} and coulombic efficiency of the half-cell are shown in Fig. 3.23. At 100 mA g^{-1}, the storage capacity increased, respectively, by 62 % and 24 % for the MC CNFs and HC CNFs compared to the non-porous CNFs. Interestingly, at a higher current density (2000 mA g^{-1}), the capacity increase was higher (277 % and 167 %, respectively) which implies the importance of a fast ion transport under the fast charging condition.

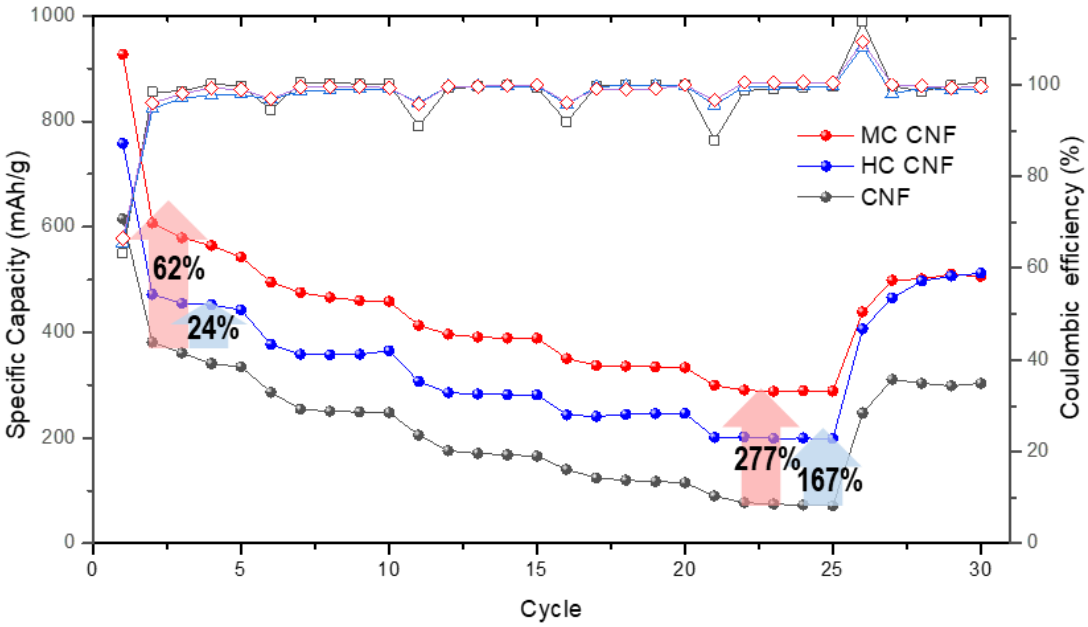

Figure 3.23 Electrochemical test results of each sample at varying current densities (100, 200, 500, 1000, 2000, and 10 mA g^{-1}, respectively)

Furthermore, with a normalized capacity per surface area, the CNF sample represents severe capacity degradation even at a low current density, and the MC CNFs and HC CNFs show a better rate performance (Fig. 3.24 a). Even though both the MC CNFs and HC CNFs have ion channels, the MC CNFs delivering capacities of 607.2, 495, 413.1, 350.3 and 299.7 mAh g^{-1} at 0.1, 0.2, 0.5, 1 and 2 A g^{-1} are superior to the HC CNFs for both capacity and rate capability on a high current density. Furthermore, the 'R-ratio,' which is derived to verify the effect of the ion channels compared to the non-porous CNFs, indicates that the effect of the ion channels on the rate capability is clear, and the gap between the MC CNFs and HC CNFs is increasing as the current density goes higher (Fig. 3.24 b). This result is consequently explained by the overpotential value with each current density calculated from the *dQ/dV* data (Fig. 3.25). In Fig. 3.24 c, the overpotential value increases with a higher current density, and the amount of increased overpotential is large in ascending order of the CNFs, HC CNFs and MC CNFs. Comparing that the CNFs have a high overpotential even at a low current density, the overpotential of the HC CNFs started to increase at a relatively higher current density (about 1 A mg^{-1}).

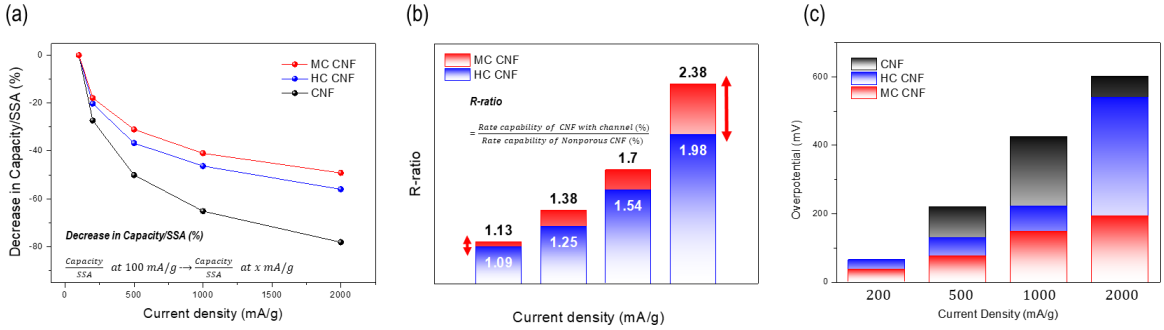

Figure 3.24 (a) Decrease in specific capacity from 100 mA/g to 500, 1000, 2000 mA g-1 of each sample; (b) Rate capability increase compared to non-channel CNF (R-ratio) according to current density; (c) Overpotential according to current density

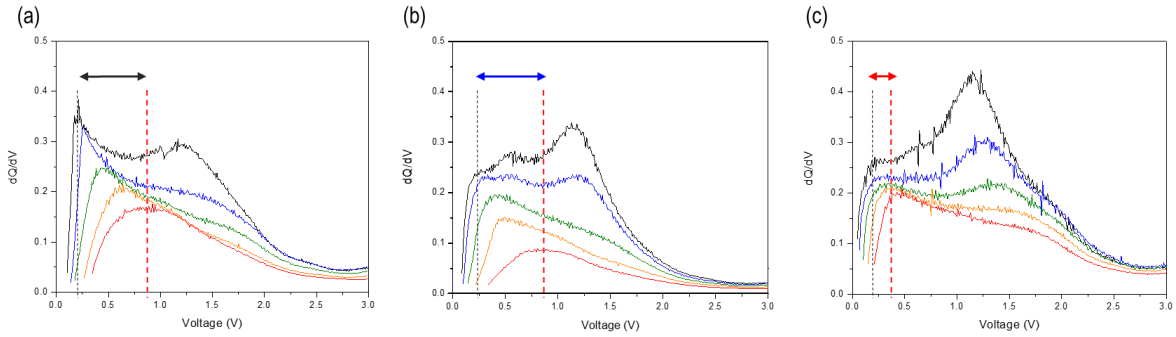

Figure 3.25 dQ/dV plots of (a) CNF, (b) HC CNF, (c) MC CNF electrode. Arrow between shifted peaks from 100 mA g-1 to 2000 mA g-1 indicates degree of overpotential

This result proves that not just the presence but also the accessibility of the ion channels acts to reduce the overpotential of the active material and subsequently improves the electrochemical performance in the fast charging condition. The effect of ion-transport on the long term cycle stability was also measured (Fig. 3.26). The MC CNFs has the best cycle stability maintaining 91% of the capacity after 500 cycles compared to 48% and 61% maintained by the HC CNFs and CNFs. It is interesting that the HC CNFs have the worst structural stability during the repeated charging/discharging process showing that capacity degradation starts early at around 200 cycles. This result indicates that in contrast to the CNFs which have a low initial Li-ion storage, the HC CNFs have more capacity reduction due to the continuous pore clogging caused by the irregular formations of the SEI layer. Therefore, the redox sites of the HC CNFs are continuously clogged, and the capacity of the HC CNFs eventually becomes similar to that of the CNFs after 500 cycles.

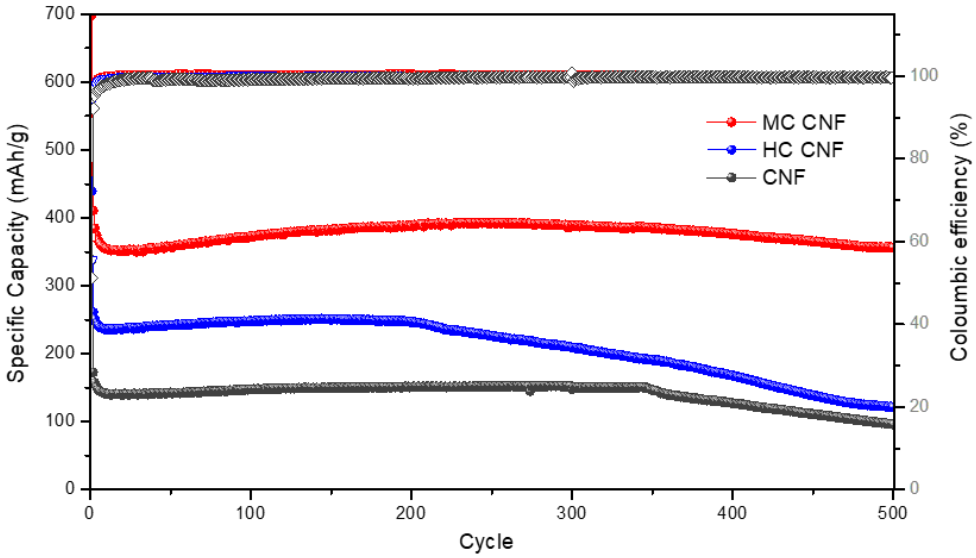

Figure 3.26 Cycling stability test results of each sample at a high current density of 1000 mA g^{-1}

3.3 Conclusion

Phase separation behavior in polymer blend electrospinning could make fast electrochemical species transportable morphology of carbon nanofiber, which is a good candidate for fast charging anode materials. In order to control and design phase-separated electrospun nanofibers, ternary phase diagram and subsequent phase morphology were predicted based on the Flory-Huggins interaction parameter. Between co-continuous phase and sea-island phase, sea-island phase separation morphology is anticipated to make fast ion transportable "channel" in CNF. Phase separation behavior of immiscible polymer blend system by solvent evaporation and subsequent composition change in ternary phase diagram were predicted according to the state of Taylor cone and corresponding solvent movement. Considering phase transition to the metastable region in asymmetric phase diagram, the method for secondary-micro phase separation by expelling guest polymer is investigated to build additional ion transport channel in CNF. Consequently, predicting the phase morphology of an immiscible polymer blend with the Flory-Huggins parameter could be a useful method to design eletrospun nanofibers suitable for fast-charging anode materials. It helps to determine how a polymer blend should be phase separated for electrospinning fast ion transportable CNFs and what kind of polymer and solvent should be used to obtain the ideal phase morphology.

In this study, we interpreted the difference in the electrochemical environment between normal and fast charging conditions in terms of the overpotential by the transport limit of Li-ions. A rational way to design fast-charging anode materials that have multi-ion channels for solvated Li-ion transport was suggested. A facile method to control the morphology of CNFs with an immiscible polymer blend electrospinning system was investigated through the interpretation

of the ternary phase diagram. Effects of the morphology and space characteristics of each CNF sample on the electrochemical performance including the rate capability and cycle stability under fast charging conditions are discussed in terms of the transport characteristics of the electrochemical species in different types of ion channels. As a result, MC CNFs, which have exposed ion transport channels within the thin nanofibers, had a high rate capability whose reversible capacity is 607.2 at 0.1 A g^{-1} and 299.7 mAh g^{-1} at a high current density of 2 A g^{-1}, showing the lowest overpotential resistance than the same material with a different CNF morphology and space characteristics. Moreover, the charge transfer and SEI layer formation are both enhanced by an even surface charge distribution from the enhanced solvated Li-ion transport subsequently leading to a stable cycle stability, which decreased only 9% after 500 cycles. These improvements are due to the presence of the ion transport channels in the CNFs and the high accessibility of the exposed multi-channel structure. This study not only suggests a simple phase separation derived from the electrospinning method but also confirms the effects of the morphology of the CNFs on the transport characteristics of Li-ions under fast charging conditions.

3.4 Experimental section

3.4.1 Materials and Electrodes Characterization

Chemicals and Materials. Polyacrylonitrile [PAN; molecular weight (Mw) of 150,000; Aldrich], poly(methyl methacrylate) (PMMA; Mw 120,000; Aldrich, N,N′-dimethylformamide (DMF; Daejung, Korea). The sample name is denoted as follows. To prepare the electrospinning dope solution, specified amounts of PAN, the orientation controlling polymer, were dissolved in 10 mL of DMF with stirring at 90 °C for 4 h. After the PAN was fully dissolved into the solution by tip-sonication for 1 h and ultra centrifuged at 5000 rpm for 40 min. Finally, specific amounts of PMMA, which make 20 wt % of the total polymer concentration with PAN, were dissolved overnight into the solution. The electrospinning dope solution was loaded into a syringe connected to a metal needle (gauge no. 28, inner diameter of 0.18 mm) nozzle and electrospun at a rate of 1.0 mL h−1 in air at a voltage of 19.5 kV The distance from the nozzle to the grounded collector was approximately 18 cm, and the temperature was approximately 22−25 °C with 18−20% relative humidity.

After the electrospinning step, electrospun fiber was heated to 750 °C in a nitrogen atmosphere at a heating rate of 5 °C/min and maintained at that temperature for 4 h to fully decompose PMMA with PAN. Finally, activated partially PCNFs was obtained after drying at 80 °C overnight.

3.4.2 Characterization

Volumetric nitrogen adsorption isotherms (at 77 K) up to 1 bar were measured using a Micromeritics ASAP 2020 static volumetric gas adsorption instrument, preliminarily outgassed for 10 h at 150 °C. The specific surface areas and pore volume distributions were examined based on the BET equation [16] using a Micromeritics ASAP 2020 static volumetric gas

adsorption instrument. The morphologies of the bare material and synthesized materials were analyzed by field-emission scanning electron microscopy (FE-SEM, SIGMA: Carl Zeiss,).

An optical microscope (Olympus, BX-51) with polarizers was used to observe the polymer phase separation. FESEM (MERLIN Compact) were conducted to verify the 1D morphologies of the samples. In addition, to determine how much the electrical conductivity can be enhanced by incorporating CNFs uniaxially, the samples were pelletized and measured using a M4P-205 4-point probe station (MSTECH). The specific surface areas and pore volume distributions were examined based on the BET equation82 using a Micromeritics ASAP 2020 static volumetric gas adsorption instrument.

3.4.3 Electrochemical Measurements

Analyzing the electrochemical performance of the prepared samples, the electrodes were all prepared using the doctor blade method with 1~1.5mg cm^{-2} loading mass, polyvinylidene fluoride (15 wt %), carbon black (15 wt %), and active material (70 wt %). Coating the prepared slurry onto a copper current collector and vacuum drying it for 12 h at 80 °C. The electrolyte was 1 M $LiFP_6$ in EC/DEC (1:1 volume ratio). The electrochemical test was performed using a battery cycler (WBCS3000, WonATech) and a potentiostat (ZIVE SP2, WonATech) with assembled 2032 coin-type half-cells. The electrochemical performance tested over a voltage range between 0.02−2.0 V against Li/Li^+ and cyclic voltammetry were measured at a scanning rate of 5 mV s^{-1} between 0.02 and 2 V versus Li/Li+. Electrochemical impedance spectra were obtained at the open circuit voltage over the frequency range of 10 mHz to 10 kHz with an AC amplitude of 5 mV.

3.5 References

[1] J.T. McCann, D. Li, Y. Xia, Electrospinning of nanofibers with core-sheath, hollow, or porous structures, Journal of Materials Chemistry 15(7) (2005) 735-738.

[2] X. Fan, L. Zou, Y.-P. Zheng, F.-Y. Kang, W.-C. Shen, Electrospinning Preparation of Nanosilicon/Disordered Carbon Composite as Anode Materials in Li-Ion Battery, Electrochemical and Solid-State Letters 12(10) (2009) A199.

[3] D. Li, Y. Xia, Electrospinning of Nanofibers: Reinventing the Wheel?, Advanced Materials 16(14) (2004) 1151-1170.

[4] J.T. McCann, M. Marquez, Y. Xia, Highly Porous Fibers by Electrospinning into a Cryogenic Liquid, Journal of the American Chemical Society 128(5) (2006) 1436-1437.

[5] Y.K. Doğan, A. Demirural, T. Baykara, Single-needle electrospinning of PVA hollow naofibers for core–shell structures, SN Applied Sciences 1(5) (2019) 415.

[6] R. Singh, F. Ahmed, P. Polley, J. Giri, Fabrication and Characterization of Core–Shell Nanofibers Using a Next-Generation Airbrush for Biomedical Applications, ACS Applied Materials & Interfaces 10(49) (2018) 41924-41934.

[7] P. Tipduangta, P. Belton, L. Fábián, L.Y. Wang, H. Tang, M. Eddleston, S. Qi, Electrospun Polymer Blend Nanofibers for Tunable Drug Delivery: The Role of Transformative Phase Separation on Controlling the Release Rate, Molecular Pharmaceutics 13(1) (2016) 25-39.

[8] L. Martinova, D. Lubasova, Reasons for using polymer blends in the electrospinning process, AIP Conference Proceedings 1502(1) (2012) 115-128.

[9] M.J. Akanbi, S.N. Jayasinghe, A. Wojcik, Characterisation of electrospun PS/PU polymer

blend fibre mat for oil sorption, Polymer 212 (2021) 123129.

[10] X. Zhang, L. Ji, O. Toprakci, Y. Liang, M. Alcoutlabi, Electrospun Nanofiber-Based Anodes, Cathodes, and Separators for Advanced Lithium-Ion Batteries, Polymer Reviews 51(3) (2011) 239-264.

[11] W. Lee, Y. Park, Organic Semiconductor/Insulator Polymer Blends for High-Performance Organic Transistors, Polymers 6 (2014) 1057-1073.

[12] D.R. Paul, Chapter 16 - Fibers from Polymer Blends, in: D.R. Paul, S. Newman (Eds.), Polymer Blends, Academic Press1978, pp. 167-217.

[13] J. Zhang, J. Nie, Transformation of complex internal structures of poly(ethylene oxide)/chitosan oligosaccharide electrospun nanofibers, Polymer International 61 (2012).

[14] J.-S. Kim, P.K.H. Ho, C.E. Murphy, R.H. Friend, Phase Separation in Polyfluorene-Based Conjugated Polymer Blends: Lateral and Vertical Analysis of Blend Spin-Cast Thin Films, Macromolecules 37(8) (2004) 2861-2871.

[15] J. Joy, K. Winkler, K. Joseph, S. Anas, S. Thomas, Epoxy/methyl methacrylate acrylonitrile butadiene styrene (MABS) copolymer blends: reaction-induced viscoelastic phase separation, morphology development and mechanical properties, New Journal of Chemistry 43(23) (2019) 9216-9225.

[16] C. Hong, K.S. Yang, S. Oh, H.-J. Ahn, B. Cho, C. Nah, Effect of blend composition on the morphology development of electrospun fibres based on PAN/PMMA blends, Polymer International 57 (2008) 1357-1362.

[17] M. Bognitzki, T. Frese, M. Steinhart, A. Greiner, J. Wendorff, A. Schaper, M. Hellwig,

Preparation of fibers with nanoscaled morphologies: Electrospinning of polymer blends, Polymer Engineering & Science 41 (2001) 982-989.

[18] N. Posharnowa, A. Schneider, M. Wünsch, V. Kuleznew, B.A. Wolf, Polymer–polymer interaction parameters for homopolymers and copolymers from light scattering and phase separation experiments in a common solvent, The Journal of Chemical Physics 115(20) (2001) 9536-9546.

[19] E. Pavlova, I. Nikishin, A. Bogdanova, D. Klinov, D. Bagrov, The miscibility and spatial distribution of the components in electrospun polymer–protein mats, Rsc Advances 10(8) (2020) 4672-4680.

[20] E. Rezabeigi, P. Wood-Adams, R. Drew, Isothermal ternary phase diagram of the polyactic acid-dichloromethane-hexane system, Polymer 55 (2014).

[21] V. Negi, O. Wodo, J.J. van Franeker, R.A.J. Janssen, P.A. Bobbert, Simulating Phase Separation during Spin Coating of a Polymer–Fullerene Blend: A Joint Computational and Experimental Investigation, ACS Applied Energy Materials 1(2) (2018) 725-735.

[22] J. Kim, H.I. Cho, Y.S. Cho, S.H. Lee, C.R. Park, New insights into the effects of available space characteristics within graphite-based anodes on the accessibility of solvated Li-ions under fast charging conditions, Carbon (2022).

[23] K. Kaneko, Determination of pore size and pore size distribution: 1. Adsorbents and catalysts, Journal of Membrane Science 96(1) (1994) 59-89.

[24] Z. Wang, X. Jiang, M. Pan, Y. Shi, Nano-Scale Pore Structure and Its Multi-Fractal Characteristics of Tight Sandstone by N2 Adsorption/Desorption Analyses: A Case Study of Shihezi Formation from the Sulige Gas Filed, Ordos Basin, China, Minerals, 2020.

[25] M. Thommes, K. Kaneko, A.V. Neimark, J.P. Olivier, F. Rodriguez-Reinoso, J. Rouquerol, K.S.W. Sing, Physisorption of gases, with special reference to the evaluation of surface area and pore size distribution (IUPAC Technical Report), 87(9-10) (2015) 1051-1069.

[26] L.A.G. Aylmore, Hysteresis in gas sorption isotherms, J Colloid Interf Sci 46(3) (1974) 410-416.

[27] F. Sotomayor, K. Cychosz, M. Thommes, Characterization of Micro/Mesoporous Materials by Physisorption: Concepts and Case Studies, (2018).

[28] Y. Yuan, F. Cai, L. Yang, Pore structure characteristics and fractal structure evaluation of medium- and high-rank coal, Energy Exploration & Exploitation 40(1) (2021) 328-342.

[29] B. Xue, J. Zhang, X. Tang, C. Yang, Q. Chen, X. Man, W. Dang, Micro-pore Structure and Gas Accumulation Characteristics of Shale in the Longmaxi Formation, Northwest Guizhou, Petroleum Research 1 (2016) 191-204.

[30] D. Zhang, J. Meegoda, B. Silva, L.-m. Hu, Impact of de-ionized water on changes in porosity and permeability of shales mineralogy due to clay-swelling, Scientific Reports 11 (2021) 20049.

[31] L. Borchardt, D. Leistenschneider, J. Haase, M. Dvoyashkin, Diffusion: Revising the Concept of Pore Hierarchy for Ionic Transport in Carbon Materials for Supercapacitors (Adv. Energy Mater. 24/2018), Advanced Energy Materials 8(24) (2018) 1870108.

[32] Y. Yong, X. Lou, S. Li, C. Yang, X. Yin, Direct simulation of the influence of the pore structure on the diffusion process in porous media, Computers & Mathematics with Applications 67(2) (2014) 412-423.

Chapter 4. Correlation between the Space Characteristics of CNF and the Electrochemical Performance

4.1 Introduction

The demand for high capacity energy storage systems, such as enormous electric storage stations and electrical vehicles, has increased dramatically [1-7]. Since the early 1990s, graphite has become the most common anode material by replacing lithium metal because of its safe energy storage mechanism and economical merits, such as natural abundance and environmental benignity [8-11]. On the other hand, the energy storage mechanism of graphite limits the theoretical capacity because Li ions are only intercalated into the limited space in-between the basal planes [10, 12, 13]. Low temperature carbon (LTC) prepared at low temperatures (<1200 ^{o}C) has attracted considerable research attention because LTC not only intercalates Li ions between graphitic layers but also stores Li ions in the micropores on the graphitic layer as Li clusters or Li molecules, increasing the reversible capacity compared to graphite [14, 15]. Among the various precursors for LTC, PAN-derived LTC has been studied widely because of its high carbon content and that it can also be transformed to *N*-doped carbon for more Li ion storage [16-23]. Nevertheless, low temperature synthesis results in a low degree of graphitization and poor electrical conductivity, which leads to large charge transfer resistance and low rate capability of the anode material.[21, 24-27] In addition, some micropores in LTC were initially clogged or destroyed during the cycles, which adversely

affects the ion accessibility and cycling stability.[14] Because the anode material requires a high reversible capacity, good rate capability, and cycling stability, the currently developed LTC was unsuitable as a superior anode material. Therefore, it is essential to enhance both the electronic conductivity and ion-accessibility while stabilizing the structure in LTC for achieving high performance anode materials. Herein, we denote the electrochemical redox sites, where ions and electrons meet as a 'triple junction' suggesting that the origin of the high electrochemical performance is the perfect harmony of ion, electron, and redox sites together. The ideal electrode structure for a high performance anode is one with a maximized triple junction. In the view of a triple junction, there have been many efforts to use carbon nanotubes (CNTs) in LTCs because of the physical and chemical merits of CNTs that can achieve the following: facilitate electron transfer due to its superior electrical conductivity of 10^6-10^7 S m^{-1},[28, 29] form facile ion channels as redox sites in-between the CNTs owing to its 1D structure,[30] and withstand large volume changes during cycling, which originated from the increased lithium storage at the newly adopted redox sites due to the high mechanical strength of CNTs.[31-33] CNT/PAN-derived low temperature carbon nanofiber (LTCNF) hybrid anode,[34] SnO_x-embedded CNT/PAN-derived LTCNF anode,[35] and Si-loaded CNT/PAN-derived LTCNF[36] anode are such cases.

Despite the recent advances of CNT-based electrodes, the critical issues limiting commercialization are still unresolved. The most difficult part to utilize CNTs is controlling the state of CNTs in LTC due to the aggregation of CNTs resulted in the increased electrical resistance and undesirable structure.[37, 38] Furthermore, aggregated CNTs would lower the surface coverage of CNTs within the LTC,[39] interrupting the electrons on CNTs to meet ions in the LTC and consequently decreasing the accessible redox sites.[40] Therefore, it is essential

to control the aggregation of CNTs in CNT-LTC-based anode materials to fully utilize the merits of CNTs and guarantee the abundant redox sites to materialize an optimal electrode structure by maximizing the triple junctions in a CNT-LTC-based electrode.

Herein, 1D partially graphitized LTC with uniaxially packed CNTs was prepared by a facile method using a co-polymer system for dealing with the critical issues. The uniaxially aligned CNTs in 1D LTC acts as a) stable structural scaffold supporting the adequate porous structure that enhances the ion accessibility, b) electron transfer path, and c) effective triple junctions where ion and electron meet at effective redox sites, for example, change in nitrogen bonding configuration by increasing beneficial N-5 and N-6 while reducing harmful N-Q. These synergetic roles between packed uniaxially CNTs and LTC are elucidated in the following discussions: 1) role of the slow-envelopment phenomenon to design an ideal structure, 2) role of activation to realize the hierarchical pore network, and 3) role of CNTs in increasing the electrical properties.

*** Part of result and discussion of Chapter 4 was published in**

ACS Nano 2018, 12, 11106−11119

4.2 Results and discussion

4.2.1 Effects of hierarchical space modification on electrochemically active sites maximization

Before discussing the effective methods to control the CNT aggregation issue with single nozzle electrospinning using CNT orientation-controlling polymer (PAN) and template polymer (PMMA), the adequate preparation of dope solution is critical for developing highly dispersed CNTs by single nozzle electrospinning. An acid-treatment was previously believed to be essential to increase the degree of CNT dispersion and allow the fabrication of CNT strands into a 1D morphology.[41-43] On the other hand, this method results in CNTs with poor conductivity and more importantly cannot fully suppress the aggregation of CNTs unless it is harshly acid-treated.[42-45] Therefore, polymer wrapping methods have been used to highly disperse pristine CNTs without impeding the electrical conductivity of CNTs.[46, 47] Among the wide range of polymers, PAN wrapping can turned easily to low temperature carbon during thermal treatment,[48] enhancing the degree of CNT dispersion.[49, 50] Nevertheless, when PAN is used solely to produce a dope solution for electrospinning, only small amounts of CNTs are confined to the inner part of the electrospun fiber while an excessive amount of PAN accumulates on the outer surface, as shown in Fig. 4.3f. Williams[51] and Kim[52] suggested the fundamental reason for this unideal structure in that when phase migration occurs in the electrospinning step, a high-viscosity phase envelopes the low-viscosity phase according to a ‘slow-envelopment phenomenon’. Therefore, in this study, a co-polymer system with PAN and PMMA was adopted to minimize the concentration of PAN. PMMA is immiscible with PAN so it can act as a shell template to form a core-shell structure by a slow-envelope phenomenon at certain concentration ratios, and can be clearly removed after

pyrolysis. In Fig. 4.2, the concentration ratio between PAN and PMMA was varied and their corresponding morphologies were analyzed to determine the ideal solution concentration for the slow-envelopment phenomenon. Fig. 4.1 presents the overall process of preparing the 1D partially graphitized LTC with uniaxially packed CNTs. The sample names are denoted as below.

	Activation	**Activation temperature**	**Template polymer**	**CNT**
CNTCNF	X	-	X	O
CNF	X	-	O	X
MC CNTCNF	X	-	O	O
CNTPNF	O	750 ºC	X	O
PNF	O	750 ºC	O	X
MC CNTPNF	O	750 ºC	O	O
MC CNTPNF-650	O	650 ºC	O	O
MC CNTPNF-850	O	850 ºC	O	O

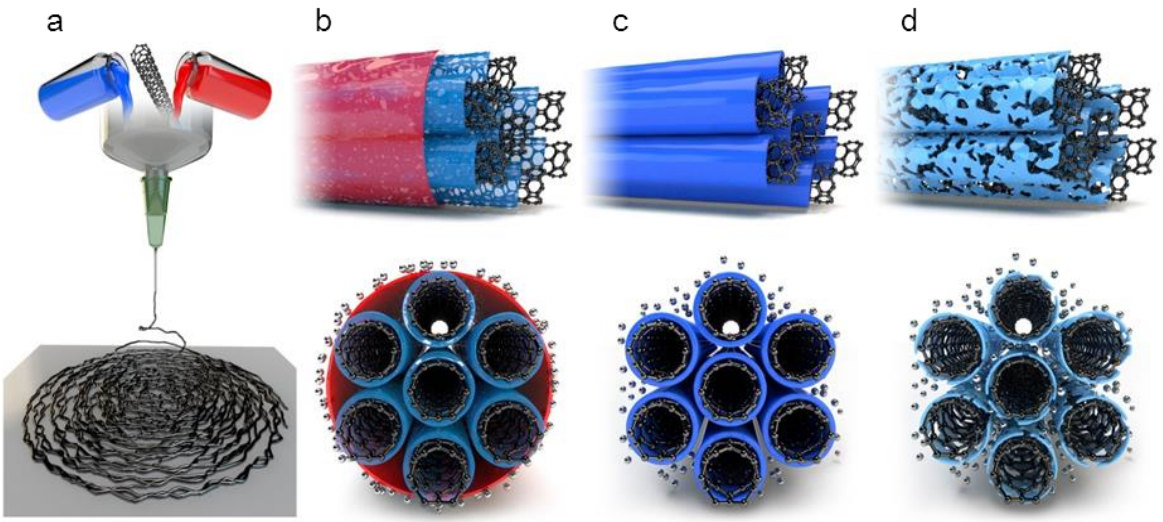

Figure 4.1 Schematic illustration of the changes in the morphological and chemical properties of the prepared samples in (a,b) co-polymer electrospinning, (c) gluing CNTs and carbonization, and (d) developing a connected pore network by KOH activation.

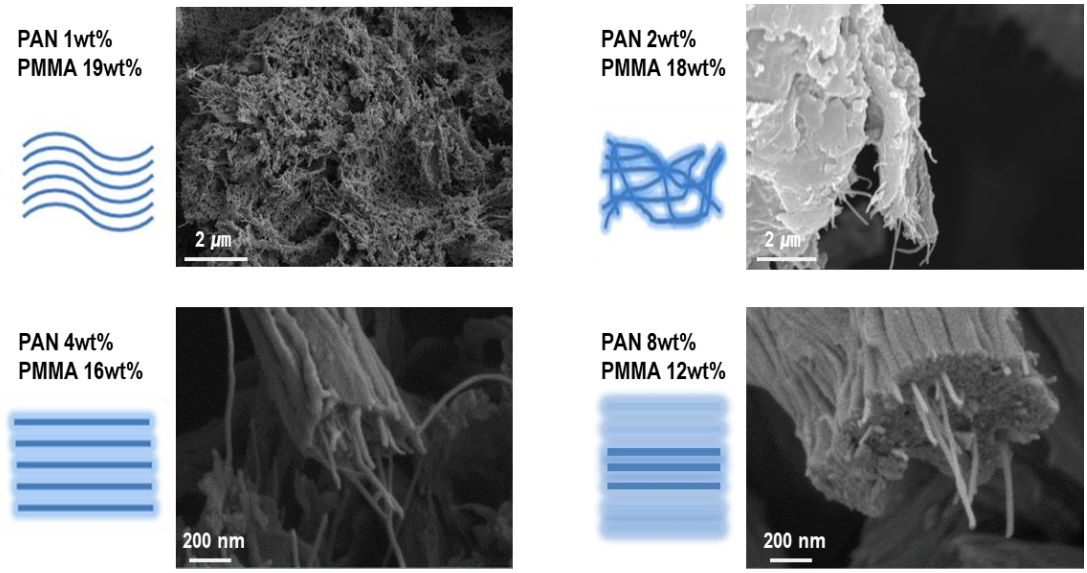

Figure 4.2 Varying concentration ratio between PAN and PMMA and their corresponding morphologies.

‘PNC’ denotes ‘porous *N*-doped carbon’, which is acquired from heat treatment of PAN. The process of preparing MC CNTPNF consists of three steps: electrospinning, heat treatment, and activation. Suffix number, such as ‘-750’, denotes the activation temperature. Nanofibers, in which the PMMA envelopes the PAN-wrapped CNTs, can be obtained by electrospinning (Fig. 4.1(a,b)). In the following carbonization process, as illustrated in Fig. 4.1c, the template polymer (PMMA) is decomposed and removed while PAN is changed to partially graphitized *N*-doped porous LTC, maintaining its morphological integrity. Finally, the 1D hierarchically porous material composed of densely packed CNTs (core) and abundant redox sites (shell) of PNC is prepared during the KOH activation process. This guarantees rapid ion/electron transfer with reversible lithium storage sites by maximizing the triple junction, where ion-electron-redox site meet, even though there is little sacrifice of the N contents during the connected micro pore development.

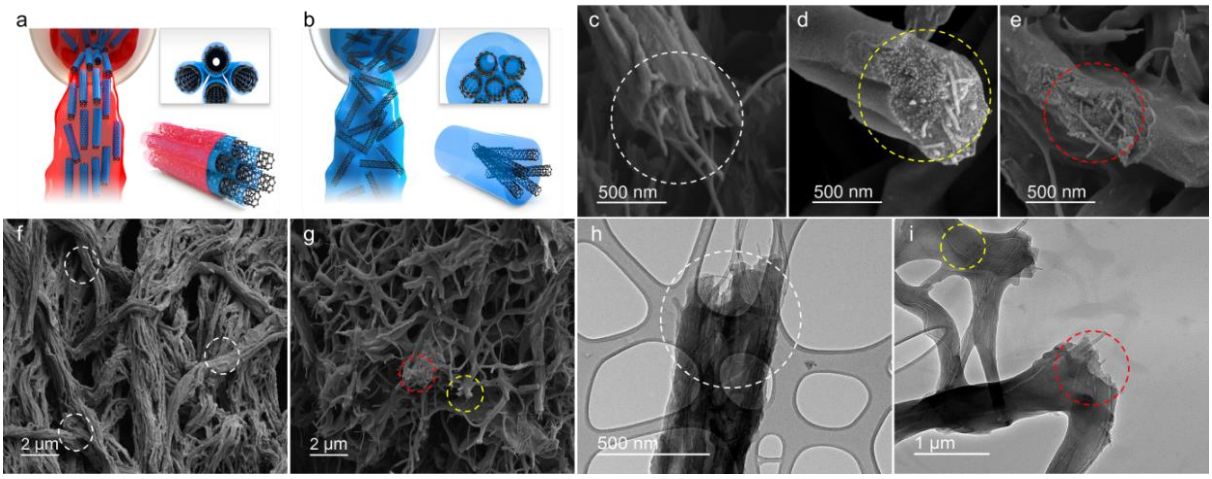

Figure 4.3 Schematic illustration of electrospinning (a) MC CNTCNF and (b) CNTCNF; FE-SEM images of (c, f) MC CNTCNF and (d, e, g) CNTCNF in (c, d, e) high-resolution and (f, g) low-resolution respectively; and corresponding TEM images of (h) MC CNTCNF and (i) CNTCNF; the white circles in (c), (f), (h) indicate uniaxially packed CNTs in a thin PNC layer; the yellow circles in (d), (g), (i) indicate the aggregation of CNTs with very thick layers of PNC; and the red circles in (e), (g), (i) indicate a fragmentized short 1D structure with CNTs out of the nanofiber.

As shown in the FE-SEM and TEM images, the prepared samples showed obvious differences in the orientation and morphological structure of the CNTs depending on the existence of a template polymer. In Fig. 4.3a-i, both MC CNTCNF and CNTCNF exhibited a polymer-wrapped surface and a 1D rod-like morphology. In MC CNTCNF, however, an individual strand of electrospun fiber collectively formed a long 1D morphology with uniaxially packed CNTs under a thin PNC layer (white circle), while CNTCNF showed a fragmentized short 1D with CNTs out of fiber (red circle) and/or the aggregation of CNTs with very thick layers of PNC (yellow circle), which is an non-ideal morphology. Compared to the very smooth and fine surface of CNTCNF, MC CNTCNF has a thin, rough surface with pores, maintaining an ideal 1D morphology. The smoother and finer surface might be explained by the relatively small amount of CNTs confined in inner part and the excessive thick PAN layer located at the surface.

Fig. 4.4a shows that a high viscous phase, whose excessive PAN did not wrap the CNTs, is located at the outer surface and low viscous phase, which is PAN-wrapped CNTs confined to the inner part. As the concentration of PAN increases, large amounts of PAN are attached to the surface of the CNTs and the thickness of wrapping PAN becomes thicker,[50] resulting in an unfavorable morphology. The fragmentized electrospun fibers are also unfavorable for an electrode material due to the disconnected electron pathway from the collapsed 1D morphology. The thin, rough, and porous surface of MC CNTCNF might be due to the minimum concentration of polymer to CNT and decomposition of the template polymer. In MC CNTCNF, orientation-controlling polymer (PAN) is dissolved at the minimum concentration, which is inadequate for fabricating 1D nanofibers during electrospinning, but adequate for wrapping the individual CNTs and producing thin PNC. Template polymer (PMMA), which was used to fulfill the critical minimum concentration for electrospinning and for a stable template shell, was removed after pyrolysis. Subsequent pores originating from void space between each thin PNC on the individual CNTs and during decomposition of the template polymer enabled rapid ion accessibility.

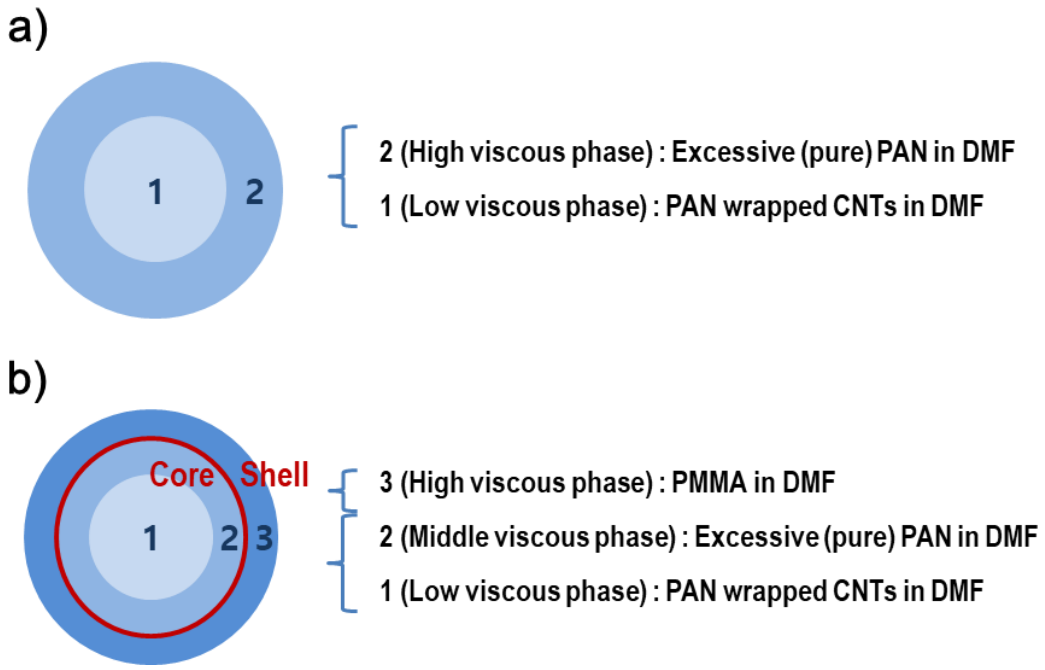

Figure 4.4 Schematic illustration of the phases in cross section of electrospinning nanofiber.

This was confirmed further by the characterized specific surface area and pore structure of the samples by N_2 adsorption/desorption characterization. An analysis of the BET specific surface area (SSA) and pore volume data (Table 5.1) revealed MC CNTCNF (74 m^2 g^{-1}) to have a 10 times larger surface area than CNTCNF (7 m^2 g^{-1}) and meso (2~50nm)/macro (>50nm) pores. This result was verified by the pore size distribution based on Original Density Functional Theory (Fig. 4.5a). Density functional theory is developed by Seaton and widely used method for predicting adsorption/desorption isotherms in pores of different geometries over a wide range of pore sizes, and for calculating pore size distributions.[53-55] In addition, using N_2 adsorption isotherm data (Fig. 4.5b), the rapid ion accessible structure, whose pore network has various pore sizes, was verified in the MC CNTCNF sample, but not in CNTCNF. This structural difference was consistent with the TEM and SEM images in Fig. 4.3c-i. This 1D porous structure in MC CNTCNF is expected to facilitate rapid electrolyte transfer and offer favorable pathways for ion penetration and transport.

Table 4.1 Specific surface area and pore volume of CNTCNF and MC CNTCNF

	Specific surface area ($m^2 g^{-1}$)	Total pore volume ($cm^3 g^{-1}$)	V_{macro} ($cm^3 g^{-1}$)	V_{meso} ($cm^3 g^{-1}$)	V_{micro} ($cm^3 g^{-1}$)
CNTCNF	7	0.006	0.004	0.002	~0
MC CNTCNF	74	0.174	0.123	0.040	0.007

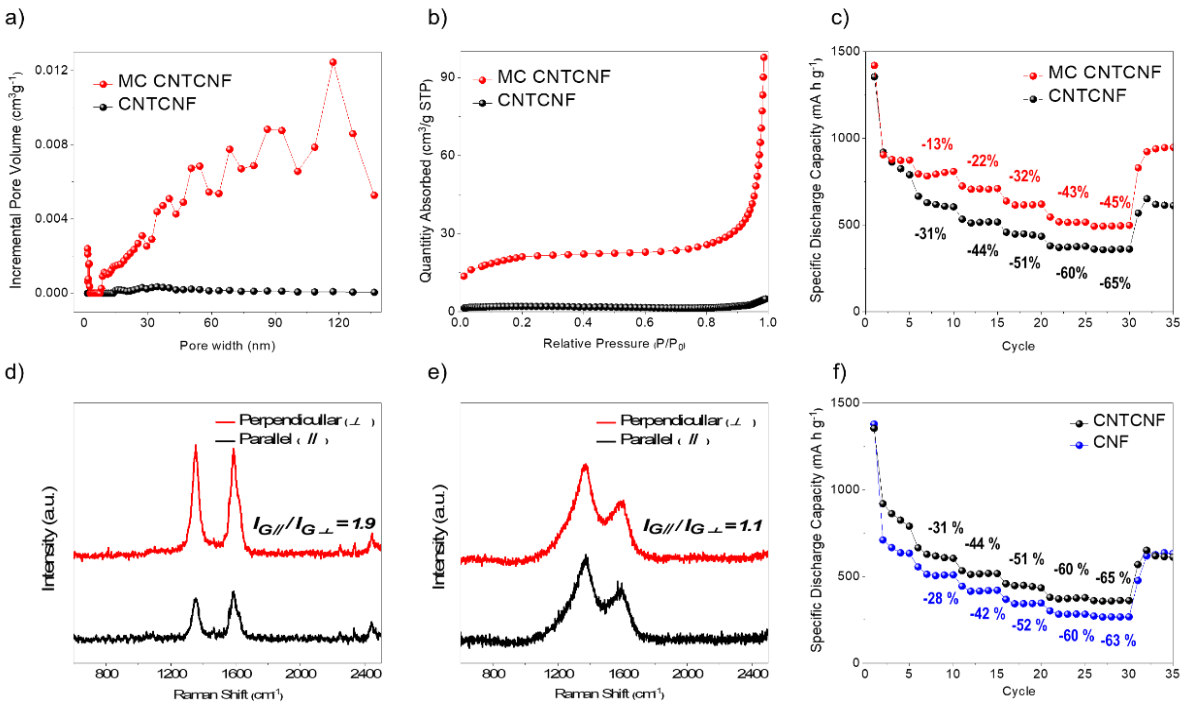

Figure 4.5 (a) Incremental pore volume *versus* pore width; (b) N_2 adsorption isotherm; (c) electrochemical test results of MC CNTCNF and CNTCNF at the various charge/discharge current densities (50, 100, 200, 250, 500, 1,000, and 50 mA g^{-1}.)(-xx% indicates the capacity drop of each current density from 50 mA h g^{-1}); polarized Raman spectra of (d) MC CNTCNF and (e) CNTCNF; (f) electrochemical test results of CNTCNF and CNF at various charge/discharge current densities

The chemical properties of MC CNTCNF and CNTCNF were examined further by element analysis. As shown in Fig. 4.6, the N contents of MC CNTCNF and CNTCNF were measured as 11.5 at. % and 19.2 at %, respectively. The higher N contents of CNTCNF can be explained by the higher PAN to CNTs ratio in the dope solution. The N bonding configurations of the samples were investigated based on the deconvoluted XPS spectra in Fig. 4.7a and summarized in Fig. 4.7b. The spectra showed two main peaks for pyridinic N (N-6, 398.4±0.2) and pyrrolic or pyridonic N (N-5, 399.8±0.2).[48] Both N-6 and N-5 are beneficial to lithium ion storage in anode materials.[56-58] The electrochemical test results showed that MC CNTCNF had better performance in varying the charge/discharge current densities from 50 mA g^{-1} to 1000 mA g^{-1} despite the lower N contents compared to CNTCNF (Fig. 4.5c). The MC CNTCNF electrode delivered an average 135.0 mA h g^{-1} more capacity at 1000 mA g^{-1} and 304.3 mA h g^{-1} more at returning 50 mA g^{-1}. The irreversible capacity observed in both samples at the 1st cycle is a common phenomenon in carbon-based electrodes due to the formation of a solid electrolyte interface layer.[59] Despite the higher N contents of CNTCNF, the superior electrochemical performance of MC CNTCNF might be due to the unveiled redox active sites of N-6 and N-5 to the electrolytes on the rapid ion-accessible porous surface of MC CNTCNF, which is supported indirectly by the measured specific surface area and pore volume (Table 5.1, Fig. 4.5a-b). In addition, it can also have originated from the ideal structure of MC CNTCNF, as supported visually in Fig. 4.3a-i. In this case, the smooth surface of CNTCNF has no porous structure for rapid ion accessibility, which is unfavorable for the electrode materials in that the thick PNC layers on the CNTs act as a barrier and impede the penetration and diffusion of the electrolyte.

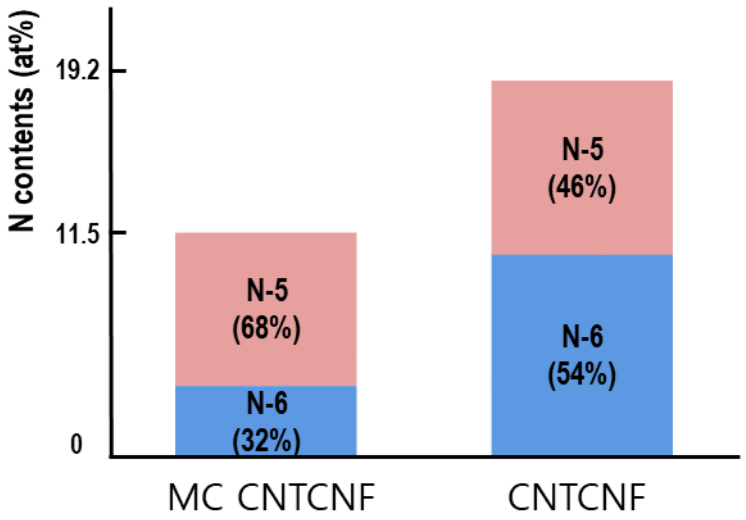

Figure 4.6 N contents and corresponding bonding configuration of each sample.

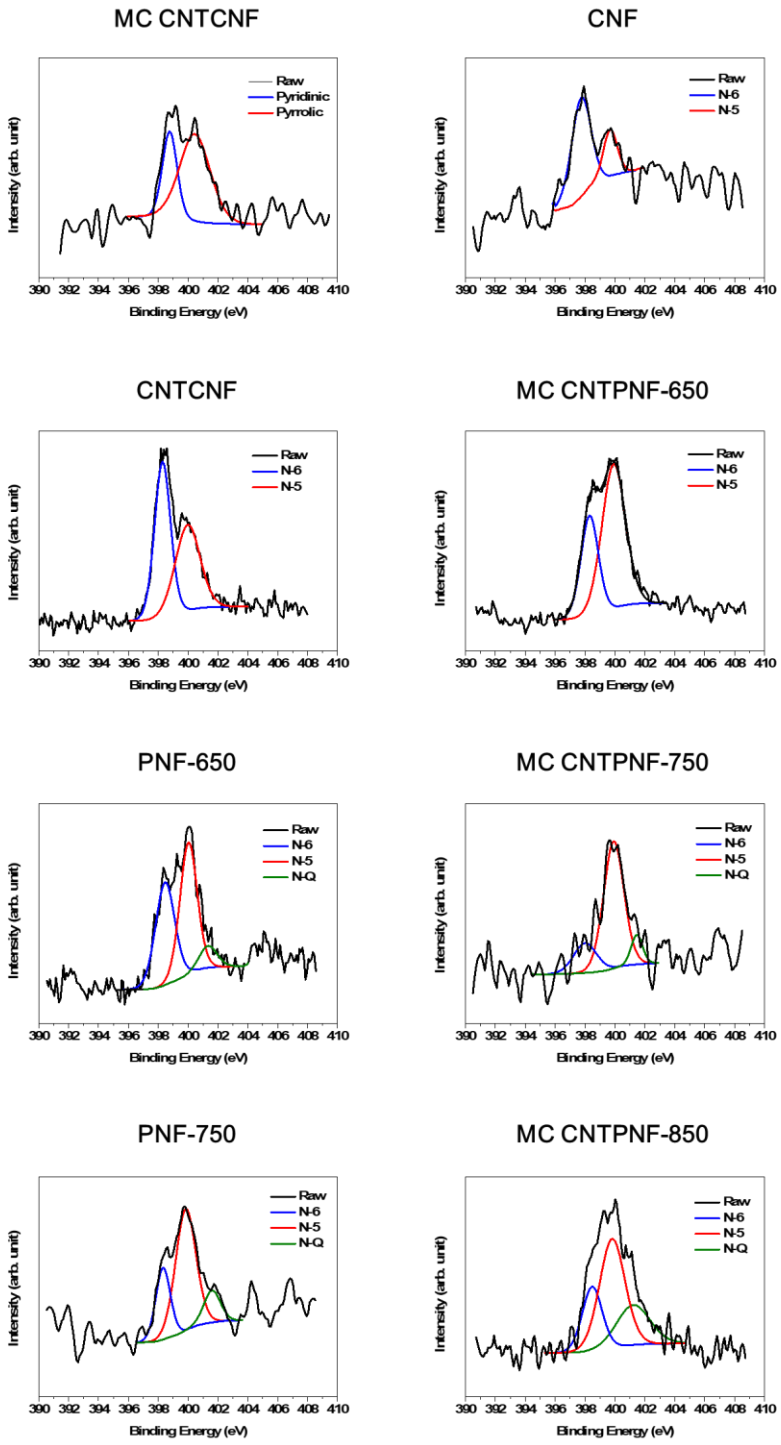

Figure 4.7 The N bonding configurations of the samples investigated based on the deconvoluted XPS spectra

Polarized Raman spectroscopy was performed to further support the structural characteristics, as shown in Fig. 4.5d and 5e. The ratio of the intensity of the G-band in the parallel configuration to the perpendicular configuration ($I_{G//}$ / $I_{G\perp}$) of sample MC CNTCNF was 1.9, which much higher than 1.1 in CNTCNF, showing that the CNTs in MC CNTCNF are aligned uniaxially. Only when the CNTs are uniaxially and densely packed in 1D morphology can the CNTs act as structural scaffold within material and prevent the material from collapsing both in material preparation step and electrochemical reaction step (Fig. 4.3a-i). In Fig. 4.8a-d, the role of CNTs as a structural scaffold was confirmed clearly by FE-SEM of the MC CNTCNF electrodes before and after cycling. The ideal 1D morphology with aligned CNTs (Fig. 4.8a) was well-preserved during cycling under both low C-rate (Fig. 4.9a) and high C-rate test conditions (Fig. 4.8b). On the other hand, the CNF electrodes (Fig. 4.8c) collapsed under both the low C-rate (Fig. 4.9b) and high C-rate test conditions (Fig. 4.8d), indicating that the uniaxially packed CNTs inside PNC act as a structural scaffold. Finally, the importance of an ideal CNT morphology and structural integrity was verified by the electrochemical test results.

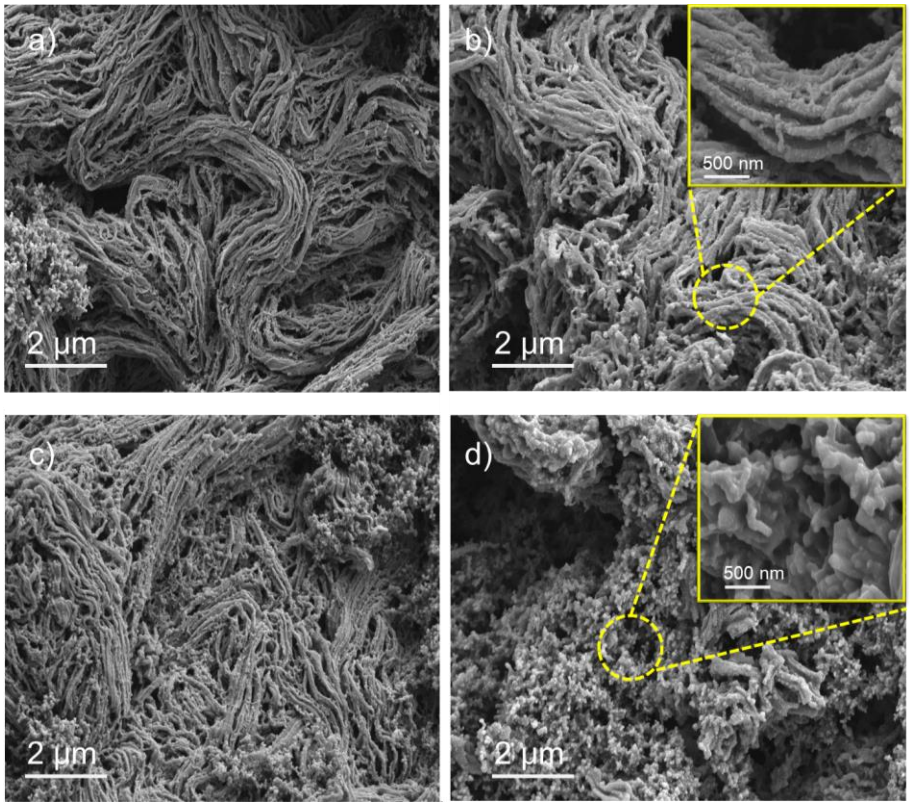

Figure 4.8 FE-SEM images of (a) MC CNTCNF electrode before cycle (b) MC CNTCNF electrode after cycles; (c) CNF electrode before cycle (d) CNF electrode after cycles

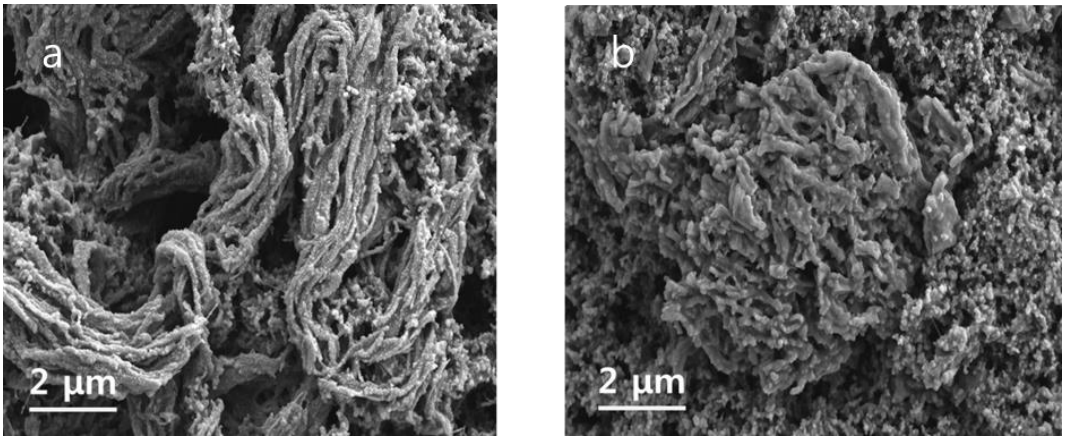

Figure 4.9 FE-SEM images of the (a) MC CNTCNF and (b) CNF electrodes after cycles under low C-rate test conditions.

As shown in Fig. 4.5c, at a current density of 50 mA h g^{-1} after several current densities, the capacity of the CNTCNFs was not recovered from the first 50 mA h g^{-1}. In addition, despite the presence of CNT in CNTCNF, the rate capability was not improved compared to MC CNTCNF. Interestingly, the rate capability of CNTCNFs was worse than that of CNF, which has no CNTs (Fig. 4.5f). The poor performance of CNTCNF despite the presence of CNTs clearly supported the importance of a pore network in electrode materials. The thick PNC layer of the CNTCNFs which lack a pore network, negated the enhanced electrical conductivity of the CNTs within the active material and the ion accessibility, hindering the development of an efficient triple junction. It is also indirectly supported by the voltage profile of CNTCNF and MC CNTCNF (Fig. 4.10) and cyclic voltammogram (CV) of CNF, CNTCNF, and MC CNTCNF (Fig. 4.11). Fig. 4. 10 and 11 demonstrated that the lower irreversible capacity and enlarged redox peaks of MC CNTCNF due to the template polymer and well-aligned CNTs.[60] Although the 1D porous structure in MC CNTCNF was proven to be effective in facilitating electrolyte penetration and storage, the low value of SSA and the pore volume provide the possibility to increase the electrochemical performance further by developing micro pores for Li storage and connecting the hierarchical pore network for rapid ion channels.

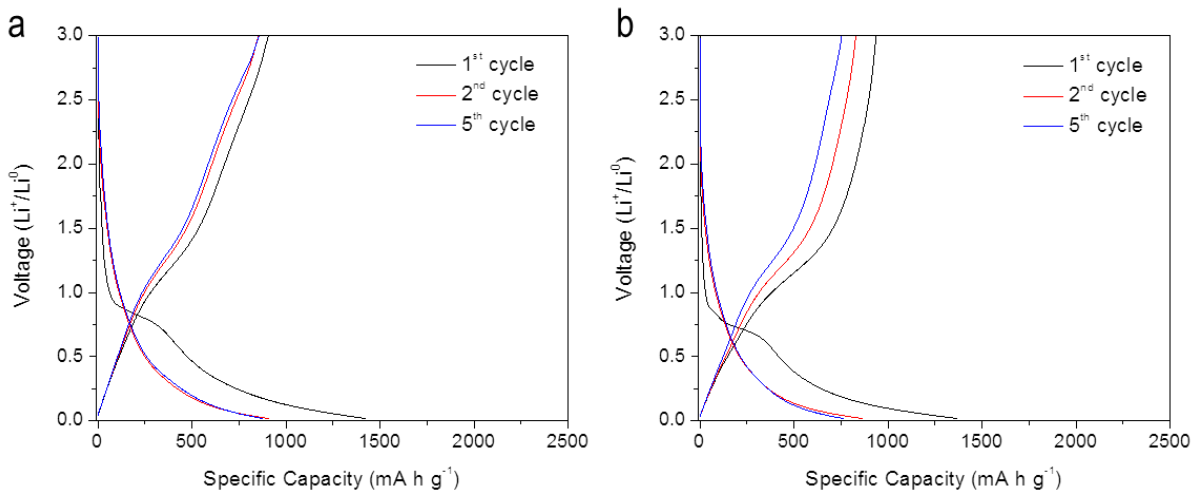

Figure 4.10 Voltage profile of (a) MC CNTCNF and (b) CNTCNF

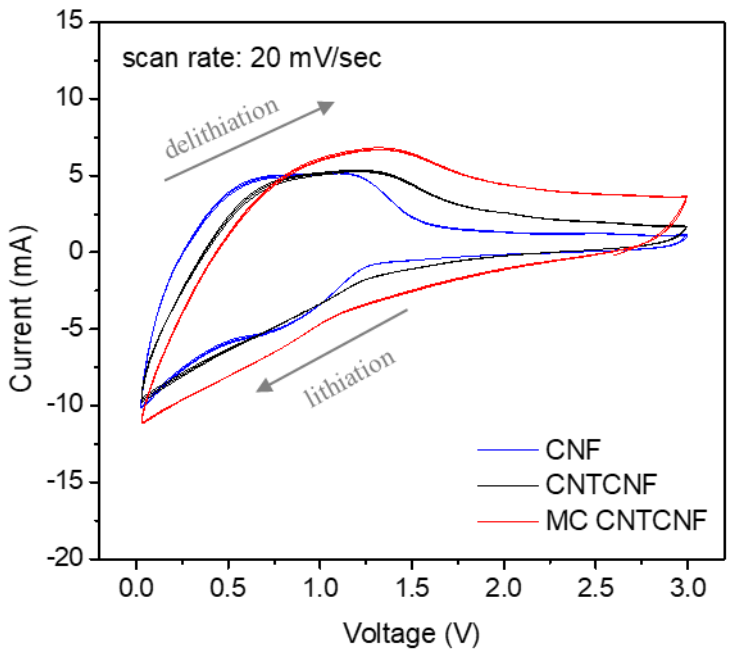

Figure 4. 11 Cyclic voltammograms (CVs) of CNF, CNTCNF, and MC CNTCNF

As shown in Fig. 4.1 and 3, the non-porous, thick surface and low specific surface area in CNTCNF might impede the access of lithium ions to the inner redox sites. Despite the 10 fold increase in the SSA compared to CNTCNF, the insufficient value of MC CNTCNF (74 m^2 g^{-1}) suggests that the slightly rough surface of carbonized PNC@CNT might not be enough for the electrolyte to penetrate and diffuse easily to the CNT. This would make it difficult to achieve the synergistic effect of the CNT core, as supported indirectly by the electrochemical test results at a high current density of 1000 mA g^{-1}. The insufficient pores, veiled redox sites, and CNTs can be developed and unveiled easily by KOH activation.[1, 61] The pore developing effect was examined by activating MC CNTCNF and CNTCNF (denoted as MC CNTPNF-activation temperature and CNTPNF-activation temperature). In addition, activation was carried out at varying temperatures from 650 to 850°C to examine the effect of the activation temperature on developing pores and the change in PNC and determine the optimal activation temperature. As shown in Fig. 4.12a-f, the FE-SEM and TEM images of MC CNTPNF and CNTPNF were different from each other in that CNTPNF exhibited a collapsed morphology with wrecked ends and protruding CNTs, whereas MC CNTPNF maintained its original 1D morphology with individual PNF wrapped CNTs. Fig. 4.14d shows X-ray diffractograms of PNF and MC CNTPNF. The peaks at the 2θ angle of 23.5° and 42° arise from (002) and (10) reflections of the partially carbonized PNF sample, and the peaks at 25.3° and 42° from the carbonized shell and the well-aligned CNTs in the core of MC CNTPNF. This implies that the carbonization was facilitated by the presence of CNTs in the fibers, which contributes to the higher crystallinity of the sample.[62-64]

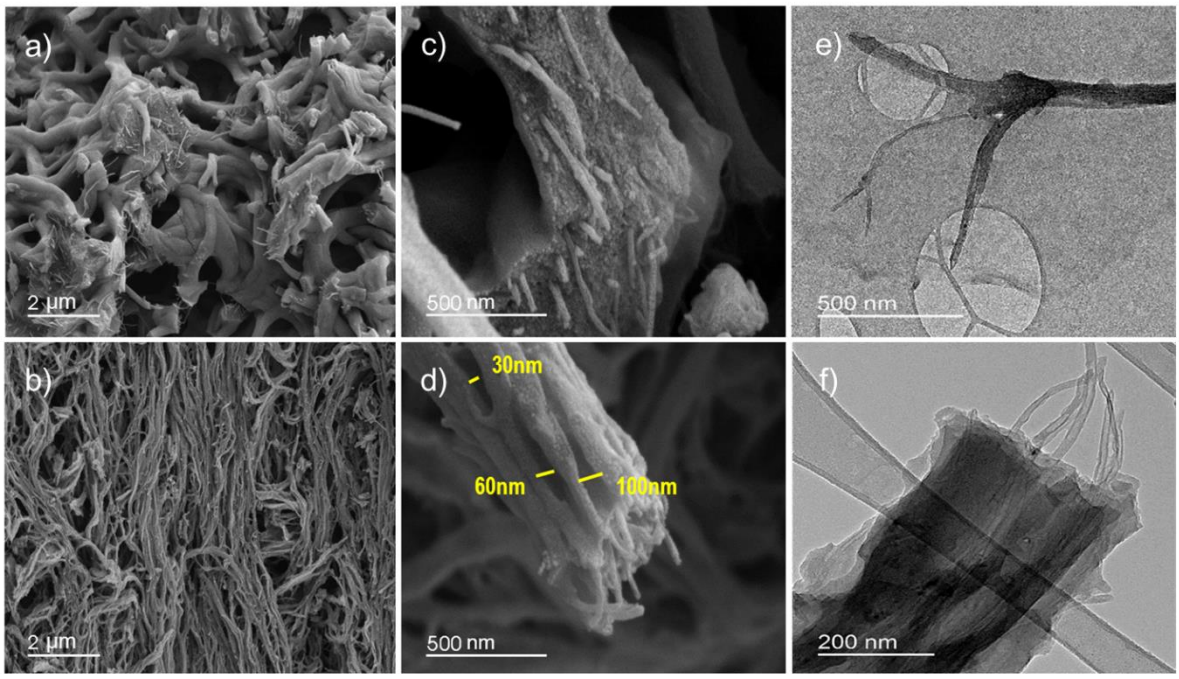

Figure 4.12 FE-SEM images of (a), (c) CNTPNF and (b), (d) MC CNTPNF in the low and the high resolution respectively; and corresponding TEM images of (e) CNTPNF and (f) MC CNTPNF

The surface of MC CNTPNF was slightly roughened due to the activation process developing micro pores resulting from carbon decomposition and gas evolution. The development micropores in both MC CNTPNF and CNTPNF was confirmed by the pore size distribution based on Original Density Functional Theory (Fig. 4.13a), the cryogenic N_2 isotherm, and increased SSA (Fig. 4.13c). The lack of a suitable porous structure and the extensive evolution of micropores in CNTPNF resulted in a vanishing hierarchical pore network with an extremely high SSA of 2485 $m^2 g^{-1}$. MC CNTPNF, however, maintained its hierarchical pore structure with a slightly lower SSA of 1217 $m^2 g^{-1}$. This difference might come from the structural integrity of the activation precursors (MC CNTCNF and CNTCNF). The structural integrity of MC CNTCNF might have originated from the optimal ratio between the CNTs and polymers, leading to strong resistance to deformation, which is analogous to the case of reinforced concrete. On the other hand, the randomly oriented CNTs in CNTCNF were crumbled during heat treatment due to the insufficient ability to withstand the activation process. This result supports indirectly the role of a stable structural scaffold of uniaxially aligned CNTs. During KOH activation, the clogged pores and veiled redox sites embedded in the inner part of 1D PNC was unveiled, developing a fast-ion accessible hierarchical pore network (Fig. 4.13a-c).

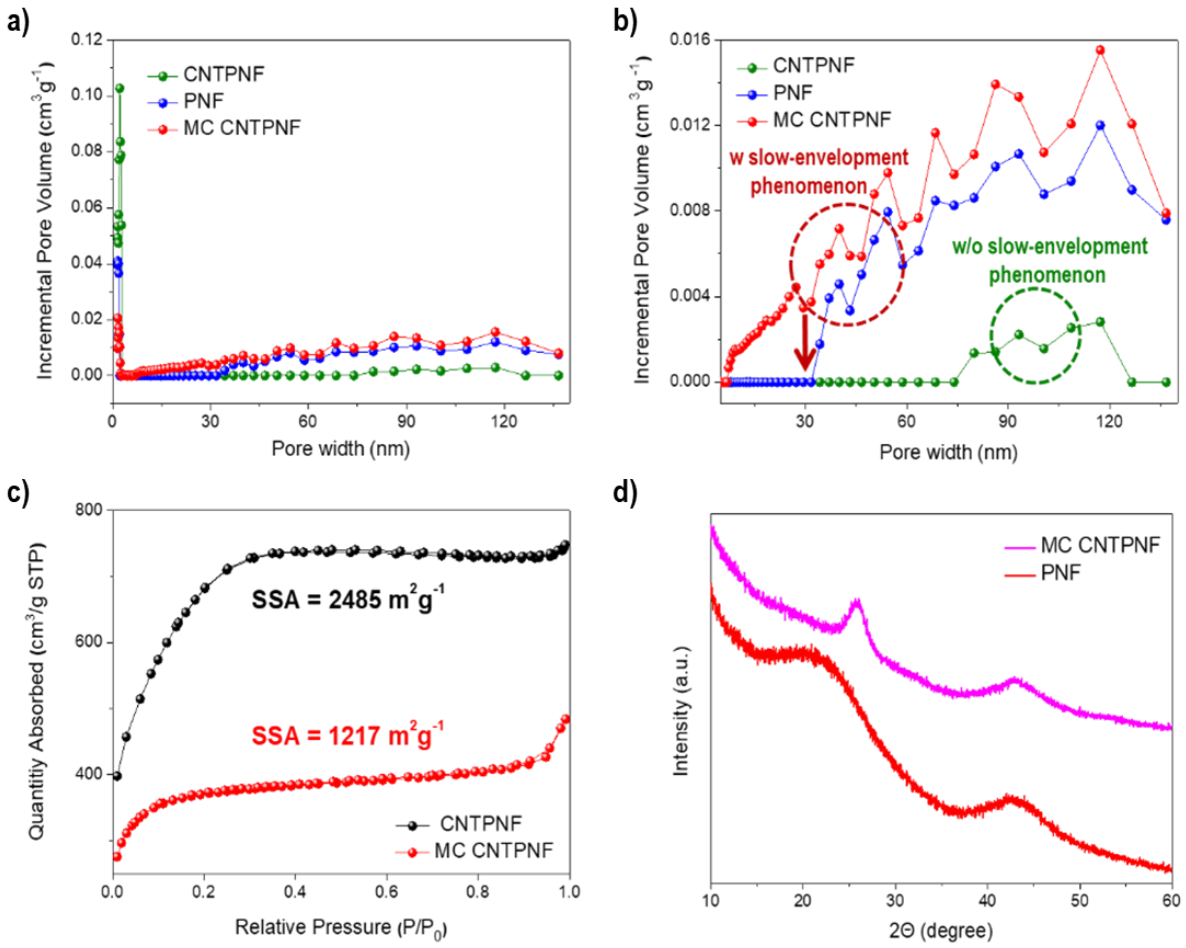

Figure 4.13 (a) Incremental pore volume *versus* pore width; (b) Incremental pore volume *versus* pore width above 5nm; (c) N_2 isotherm of the prepared samples with the SSA of the activated sample; (d) X-ray diffractogram of PNF and MC CNTPNF samples

In the pore size distribution based on Original Density Functional Theory (Fig. 4.13b), MC CNTPNF and PNF, which had a template polymer, have pores > 30nm in size. In contrast, CNTPNF, which had no template polymer, does not have pores > 30nm in size, and this difference goes well with the role of the template polymer in that it develops a reasonable porous structure, as mentioned in part 1 of this paper. Consequently, this pore structure, which has a pore size above approximately 30nm, is expected to produce a rapid ion-accessible structure that is verified by calculations of the Li ion diffusion coefficient (Fig. 4.14). In Fig. 4.15a, the Li ion diffusion coefficient of each sample (CNTPNF (8.78E-10 cm^2 s^{-1}), PNF (1.21E-09 cm^2 s^{-1}), and MC CNTPNF (2.43E-09 cm^2 s^{-1})) showed a reasonable correlation with each ratio of the pore volume, whose pore size was above 30nm, which is in contrast to the pore volume, whose pore size below 30nm. Considering that most previous studies regarded mesopores and macropores as pores that facilitate Li ion diffusion, this correlation is quite interesting in that this correlation, whose diffusion facilitating pore size criterion of 30nm (Fig. 4.15a), is more reliable than the counterpart, whose criterion is on the IUPAC pore classification (Fig. 4.15b).

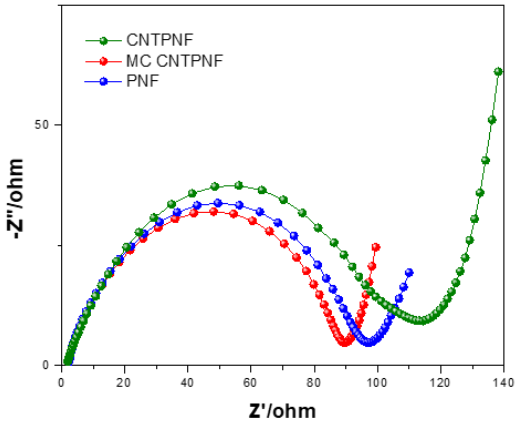

$$D_{Li^+} = \frac{1}{2}\left(\frac{RT}{AF^2C\sigma_\omega}\right)^2$$

	Slope (σ_w)	D_{Li+}
MC CNTPNF	3.38	2.43E-09
PNF	4.79	1.21E-09
CNTPNF	5.62	8.78E-10

Figure 4.14 Electrochemical impedance spectroscopy of each sample for Li ion diffusion coefficient calculation.

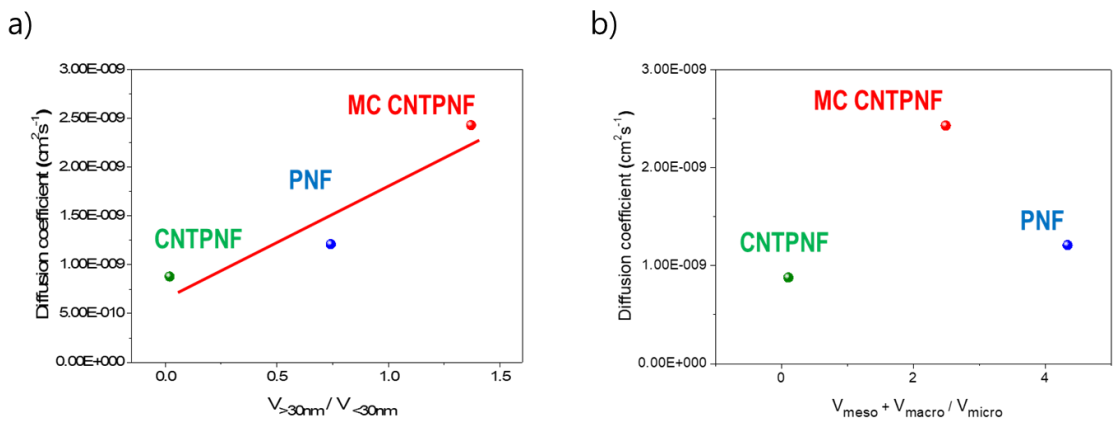

Figure 4.15 (a) Correlation between the diffusion coefficient and parameter, which stands for ratio of the pore volume, whose pore size was above 30nm, which is in contrast to the pore v olume, whose pore size below 30nm. The diffusion coefficient of Li ions was determined by electrochemical impedance spectroscopy (Figure 4. 14); (b) Correlation between diffusion co efficient and parameter which stands for ratio of the meso+macro pore volume, which is in co ntrast to the micropore volume.

Subsequently, this efficient pore network has a positive impact on its electrochemical performance at different charge/discharge current densities from 50 to 1000 mA g^{-1}. This phenomenon is supported by the approximately 16-fold increase in SSA from 74 to 1217 $m^2 g^{-1}$ in MC CNTPNF (Table 5.2) and the strong 107, 98, and 73% increase in reversible capacity after KOH activation at 50, 200, and 1000 mA h g^{-1}, respectively (Fig. 4.16b). CNTCNF, which has no template polymer, showed the same phenomenon in that the SSA increased from 7 to 2485 $m^2 g^{-1}$. Interestingly, however, although the increased SSA of CNTCNFs (approximately 355 fold) was much higher than that of MC CNTCNF (approximately 16 fold), the enhancement of the reversible capacity was much lower (by 47, 57, and 47 % at 50, 200, and 1000 mA h g^{-1}, respectively) (Fig. 4.18). This difference suggests that the presence of a pore network, whose pore size is above approximately 30nm, is an important factor in developing 'effective' micropores within a hierarchical pore network to actually store Li ions. Therefore, KOH activation only could develop unusable and inaccessible micropores if the ideal structure had not been formed previously (Fig. 4.16).

Table 4.2 SSA and pore volume for each sample

	Specific surface area ($m^2 g^{-1}$)	V_{total} ($cm^3 g^{-1}$)	V_{macro} ($cm^3 g^{-1}$)	V_{meso} ($cm^3 g^{-1}$)	V_{micro} ($cm^3 g^{-1}$)
CNTCNF	7	0.006	0.004	0.002	~0
CNTPNF	2485	0.555	0.017	0.037	0.501
MC CNTCNF	74	0.174	0.123	0.040	0.007
MC CNTPNF	1217	0.311	0.141	0.081	0.089

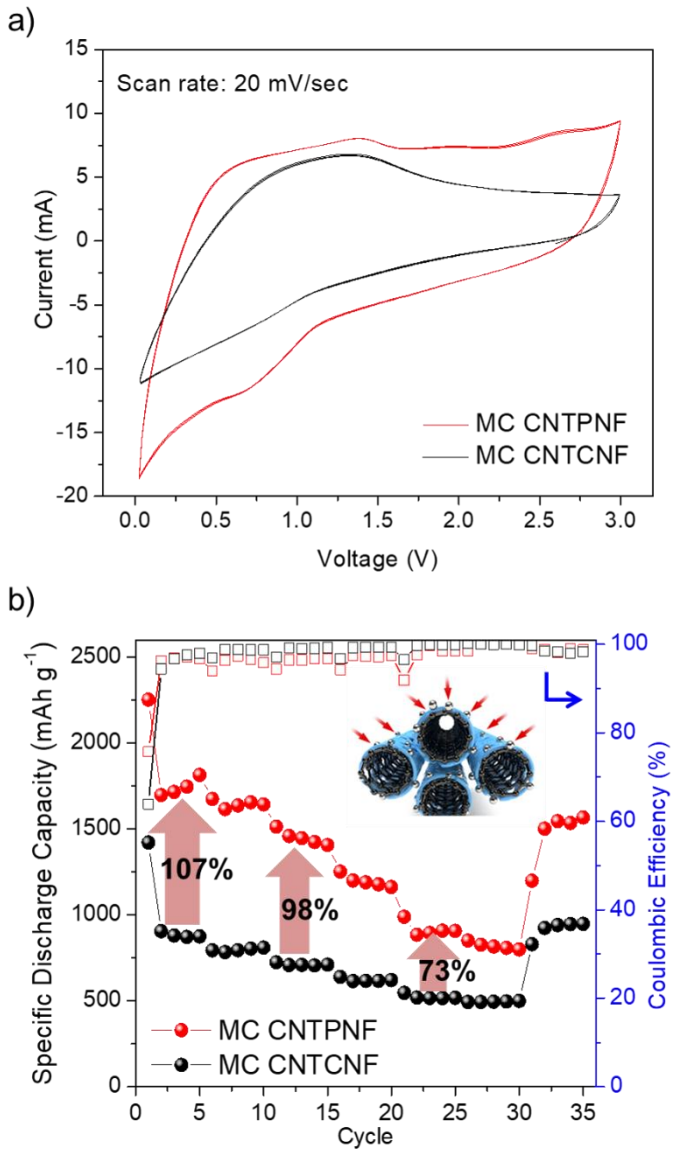

Figure 4.16 (a) Cyclic voltammogram (CV) of MC CNTPNF and MC CNTCNF; (b) Electrochemical test results at varying current densities (50, 100, 200, 250, 500, 1,000, and 50 mA g^{-1}, respectively.) and capacity enhancement (xx%) by KOH activation for MC CNTCNF, which had template polymer; Schematic illustration of (inset in (b)) MC CNTPNF;

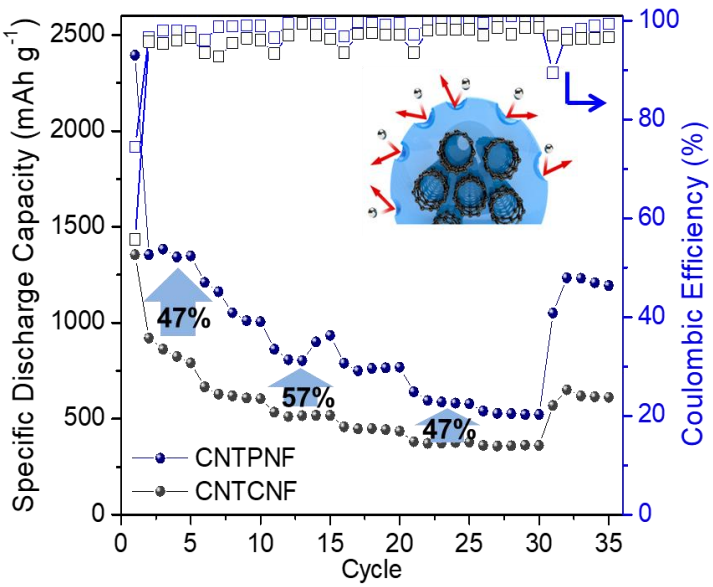

Figure 4.17 Electrochemical test results at varying current densities (50, 100, 200, 250, 500, 1,000, and 50 mA g^{-1}, respectively.) and capacity enhancement (xx%) by KOH activation for CNTCNF, which had no template polymer; Schematic illustration of (inset in image) CNTPNF;

Raman spectroscopy, which is used widely for characterizing carbon materials, in terms of I_D/I_G ratio, was used to examine the effects of KOH activation further. The intensity ratio of two dominant peaks of the D band and G band, which correspond to graphitic layers and disordered or defective carbon, respectively, indicates the degree of defects in carbon materials.[56, 65-67] As shown in Fig. 4.18, I_D/I_G of MC CNTPNF (0.91) was lower than the value of MC CNTCNF (1.47) despite the generation of micropores during KOH activation. This might be due to the partial graphitization of PAN during activation because the process temperature was high enough to induce the graphitization of PAN, leading to a decrease in I_D/I_G.[65] The KOH activation temperature also strongly affects the properties of carbon materials, as shown Fig. 4.18. By the increase of the thermal treatment temperature from 500 to 650, 750, and 850 ^{o}C, the I_D/I_G of the samples showed a decreasing tendency: 1.47, 1.40, 0.91, and 0.93, respectively. This correlation shows that the partial graphitization of PAN is dominant at temperatures higher than 750 ^{o}C and surpasses the effects of micropore development, the force to increase the number of carbon defects.

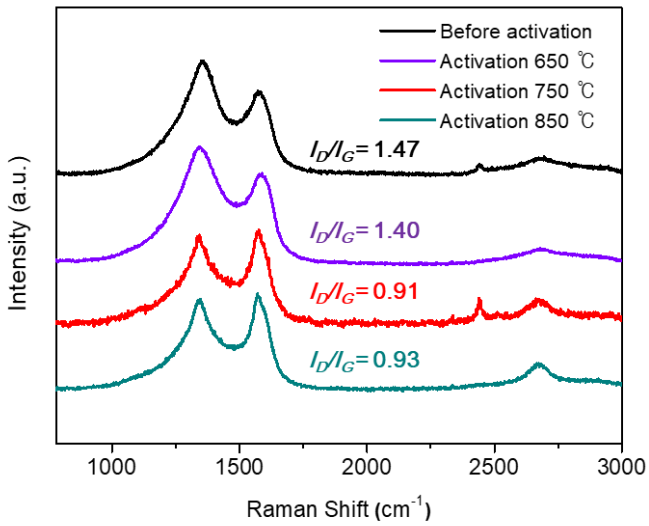

Figure 4.18 Raman spectra with I_D/I_G ratio of each sample.

The change in defect and graphitic carbon is closely related to the chemical properties of N in the samples. Elemental analysis and XPS analysis were conducted to examine the change in N content and its bonding configuration by the KOH activation process, as shown in Fig. 4.19a and 19c. The structural integrity and activation temperature both strongly affect the chemical properties of the samples. The N content was reduced during KOH activation at 750 ^{o}C and quaternary N newly appeared. In comparison with Fig. 4.6, pyridinic N might be changed to quaternary N (9 % in MC CNTPNF and 12 % in CNTPNF) during the thermal treatment, considering that similar portions of pyrrolic N were characterized in the samples (from 68 % in MC CNTCNF to 72 % in MC CNTPNF and from 46 % in CNTCNF to 52 % in CNTPNF). The activation temperature also greatly affects the N contents and its bonding configuration, as summarized in Fig. 4.19c. As the activation temperature was increased, the overall N content decreased with increasing portion of quaternary N. As shown in Table 5.3, there might be some trade-off between the N configuration and pore development.

Table 4.3 N contents and specific surface area of each sample

	N contents (wt. %)	Quaternary N (wt. %)	Specific surface area ($m^2 g^{-1}$)
MC CNTCNF	11.5	0	74
MC CNTPNF-650	11.5	0	493
MC CNTPNF-750	3.9	9	1217
MC CNTPNF-850	2.6	24	1200

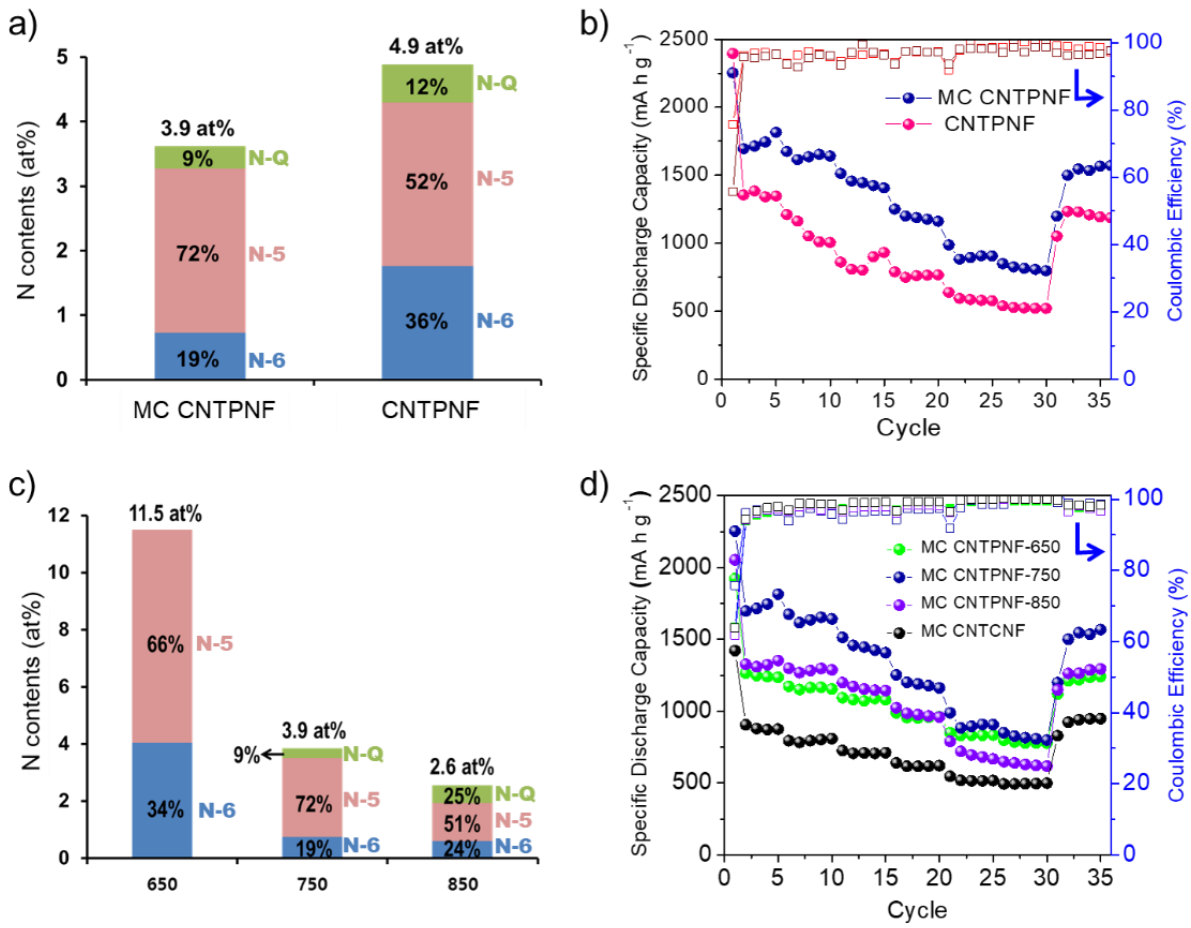

Figure 4. 19 (a) N bonding configuration percentages of MC CNTPNF and CNTPNF activated at 750 ^{o}C and (b) corresponding electrochemical test results at varying current densities (50, 100, 200, 250, 500, 1,000, and 50 mA g^{-1}, respectively.); (c) change in N bonding configuration depending on the activation temperature and (d) corresponding electrochemical test results of activated MC CNTCNF samples at the same varying current densities with (b)

As shown in Fig. 4.19c and 19d, the N content decreased while the portion of quaternary N, which impedes lithium ion storage compared to pyrrolic and pyridinic N [56, 68] is increased with increasing activation temperature.[48] On the other hand, all of the activated samples delivered higher capacities at all charge/discharge current densities despite the decreased amount of N. According to the CV curves (Fig. 4.16a) of the samples we can tentatively conclude that the development of triple junctions through the formation of ion channels is prerequisite for improving the electrochemical performance. The simple increase of N contents does not result in the higher performance unless it is accessible by the redox species. Indeed, The more rectangular-like CVs at around 0.2-3 V, which is due to the storage of lithium ion in the micropores and the surface faradaic reaction with N-, O- functional groups[69] is shown by MC CNTPNF than by MC CNTCNF. In addition, the higher peak cuurent at below 0.l V of the MC CNTPNF indicates the easier accessibility to the triple junctions due to the development of ion channels by KOH activation.[69, 70] Of course, capacity fading is obviously expected if too much N has disappeared due to a lack of redox sites. This is supported by the lower capacity of MC CNTPNF-850 compared to MC CNTPNF-750 and MC CNTPNF-650 (Fig. 4.19d).

Consequently, KOH activation on CNFs expands the number of accessible redox sites from the surface of the material to every part of the material, including the surface, inner part, and also the interfaces between CNT and CNF (Fig. 4.16b). In addition, rapid-ion accessible pores, whose pore size is above approximately 30nm, are connected hierarchically to the abundant micropores by KOH activation, maximizing the triple junction and resulting in higher capacity and higher rate capability than the PNC. Regarding the KOH activation temperature, 650 or 750 ^{o}C were found to be effective in developing an adequate porous structure, as determined by the effective specific area increase for improved capacity indices with the electrochemical test results.

4.2.2 Effects of CNTs on modifying surface characteristics of space

The addition of CNTs in electrode materials facilitates electron transfer by reducing the charge transfer resistance and improving the capacity by providing an electrical pathway to insulating redox particles.[39] The electrical conductivities of 4 different samples were measured to examine the effects of CNT quantitatively: MC CNTPNF (Not electrospun), PNF, CNTPNF, and MC CNTPNF, as summarized in Table 5.4. The measured electrical conductivities of PNF, MC CNTPNF (Not Spun), and MC CNTPNF were 0.05, 0.41, and 86.14 S m^{-1}, respectively. This suggests that an effective electrical pathway by CNTs might be formed only if the CNTs are highly aligned, as confirmed by Fig. 4.5d, supporting the merit of the co-polymer electrospinning method by suppressing aggregation and aligning the CNTs along the uniaxial shear force by the electrical force in the electrospinning process. To examine the contribution on the electrical pathway further, the electrical conductivity of CNTPNF, whose CNTs are in a crumbled 1D structure (0.92 S m^{-1}), was also measured and compared with the aligned and densely packed CNT (86.14 S m^{-1}). The huge difference between the two indicates that how the CNTs are oriented in composite materials is essential in the formation of an electrical pathway, rather than the merely existence of CNTs in the composite. This result is consistent with the electrochemical test results in Fig. 4.19b and polarized Raman spectra in Fig. 4.5d and 5e. Consequently, only when CNTs are uniaxially and densely oriented in a material and adequately wrapped with thin PNC does an effective electron transfer pathway form.

Table 4.4 Summary for each sample.

	Electrospinning	CNT	Template polymer	Morphology	Electrical conductivity (S m^{-1})
MC CNTPNF (Not Spun)	X	O	O	CNTs are randomly scattered within partially graphitized carbon, whose morphology is not 1D	0.41
PNF	O	X	O	1D morphology is not retained during thermal treatment, showing broken PNC	0.05
CNTPNF	O	O	X	CNTs are confined under thick PNC surface and randomly oriented. Some fibers are wrecked	0.92
MC CNTPNF	O	O	O	CNTs are uniaxially packed with thin PNC layer	86.14

Furthermore, an interesting change was observed depending on the existence of CNTs, which indicates the role of CNTs in the partial graphitization step of PAN to PNCs as well as enhancing the electrical conductivity. Maitra *et al*. reported that CNTs can act as an efficient template for graphitization in PAN-derived carbon and there was high graphitization near the walls of the CNTs in CNT-PAN composite.[71] To determine the role of CNTs even under the condition of KOH activation, a visual inspection by TEM, Raman spectroscopy, and XPS were carried out collectively on the MC CNTPNF-650 sample. The TEM image of the activated sample in Fig. 4.20b shows a few "more graphitic layers" near the walls of the CNTs, thereby verifying the graphitization prompting effect of CNT on PAN even during the KOH activation process. This can be explained further by the π- π interaction between the cyano group and CNTs during the wrapping process, leading to the alignment of the cyano group in PAN along the crystalline walls of the CNTs.[49, 72] The presence of CNTs in the electrospun fiber further affect the cyclization, graphitization, and bonding configurations of N during the subsequent KOH activation step *via* π-π interactions between the cyano group and CNTs. The X-ray diffractoram (Fig. 4.14d) and the I_D/I_G ratio of PNF with/without CNTs indirectly support the graphitization prompting effect of CNTs by giving a lower I_D/I_G value of 0.93 for MC CNTPNF (1.20 for PNF) in Fig. 4.20c.

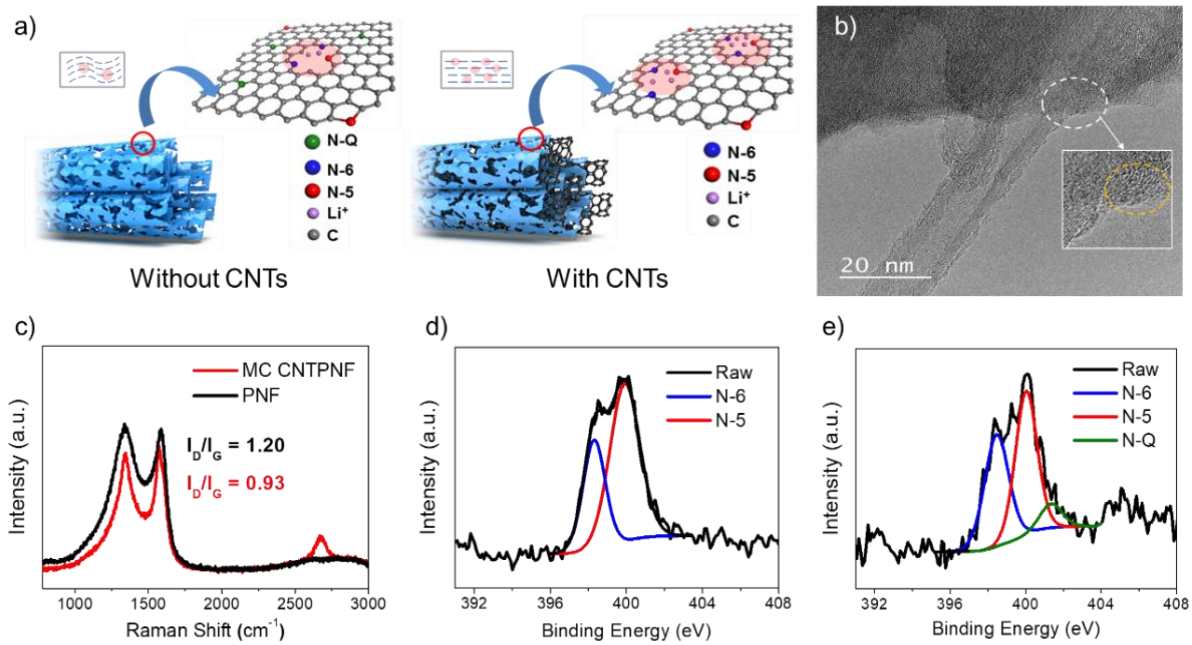

Figure 4.20 (a) Schematic diagram of the change in the N-bonding configuration depending on the presence of CNTs; (b) TEM images of MC CNTPNF with evidence on the partial graphitization of PAN; (c) Raman spectra with an I_D/I_G ratio of sample with/without CNTs; XPS analysis on (d) MC CNTPNF-650 (with CNTs) and (e) PNF-650 (without CNTs)

The N bonding configurations were characterized by XPS to determine the effects of the alignment of the cyano group in PAN along the CNT walls by the π- π interaction, as shown in Fig. 4.20d and 19e. Generally when PAN is treated thermally below 1573 K for graphitization, XPS shows three main N 1s peaks: shows pyridinic N (N-6, 398.4±0.2), pyrrolic or pyridonic N (N-5, 399.8±0.2), and quaternary N (N-Q, 400.7±0.4).[48] The N bonding configurations of the partially graphitized PAN on CNTs (MC CNTPNF-650) was 66% N-5 and 34% N-6 without any N-Q. On the other hand, the absence of CNTs resulted in the newly appeared 8% N-Q with 49% N-5 and 43% N-6. This clear change in the N bonding configuration depending on whether CNTs are present (Fig. 4.20a) supports the effect of the alignment of the cyano group in PAN along the CNT walls on the PAN during the pyrolysis process.

Before discussing the electrochemical test results to examine the effect of CNTs on changing N-bonding configuration, the mechanism of the improvement of the electrochemical performance should be noted. As illustrated as a pink-colored circle in Fig. 4.20a, the “edge site” N atoms in N-5 and N-6 form are beneficial to Li^+ storage for following reasons.[56] Since doping nitrogen would alter the chemical and electronic properties of carbon host, subsequently make stronger interaction between *N*-doped carbon and lithium ion.[73, 74] Especially, it is indicated by recent researches that divacancy and Stone-Wales defect, which is introduced by additional n-type carriers in carbon systems and the hybridization between the nitrogen lone pair electrons and the graphene p-electron system, make deficiency to gain electrons from Li ions[15, 73] and consequently kinetics of lithium diffusion and adsorption of Li atoms in *N*-doped carbon matrix are improved.[74, 75]

In this sight, N-5 and N-6 can generate a large number of nanopore-defects with their inner surfaces and provide more active sites for Li^+ storage because these nanopore-defects act as divacancy and Stone-Wales defect,[15, 73] providing a deficiency to gain electrons from lithium.[56, 57] In contrast, quaternary N (N-Q), which is located inside the graphitic carbon plane, is less beneficial for *N*-doped carbon to storage Li ions because it cannot generate nanopore-defects for Li storage and its electron-rich structure hinders Li^+ adsorption.[76, 77] In addition, the high N-Q content in the lattice can increase the energy of the carbon framework, leading to structural instability during many charge-discharge cycles.[56] In this view, when there is an equivalent nitrogen content, less N-Q and more "edge site" N atoms (N-5, N-6) would be beneficial for Li storage. On the other hand, as heat-treatment temperature increases, a large amount of "edge site" N atoms are converted to N-Q because there is a gradual conversion step for N-5 to N-6 and N-6 to N-Q from 773 to 1573 K, which is the general heat-treatment temperature for the cyclization and graphitization of *N*-doped carbon sources.[48] Therefore in previous studies, a decrease in the amount of the N-Q form was inevitable. Interestingly, this study overturned the tendency of N-Q formation. This can be explained by the effects of the alignment of the cyano group in PAN along the CNT walls on the PAN pyrolysis process in the presence of CNTs.

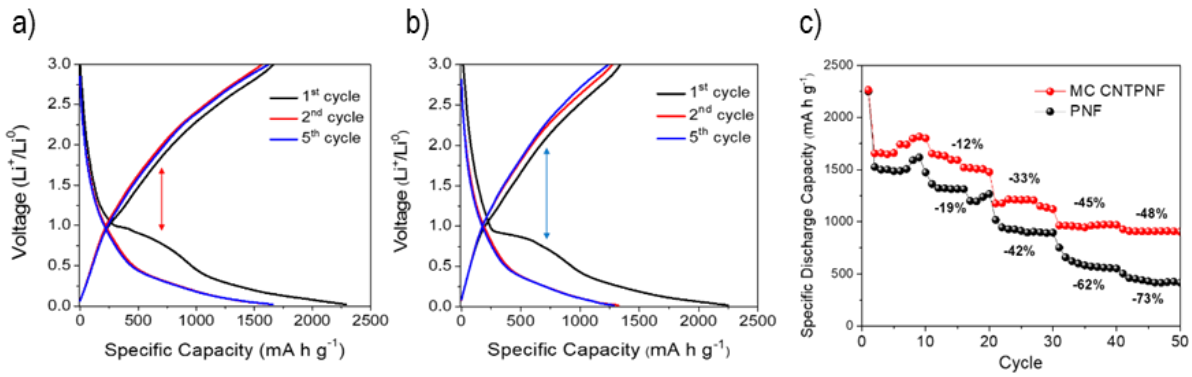

Figure 4.21 (a) Voltage profile of MC CNTPNF (The arrow indicates overpotential of the sample); (b) Voltage profile of PNF; (c) The electrochemical test results (100, 200, 400, 800, and 1000 mA g^{-1}, respectively

Fig. 4.21c clearly demonstrates the superior rate capability of MC CNTPNF compared to PNF. MC CNTPNF retained 52 % of the initial specific discharge capacity at the high current density of 1000 mA g^{-1} while PNF maintained only 27 %. It should be noted that the presence of well-aligned CNTs in the core of fibers helps improving the rate capability by enhancing electron conductivity. This can also be supported by the corresponding voltage profiles (Fig. 4.21a and 21b) showing a much reduced overpotential due to the presece of CNTs. Furthermore in Fig. 4.22, the PNF sample decreased 53% in capacity after 400 cycles at a high current density of 1,000 mA g^{-1} but the MC CNTPNF sample decreased by only 36% even after 400 cycles, indicating better cycling stability as well as higher capacity of the MC CNTPNF. The improved cycling stability of MC CNTPNF resulted from the role of CNTs as a structural scaffold. In Fig. 4.23a and 23b, the PNF electrode showed a relatively shorter and broken morphology after KOH activation compared to Fig. 4.14c and under high current density conditions, its structure had collapsed almost completely. On the other hand, the MC CNTPNF electrode retained its 1D ideal morphology after both KOH activation and under high current density conditions (Fig. 4.23c and 23d).

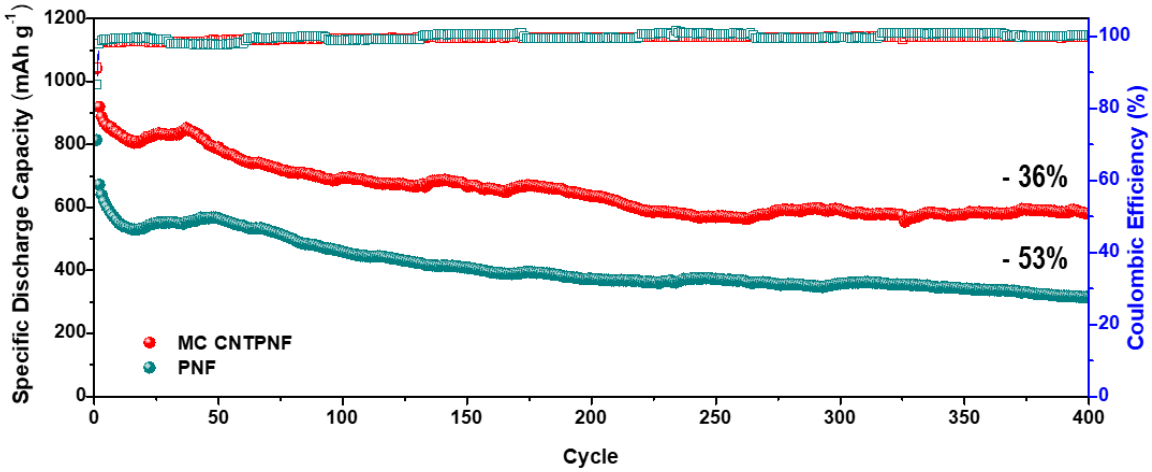

Figure 4.22 Cycling stability test results at a high current density of 1000 mA g^{-1} to evaluate the effect of CNTs

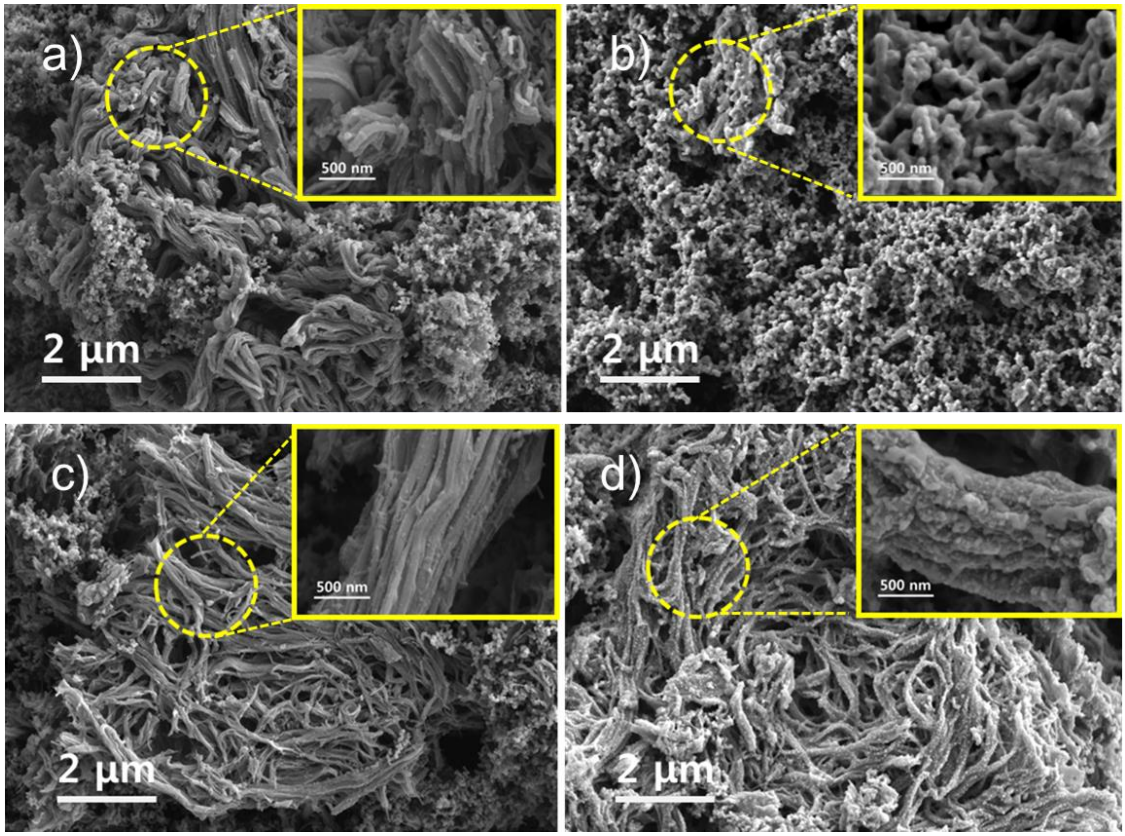

Figure 4.23 (a) PNF made as a coin cell before cycle (b) PNF made as a coin cell after the high C-rate cycles; (c) MC CNTPNF made as a coin cell before cycle; (d) MC CNTPNF made as a coin cell after the high C-rate cycles

Electrochemical impedance spectroscopy (EIS) was also conducted to better understand the measured electrochemical performance of the samples with/without CNTs. The MC CNTPNF electrode showed lower charge transfer resistance in both cases of before/after cycling and lower film resistance in the Nyquist plots (Fig. 4.24). These results are accordance with the electrical conductivity data and electrochemical test results, reconfirming the positive effects of aligned CNTs. Interestingly, the resistance was reduced during cycling in both samples regardless of the presence of CNTs. This can be explained by the activation and electrolyte wetting of the ion channels, which has been reported.[67, 78, 79]

Finally, to determine precisely the effects of the enhanced electrical conductivity of CNTs on the rate capability, anodes with polyvinyline fluoride (2 wt. %), carbon black (3 wt. %), active material (95 wt. %) were prepared. As increasing the performance with decreasing binder and conductive carbon has been a major strategy to increase the capacity of commercial secondary batteries in recent years,[80, 81] this experiment is of great significance for practical commercial secondary batteries. Although MC CNTPNF retained 819 mA h g^{-1} at 1000 mA g^{-1} from 1643.6 mA h g^{-1} at 100 mA g^{-1}, the low-binder and conductive carbon MC CNTPNF showed a relatively lower capacity of 956.7 mA h g^{-1} at 100 mA g^{-1} and retained 401.2 mA h g^{-1} at 1000 mA g^{-1} (Fig. 4.25). On the other hand, this value still indicates greatly enhanced performance compared to the commercial graphite anode. Moreover, the low-binder and conductive carbon PNF without CNTs showed similar capacity to the low-binder and conductive carbon MC CNTPNF at a low current rate but the absence of CNTs resulted in huge capacity drop to 269.1 mA h g^{-1} at a high current density of 1000 mA g^{-1}. This difference in rate capability at a high current rate indicates the importance of CNTs in its electrochemical performance by increasing the electrical conductivity of the material. This improvement of both the rate capability and cycling ability are due to the synergistic effects of the improved charge transfer through the facilitated electrical pathway of the CNTs, the favorable N bonding configurations due to the presence of CNTs, and their role as a structural scaffold within the material.

a)

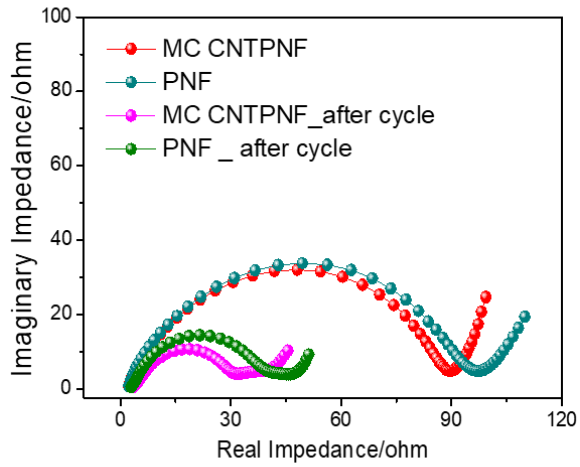

b)

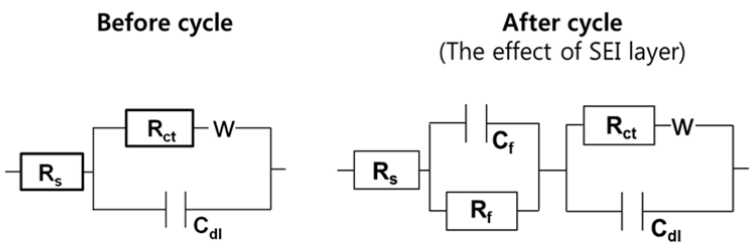

	R_s (Ω)	R_{ct} (Ω)	R_f (Ω)
MC CNTPNF Before cycling	2.2	83.4	-
PNF Before cycling	2.3	88.0	-
MC CNTPNF After cycling	3.4	20.6	3.4
PNF After cycling	2.9	28.8	7.7

Figure 4.24 (a) Nyquist plots of the prepared samples before/after cycling from impedance and (b) equivalent circuits for Nyquist plot of the sample before and after cycling

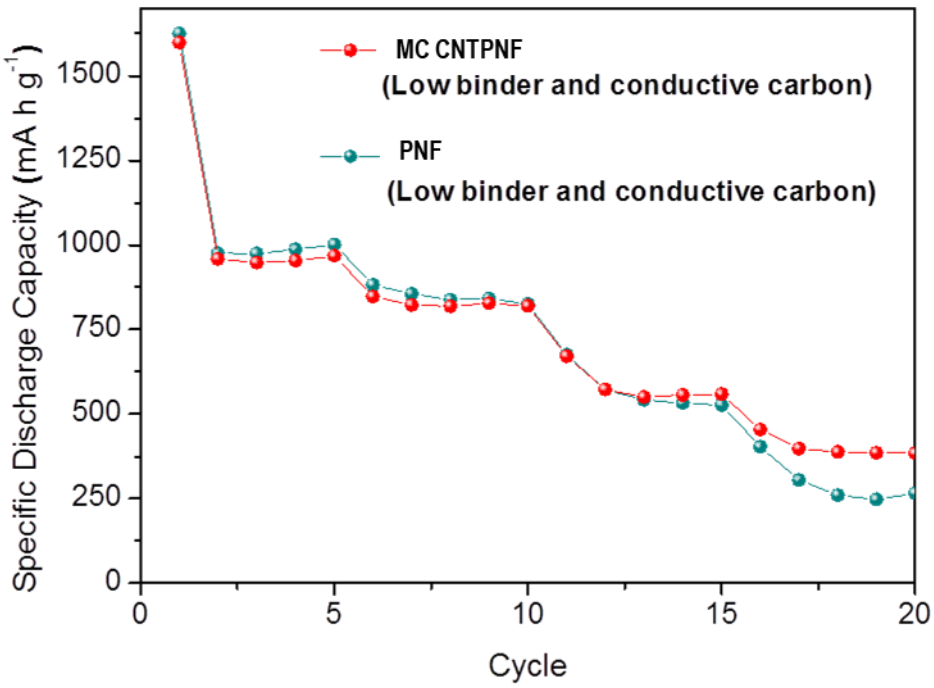

Figure 4.25 The electrochemical test results of the low-binder and conductive carbon MC CNTPNF and PNF at varying current densities (100, 200, 500, and 1000 mA g^{-1}, respectively.)

To investigate the effect of N bonding configuration in MC CNTPNF samples, normalized amount of N-5, N-6 and N-Q were ploted against normalized specific discharge capacity. Normailization by specific surface area is required to consider a huge difference in the SSA of MC CNTPNF samples. Based on Fig. 4.26, we could conclude that the specific discharge capacity normalized by SSA increases linearly with the amount of N-5 and N-6 per SSA and decreases linearly with the amount of N-Q. This result implies that the increasing N-5 and N-6 per unit surface area is critical in the electrode ability of lithium storage. The precise mechanism for the chemistry of the N-bonding configurations in the presence of CNTs might require further investigation. Nevertheless, this work sheds light on the role of CNTs and the effects of the thermal treatment temperature on the development of effective N bonding configurations

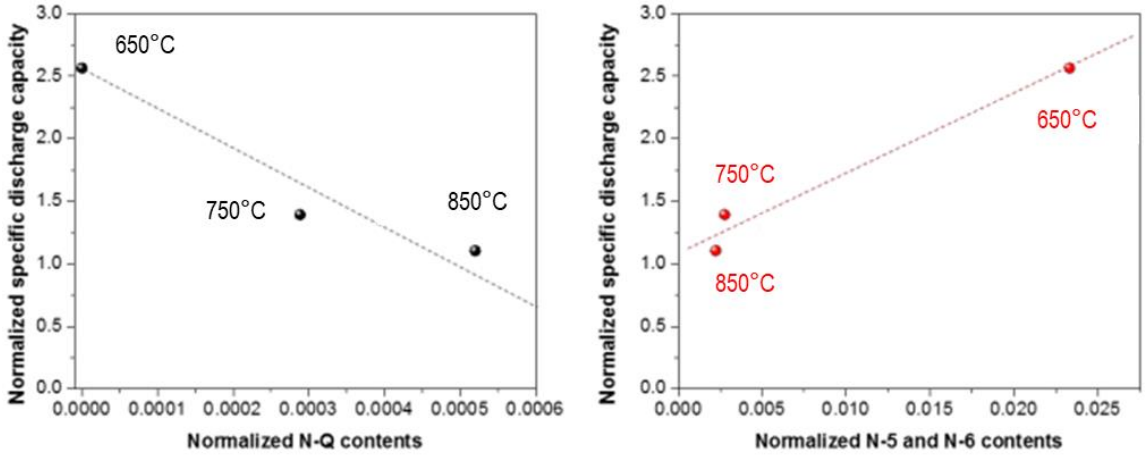

Figure 4. 26 (a) Correlation between specific capacity and the harmful N-Q normalized by the specific surface area of the sample (b) Correlation between specific capacity and the beneficial N configuration normalized by the specific surface area of the sample

4.3 Conclusion

1D partially graphitized *N*-doped hierarchical porous carbon with uniaxially packed CNTs in the core were prepared by co-polymer single nozzle electrospinning, carbonization, and KOH activation. Densely and uniaxailly packed CNTs in the core acted as a structural scaffold and improved the electrical conductivity, enhancing the rate capability and cycling ability of the anode. The partially graphitized *N*-doped LTC shell verified by the BET data and subsequent electrochemical tests indicated that only when a rapid ion-accessible hierarchical pore network is guaranteed will efficient redox sites be expanded from the surface of the material to the entire material and interact with the large surface coverage on CNTs, thereby maximizing the triple junction. The improved electrochemical performance was evaluated by three factors: 1) a facile method to orientate CNTs in a 1D morphology using the slow-envelopment phenomenon, 2) an effective way to realize the hierarchical structure and their property changes of PNCs, and 3) role of CNTs in the formation of an electrical pathway and the partial graphitization of PAN during the thermal treatment. As a result, this material displayed superior reversible capacity of 1814.30 mA h g^{-1} at 50 mA g^{-1}, and 850.10 mA h g^{-1} at 1000 mA g^{-1}. Furthermore, the reversible capacity decreased only 36 % even after 400 cycles and showed superior rate capability than the same material without CNTs. In addition, the unexpected role of the CNTs in changing the nitrogen bonding configuration in *N*-doped carbon for better Li ion storage was discussed. These findings not only suggest an ideal way to design CNT-LTC anode materials to maximize the triple junction, but also shed light on controlling a favorable nitrogen bonding configuration by adopting CNTs in *N*-doped carbon materials.

4.4 Experimental section

4.4.1 Chemicals and materials

Polyacrylonitrile (PAN; Mw 150,000; Aldrich), poly(methyl methacrylate) (PMMA; Mw 120,000; Aldrich), potassium hydroxide (KOH; Aldrich), N,N′-dimethylformamide (DMF; Daejung, Korea), and the as-produced multi-walled carbon nanotubes, synthesized by a catalytic chemical vapor deposition process, (MWCNTs, CM250, Hanhwa Chemical) were purchased and used as received.

4.4.2 Electrospinning and post treatment

To prepare the electrospinning dope solution, specified amounts of PAN, the orientation-controlling polymer, were dissolved in 10mL of DMF with stirring at 90 ^{o}C for 4h. After the PAN was fully dissolved, 50 mg of MWCNTs were dispersed into the solution by tip-sonication for 1h and ultra-centrifuged at 5000 RPM for 40 min. Finally, specific amounts of PMMA, which make 20 wt. % of the total polymer concentration with PAN, were dissolved overnight into the solution. The electrospinning dope solution was loaded into a syringe connected to a metal needle (gauge no. 28, inner diameter 0.18 mm) nozzle and electrospun at a rate of 1.0 mL h^{-1} in air at a voltage of 19.5 kV The distance from the nozzle to the grounded collector was approximately 18 cm and the temperature was approximately 22-25 ^{o}C with 18-20 % relative humidity.

After the electrospinning step, electrospun fiber was heated to 500 ^{o}C in a nitrogen atmosphere at a heating rate of 5 ^{o}C/min and maintained at that temperature for 3h to fully decompose PMMA and glue the MWCNTs with PAN. Subsequently, the prepared nanofibers were dispersed with a KOH solution (50mL distilled water and 50mL ethanol) by tip-sonication for

20 min and dried with stirring overnight on a hot plate. The weight ratio of the nanofibers and KOH was 1:4. When all solvents were dried, prepared mixture of nanofibers and KOH were heated to 650 ^{o}C, 750 ^{o}C, and 850 ^{o}C in a nitrogen atmosphere at a heating rate of 5 ^{o}C/min and maintained at either of those temperatures for 1h for KOH activation. Subsequently, the prepared activated nanofibers were stirred in 1M HCl for 2.5h and washed with distilled water until the pH of the filtrate was approximately 7. Finally, activated partially graphitized porous *N*-doped carbon (MC CNTPNF) was obtained after drying at 80 ^{o}C overnight. For comparison, the same sample without the MWCNTs was prepared and a sample without PMMA was prepared by dissolving 12 wt. % PAN to obtain the minimum concentration for electrospinning.

4.4.3 Characterization

Field emission scanning electron microscopy (FESEM; MERLIN Compact) and transmission electron microscopy (TEM; JEM-2100F and Tecnai F20) were conducted to verify the 1-D morphologies of the samples and uniaxial orientation of MWCNTs. In addition, to determine how much the electrical conductivity can be enhanced by incorporating MWCNTs uniaxially, the samples were pelletized and measured using a M4P-205 4 point probe station (MSTECH). An elemental analyzer (EA; Flash EA 1112) was used to measure the quantity of each element. The surface chemical characteristics of the samples were investigated by X-ray photoelectron spectroscopy (XPS; AXISHIS, Kratos). The specific surface areas and pore volume distributions were examined based on the Brunauer-Emmett-Teller (BET) equation[82] using a Micromeritics ASAP 2020 static volumetric gas adsorption instrument. The intensity ratio of the D and G bands of the samples was measured by Raman spectroscopy (Raman plus, Nanophoton). In addition, polarized Raman spectroscopy was used to examine the degree of orientation of the CNTs.

4.4.4 Electrochemical measurements

To investigate the electrochemical performance of the prepared samples, all anodes were prepared by the doctor blade method using polyvinylidene fluoride (15 wt. %), carbon black (15 wt. %), and active material (70 wt. %). The prepared slurry was coated on a copper current collector and dried for 12 hours at 80 ^{o}C under vacuum. A 1 M $LiFP_6$ solution in EC/DEC (1:1 volume ratio) was used as the electrolyte. The electrochemical performance was evaluated using a battery cycler (WBCS3000, WonATech) and a potentiostat (ZIVE SP2, WonATech) with assembled 2032 coin-type half-cells. The electrochemical performance was investigated in the 0.02-3.0 V potential range against Li/Li^+. Cyclic voltammetry (CV) experiments were carried out at a scanning rate of 20 mV s^{-1} between 0.02 V and 3 V *versus* Li/Li^+. Electrochemical impedance spectra were obtained at the open circuit voltage over the frequency range of 10 mHz to 10 kHz with an AC amplitude of 5 mV.

4.5 References

[1] Y.C. Jeong, K. Lee, T. Kim, J.H. Kim, J. Park, Y.S. Cho, S.J. Yang, C.R. Park, Partially unzipped carbon nanotubes for high-rate and stable lithium-sulfur batteries, Journal of Materials Chemistry A 4(3) (2016) 819-826.

[2] J.H. Kim, M. Byeon, Y.C. Jeong, J.Y. Oh, Y. Jung, N. Fechler, S.J. Yang, C.R. Park, Morphochemical imprinting of melamine cyanurate mesocrystals in glucose-derived carbon for high performance lithium ion batteries, Journal of Materials Chemistry A 5(39) (2017) 20635-20642.

[3] Y.C. Jeong, J.H. Kim, S.H. Kwon, J.Y. Oh, J. Park, Y. Jung, S.G. Lee, S.J. Yang, C.R. Park, Rational design of exfoliated 1T MoS2@CNT-based bifunctional separators for lithium sulfur batteries, Journal of Materials Chemistry A 5(45) (2017) 23909-23918.

[4] M.V. Reddy, G.V. Subba Rao, B.V.R. Chowdari, Metal Oxides and Oxysalts as Anode Materials for Li Ion Batteries, Chemical Reviews 113(7) (2013) 5364-5457.

[5] A.R. Armstrong, C. Lyness, P.M. Panchmatia, M.S. Islam, P.G. Bruce, The lithium intercalation process in the low-voltage lithium battery anode Li1+xV1−xO2, Nature Materials 10 (2011) 223.

[6] P. Poizot, S. Laruelle, S. Grugeon, L. Dupont, J.M. Tarascon, Nano-sized transition-metal oxides as negative-electrode materials for lithium-ion batteries, Nature 407 (2000) 496.

[7] P.L. Taberna, S. Mitra, P. Poizot, P. Simon, J.M. Tarascon, High rate capabilities Fe3O4-based Cu nano-architectured electrodes for lithium-ion battery applications, Nature Materials 5 (2006) 567.

[8] M.S. Dresselhaus, G. Dresselhaus, Intercalation compounds of graphite, Advances in Physics 30(2) (1981) 139-326.

[9] N.A. Kaskhedikar, J. Maier, Lithium storage in carbon nanostructures, Advanced Materials 21(25-26) (2009) 2664-2680.

[10] J. Liu, Addressing the grand challenges in energy storage, Advanced Functional Materials 23(8) (2013) 924-928.

[11] R. Yazami, P. Touzain, A reversible graphite-lithium negative electrode for electrochemical generators, Journal of Power Sources 9(3) (1983) 365-371.

[12] K. Totsumi, N. Washita, H. Sakaebe, H. Shioyama, S. Higuchi, The Influence of the Graphitic Structure on the Electrochemical Characteristics for the Anode of Secondary Lithium Batteries, Journal of the Electrochemical Society 142(3) (1995) 716-720.

[13] C.S. Wang, G.T. Wu, W.Z. Li, Lithium insertion in ball-milled graphite, Journal of Power Sources 76(1) (1998) 1-10.

[14] Y.-P. Wu, C.-R. Wan, C.-Y. Jiang, S.-B. Fang, Y.-Y. Jiang, Mechanism of lithium storage in low temperature carbon, Carbon 37(12) (1999) 1901-1908.

[15] J.R. Dahn, T. Zheng, Y. Liu, J.S. Xue, Mechanisms for lithium insertion in carbonaceous materials, Science 270(5236) (1995) 590-593.

[16] H. Benaddi, T.J. Bandosz, J. Jagiello, J.A. Schwarz, J.N. Rouzaud, D. Legras, F. Béguin, Surface functionality and porosity of activated carbons obtained from chemical activation of wood, Carbon 38(5) (2000) 669-674.

[17] E. Frackowiak, F. Béguin, Carbon materials for the electrochemical storage of energy in capacitors, Carbon 39(6) (2001) 937-950.

[18] H. Wang, X. Zhang, Y. Zhang, N. Cheng, T. Yu, Y. Yang, G. Yang, Study of carbonization behavior of polyacrylonitrile/tin salt as anode material for lithium-ion batteries, 2016.

[19] X. Dong, C. Lu, L. Wang, P. Zhou, D. Li, L. Wang, G. Wu, Y. Li, Polyacrylonitrile-based turbostratic graphite-like carbon wrapped silicon nanoparticles: a new-type anode material for lithium ion battery, RSC Advances 6(16) (2016) 12737-12743.

[20] J.K. Lee, K.W. An, J.B. Ju, B.W. Cho, W.I. Cho, D. Park, K.S. Yun, Electrochemical properties of PAN-based carbon fibers as anodes for rechargeable lithium ion batteries, Carbon 39(9) (2001) 1299-1305.

[21] C. Kim, K.S. Yang, M. Kojima, K. Yoshida, Y.J. Kim, Y.A. Kim, M. Endo, Fabrication of Electrospinning-Derived Carbon Nanofiber Webs for the Anode Material of Lithium-Ion Secondary Batteries, Advanced Functional Materials 16(18) (2006) 2393-2397.

[22] X. Qin, H. Zhang, J. Wu, X. Chu, Y.-B. He, C. Han, C. Miao, S. Wang, B. Li, F. Kang, Fe3O4 nanoparticles encapsulated in electrospun porous carbon fibers with a compact shell as high-performance anode for lithium ion batteries, Carbon 87 (2015) 347-356.

[23] E. Frackowiak, F. Béguin, Electrochemical storage of energy in carbon nanotubes and nanostructured carbons, Carbon 40(10) (2002) 1775-1787.

[24] D. Zhu, C. Xu, N. Nakura, M. Matsuo, Study of carbon films from PAN/VGCF composites by gelation/crystallization from solution, Carbon 40(3) (2002) 363-373.

[25] R. Janus, P. Natkański, A. Wach, M. Drozdek, Z. Piwowarska, P. Cool, P. Kuśtrowski, Thermal transformation of polyacrylonitrile deposited on SBA-15 type silica, Journal of Thermal Analysis and Calorimetry 110(1) (2012) 119-125.

[26] J.Y. Howe, G.G. Tibbetts, C. Kwag, M.L. Lake, Heat treating carbon nanofibers for optimal composite performance, Journal of Materials Research 21(10) (2006) 2646-2652.

[27] A. Ramos, I. Cameán, A.B. García, Graphitization thermal treatment of carbon nanofibers, Carbon 59 (2013) 2-32.

[28] T.W. Ebbesen, H.J. Lezec, H. Hiura, J.W. Bennett, H.F. Ghaemi, T. Thio, Electrical conductivity of individual carbon nanotubes, Nature 382(6586) (1996) 54-56.

[29] C. Biswas, Y.H. Lee, Graphene versus carbon nanotubes in electronic devices, Advanced Functional Materials 21(20) (2011) 3806-3826.

[30] Y. Ando, X. Zhao, H. Shimoyama, G. Sakai, K. Kaneto, Physical properties of multiwalled carbon nanotubes, International Journal of Inorganic Materials 1(1) (1999) 77-82.

[31] M.F. Yu, O. Lourie, M.J. Dyer, K. Moloni, T.F. Kelly, R.S. Ruoff, Strength and breaking mechanism of multiwalled carbon nanotubes under tensile load, Science 287(5453) (2000) 637-640.

[32] M.M.J. Treacy, T.W. Ebbesen, J.M. Gibson, Exceptionally high Young's modulus observed for individual carbon nanotubes, Nature 381(6584) (1996) 678-680.

[33] B. Gao, A. Kleinhammes, X.P. Tang, C. Bower, L. Fleming, Y. Wu, O. Zhou, Electrochemical intercalation of single-walled carbon nanotubes with lithium, Chemical Physics Letters 307(3-4) (1999) 153-157.

[34] Y. Chen, X. Li, K. Park, J. Song, J. Hong, L. Zhou, Y.-W. Mai, H. Huang, J.B. Goodenough, Hollow Carbon-Nanotube/Carbon-Nanofiber Hybrid Anodes for Li-Ion Batteries, Journal of the American Chemical Society 135(44) (2013) 16280-16283.

[35] B. Zhang, J. Huang, J.-K. Kim, Ultrafine Amorphous SnOx Embedded in Carbon Nanofiber/Carbon Nanotube Composites for Li-Ion and Na-Ion Batteries, Advanced Functional Materials 25(32) (2015) 5222-5228.

[36] Y. Li, G. Xu, L. Xue, S. Zhang, Y. Yao, Y. Lu, O. Toprakçı, X. Zhang, Enhanced Rate Capability by Employing Carbon Nanotube-Loaded Electrospun Si/C Composite Nanofibers As Binder-Free Anodes, 2013.

[37] H. Dai, Carbon nanotubes: Opportunities and challenges, Surface Science 500(1-3) (2002) 218-241.

[38] F. Ko, Y. Gogotsi, A. Ali, N. Naguib, H.H. Ye, G.L. Yang, C. Li, P. Willis, Electrospinning of Continuous Carbon Nanotube-Filled Nanofiber Yarns, 2003.

[39] J.W. Yang Wu, Kaili Jiang, Shoushan Fan, Applications of carbon nanotubes in high performance lithium ion batteries, Front. Phys. 9(3) (2014) 351-369.

[40] X.-M. Liu, Z.d. Huang, S.w. Oh, B. Zhang, P.-C. Ma, M.M.F. Yuen, J.-K. Kim, Carbon nanotube (CNT)-based composites as electrode material for rechargeable Li-ion batteries: A review, Composites Science and Technology 72(2) (2012) 121-144.

[41] J.J. Ge, H. Hou, Q. Li, M.J. Graham, A. Greiner, D.H. Reneker, F.W. Harris, S.Z.D. Cheng, Assembly of Well-Aligned Multiwalled Carbon Nanotubes in Confined Polyacrylonitrile Environments: Electrospun Composite Nanofiber Sheets, Journal of the American Chemical Society 126(48) (2004) 15754-15761.

[42] G. Sui, S.S. Xue, H.T. Bi, Q. Yang, X.P. Yang, Desirable electrical and mechanical properties of continuous hybrid nano-scale carbon fibers containing highly aligned multi-walled carbon nanotubes, Carbon 64 (2013) 72-83.

[43] Q. Guo, X. Zhou, X. Li, S. Chen, A. Seema, A. Greiner, H. Hou, Supercapacitors based on hybrid carbon nanofibers containing multiwalled carbon nanotubes, Journal of Materials Chemistry 19(18) (2009) 2810-2816.

[44] Q. Zhang, Z. Chang, M. Zhu, X. Mo, D. Chen, Electrospun carbon nanotube composite nanofibres with uniaxially aligned arrays, Nanotechnology 18(11) (2007).

[45] J.P.F. Santos, A.B. Da Silva, U. Sundararaj, R.E.S. Bretas, Novel electrical conductive hybrid nanostructures based on PA 6/MWCNT<inf>COOH</inf> electrospun nanofibers and

anchored MWCNT<inf>COOH</inf>, Polymer Engineering and Science 55(6) (2015) 1263-1272.

[46] A.-E. Hsiao, S.-Y. Tsai, M.-W. Hsu, S.-J. Chang, Decoration of multi-walled carbon nanotubes by polymer wrapping and its application in MWCNT/polyethylene composites, Nanoscale Research Letters 7(1) (2012) 240.

[47] F. Tsuyohiko, N. Naotoshi, Non-covalent polymer wrapping of carbon nanotubes and the role of wrapped polymers as functional dispersants, Science and Technology of Advanced Materials 16(2) (2015) 024802.

[48] J.R. Pels, F. Kapteijn, J.A. Moulijn, Q. Zhu, K.M. Thomas, Evolution of nitrogen functionalities in carbonaceous materials during pyrolysis, Carbon 33(11) (1995) 1641-1653.

[49] S.S. Tallury, M.A. Pasquinelli, Molecular dynamics simulations of flexible polymer chains wrapping single-walled carbon nanotubes, Journal of Physical Chemistry B 114(12) (2010) 4122-4129.

[50] Y. Kwon, W. Shim, S.Y. Jeon, J.H. Youk, W.R. Yu, Improving dispersion of multi-walled carbon nanotubes and Graphene using a common non-covalent modifier, Carbon letters 20(1) (2016) 53-61.

[51] M.C. Williams, Migration of two liquid phases in capillary extrusion: An energy interpretation, AIChE Journal 21(6) (1975) 1204-1207.

[52] T. Kim, C.R. Park, Preparation and characterization of core-shell type P3HT@PEO composite nanofibers using single nozzle system, ICCM International Conferences on Composite Materials, 2011.

[53] N.A. Seaton, J.P.R.B. Walton, N. quirke, A new analysis method for the determination of the pore size distribution of porous carbons from nitrogen adsorption measurements, Carbon 27(6) (1989) 853-861.

[54] J. Landers, G.Y. Gor, A.V. Neimark, Density functional theory methods for characterization of porous materials, Colloids and Surfaces A: Physicochemical and Engineering Aspects 437 (2013) 3-32.

[55] P.I. Ravikovitch, G.L. Haller, A.V. Neimark, Density functional theory model for calculating pore size distributions: pore structure of nanoporous catalysts, Advances in Colloid and Interface Science 76-77 (1998) 203-226.

[56] F. Zheng, Y. Yang, Q. Chen, High lithium anodic performance of highly nitrogen-doped porous carbon prepared from a metal-organic framework, Nature Communications 5 (2014) 5261.

[57] C. Ma, X. Shao, D. Cao, Nitrogen-doped graphene nanosheets as anode materials for lithium ion batteries: A first-principles study, Journal of Materials Chemistry 22(18) (2012) 8911-8915.

[58] Y. Mao, H. Duan, B. Xu, L. Zhang, Y. Hu, C. Zhao, Z. Wang, L. Chen, Y. Yang, Lithium storage in nitrogen-rich mesoporous carbon materials, Energy & Environmental Science 5(7) (2012) 7950-7955.

[59] S.J. An, J. Li, C. Daniel, D. Mohanty, S. Nagpure, D.L. Wood, The state of understanding of the lithium-ion-battery graphite solid electrolyte interphase (SEI) and its relationship to formation cycling, Carbon 105 (2016) 52-76.

[60] L. Yan, J. Yu, J. Houston, N. Flores, H. Luo, Biomass derived porous nitrogen doped carbon for electrochemical devices, Green Energy & Environment 2(2) (2017) 84-99.

[61] J. Wang, S. Kaskel, KOH activation of carbon-based materials for energy storage, Journal of Materials Chemistry 22(45) (2012) 23710-23725.

[62] Z. Zhou, C. Lai, L. Zhang, Y. Qian, H. Hou, D.H. Reneker, H. Fong, Development of carbon nanofibers from aligned electrospun polyacrylonitrile nanofiber bundles and

characterization of their microstructural, electrical, and mechanical properties, Polymer 50(13) (2009) 2999-3006.

[63] K. Shirvanimoghaddam, M.M. Abolhasani, Q. Li, H. Khayyam, M. Naebe, Cheetah skin structure: A new approach for carbon-nano-patterning of carbon nanotubes, Composites Part A: Applied Science and Manufacturing 95 (2017) 304-314.

[64] Z. Wang, X. Xiong, L. Qie, Y. Huang, High-performance lithium storage in nitrogen-enriched carbon nanofiber webs derived from polypyrrole, Electrochimica Acta 106 (2013) 320-326.

[65] E.J. Ra, K.H. An, K.K. Kim, S.Y. Jeong, Y.H. Lee, Anisotropic electrical conductivity of MWCNT/PAN nanofiber paper, Chemical Physics Letters 413(1-3) (2005) 188-193.

[66] L. Bokobza, J.-L. Bruneel, M. Couzi, Raman spectroscopy as a tool for the analysis of carbon-based materials (highly oriented pyrolitic graphite, multilayer graphene and multiwall carbon nanotubes) and of some of their elastomeric composites, Vibrational Spectroscopy 74 (2014) 57-63.

[67] Y. Jung, Y.C. Jeong, J.H. Kim, Y.S. Kim, T. Kim, Y.S. Cho, S.J. Yang, C.R. Park, One step preparation and excellent performance of CNT yarn based flexible micro lithium ion batteries, Energy Storage Materials 5 (2016) 1-7.

[68] X. Wang, Q. Weng, X. Liu, X. Wang, D.-M. Tang, W. Tian, C. Zhang, W. Yi, D. Liu, Y. Bando, D. Golberg, Atomistic Origins of High Rate Capability and Capacity of N-Doped Graphene for Lithium Storage, Nano Letters 14(3) (2014) 1164-1171.

[69] N. Wang, Q. Liu, B. Sun, J. Gu, B. Yu, W. Zhang, D. Zhang, N-doped catalytic graphitized hard carbon for high-performance lithium/sodium-ion batteries, Scientific Reports 8(1) (2018) 9934.

[70] K. Wenelska, A. Ottmann, D. Moszyński, P. Schneider, R. Klingeler, E. Mijowska, Facile synthesis N-doped hollow carbon spheres from spherical solid silica, Journal of Colloid and Interface Science 511 (2018) 203-208.

[71] T. Maitra, S. Sharma, A. Srivastava, Y.K. Cho, M. Madou, A. Sharma, Improved graphitization and electrical conductivity of suspended carbon nanofibers derived from carbon nanotube/polyacrylonitrile composites by directed electrospinning, Carbon 50(5) (2012) 1753-1761.

[72] J. Lee, J.I. Choi, A.E. Cho, S. Kumar, S.S. Jang, Y.H. Kim, Origin and Control of Polyacrylonitrile Alignments on Carbon Nanotubes and Graphene Nanoribbons, Advanced Functional Materials 28(15) (2018).

[73] Y.X. Yu, Can all nitrogen-doped defects improve the performance of graphene anode materials for lithium-ion batteries?, Physical Chemistry Chemical Physics 15(39) (2013) 16819-16827.

[74] H. Wang, C. Zhang, Z. Liu, L. Wang, P. Han, H. Xu, K. Zhang, S. Dong, J. Yao, G. Cui, Nitrogen-doped graphene nanosheets with excellent lithium storage properties, Journal of Materials Chemistry 21(14) (2011) 5430-5434.

[75] L.J. Zhou, Z.F. Hou, L.M. Wu, First-principles study of lithium adsorption and diffusion on graphene with point defects, Journal of Physical Chemistry C 116(41) (2012) 21780-21787.

[76] Z. Zhou, X. Gao, J. Yan, D. Song, M. Morinaga, A first-principles study of lithium absorption in boron- or nitrogen-doped single-walled carbon nanotubes, Carbon 42(12–13) (2004) 2677-2682.

[77] Y.F. Li, Z. Zhou, L.B. Wang, CNx nanotubes with pyridinelike structures: p-type semiconductors and Li storage materials, Journal of Chemical Physics 129(10) (2008).

[78] X. Hou, Y. Hu, H. Jiang, Y. Li, W. Li, C. Li, One-step synthesis of SnO<inf>x</inf> nanocrystalline aggregates encapsulated by amorphous TiO<inf>2</inf> as an anode in Li-ion battery, Journal of Materials Chemistry A 3(18) (2015) 9982-9988.

[79] B.V. Rami Reddy, R. Ravikumar, C. Nithya, S. Gopukumar, High performance Na<inf>x</inf>CoO<inf>2</inf> as a cathode material for rechargeable sodium batteries, Journal of Materials Chemistry A 3(35) (2015) 18059-18063.

[80] H. Sun, A.E. Del Rio Castillo, S. Monaco, A. Capasso, A. Ansaldo, M. Prato, D.A. Dinh, V. Pellegrini, B. Scrosati, L. Manna, F. Bonaccorso, Binder-free graphene as an advanced anode for lithium batteries, Journal of Materials Chemistry A 4(18) (2016) 6886-6895.

[81] A. Martinez-Garcia, A.K. Thapa, R. Dharmadasa, T.Q. Nguyen, J. Jasinski, T.L. Druffel, M.K. Sunkara, High rate and durable, binder free anode based on silicon loaded MoO3 nanoplatelets, Scientific Reports 5 (2015) 10530.

[82] S. Brunauer, P.H. Emmett, E. Teller, Adsorption of Gases in Multimolecular Layers, Journal of the American Chemical Society 60(2) (1938) 309-319.

Part IV. Conclusion and Perspective

Chapter 5. Concluding Remarks

Demand for high-performance energy storage systems is growing rapidly to achieve a renewable energy economy. Although there have been many improvements in the performance of electrochemical energy storage systems represented by lithium ion batteries, more research is still needed to develop battery materials with both a high energy density and power density that meet the requirements of next-generation batteries at the crossroad from a small electronic device such as smartphones to enormous electric-storage stations and electric vehicles. Among the various requirements for next-generation batteries, fast-charging without capacity decay and stable cycle stability are two of the most important issues to solve [1]. Kinetic issues in the fast charging condition, especially transport of electrochemical species in the anode, affects the degradation of the active material and causes a performance gap between the theoretically predicted and practical ones. State-of-the-arts were revisited at the point of reducing the overpotential in each transport step of the electrochemical species. There is an apparent difference between finding a theoretically superior active material and practically realizing the expected electrochemical performance in the current required electrochemical environments such as fast charging conditions.

Some previous studies have focused on just adopting fancy new materials and showed an enhanced electrochemical performance that could not be maintained under harsh conditions (Fig. 5.1a). As seen in Fig. 5.1b, the primary goal in this research is designing an active material that can maintain the maximum electrochemical performance under any circumstances at the point of the morphology of the active material itself, without any assistance from other factors such as electrode manufacturing or adding surfactants. After the fundamental active material design guideline is set up regardless of which active material is used, the ultimate goal to both enhancing the theoretical and practical performance of a battery could be sincerely meaningful (Fig. 5.1c).

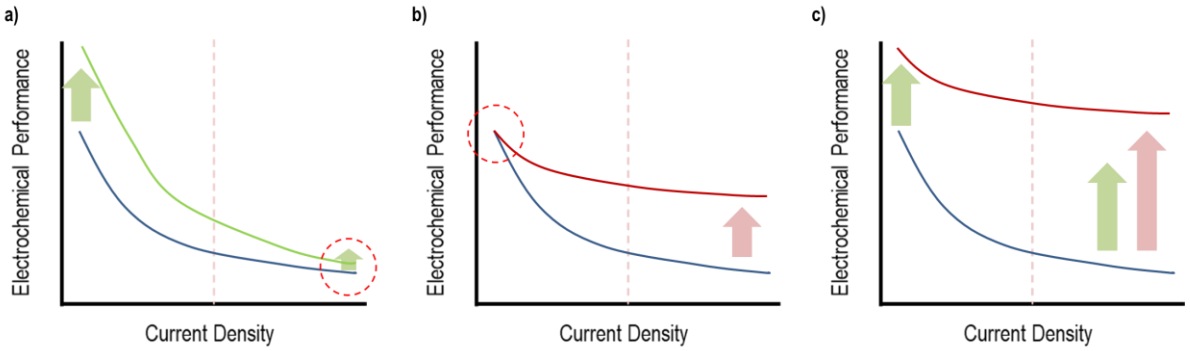

Figure 5.1 (a) Previous cases that focused on enhancing theoretical performance only (b) Goal to maintain theoretical performance under a fast charging condition (c) Goal to enhance both theoretical and practical performance under a fast charging condition

In Part II, the kinetic issues hindering the fast charging of today's LIBs were investigated from a physicochemical and materials' point of view. The overpotentials in a battery system are derived according to the route of the electrochemical species [2, 3].

$$V = -\frac{1}{F}(\tilde{\mu}_{e-}^{c} - \tilde{\mu}_{e-}^{a}) = V_{OC} + \Delta\varphi^{c} + \Delta\varphi^{a} = \Delta\varphi_{AM}^{a} + \Delta\varphi_{CT}^{a} + \Delta\varphi_{EL}^{a}$$

Among the various transport routes, solvated Li-ion transport in an electrolyte-containing active material space is suggested to be a key issue to reduce the overpotential induced by the kinetic limits of Li-ions. The concentration gradient caused by the transport limits and subsequent overpotential ($\Delta\varphi_{EL}^{a}$) is expressed as follows [4].

$$\Delta\boldsymbol{\varphi_{EL}} = \boldsymbol{\mu_{Li^+}} - \boldsymbol{\mu_{Li^+}^{0}} = \frac{\boldsymbol{RT}}{\boldsymbol{F}}\ln\left(\mathbf{1} - \frac{\boldsymbol{I}}{\boldsymbol{j_{lim}A_{\emptyset}}}\right) \sim \boldsymbol{I}\frac{\boldsymbol{T}}{\boldsymbol{j_{lim}A_{\emptyset}}}\ , \quad \boldsymbol{j_{applied}} < \boldsymbol{j_{lim}} = \frac{\boldsymbol{F\tilde{D}_{Li^+}^{EL}c_{Li^+,0}^{EL}}}{(\mathbf{1}-\boldsymbol{t_{Li^+}})\boldsymbol{L_{EL}\beta}}$$

In Part III, rational design guidelines to deduce the appropriate morphology of a 1D carbon nanofiber (CNF) anode material and develop the space characteristics in the active material were derived with the interpretation of the phase separation behavior in an immiscible polymer electrospinning system. Chapter 3 focuses on the rational design and synthesis of CNFs according to the guidelines presented in Part II, and a facile phase separation method to control the ion transport channel with an immiscible polymer blend electrospinning system was also studied through the interpretation of the ternary phase diagram. The correlation between the space characteristics and the transport characteristics of the solvated Li-ions was derived in terms of reducing the overpotential (Fig. 5.2a).

In Chapter 4, N-doped hierarchical porous carbon with uniaxially packed carbon nanotubes (CNTs) was prepared. Densely and uniaxially aligned CNTs and KOH activation hierarchically modified the CNFs, and the correlations between characteristics of each space and the electrochemical performance were discussed in the view of enhancing both the theoretical and practical performance (Fig. 5.1c). Fast transportation of solvated Li-ions through an ion channel by a core shell structure and the subsequent enhanced Li storage behavior on an activated lithiophilic surface were closely investigated according to the findings of the previous parts of this research. In addition, the effect of the CNTs was investigated from a new perspective on modifying the space characteristics of the anode materials and improving the electrical conductivity (Fig. 5.2b).

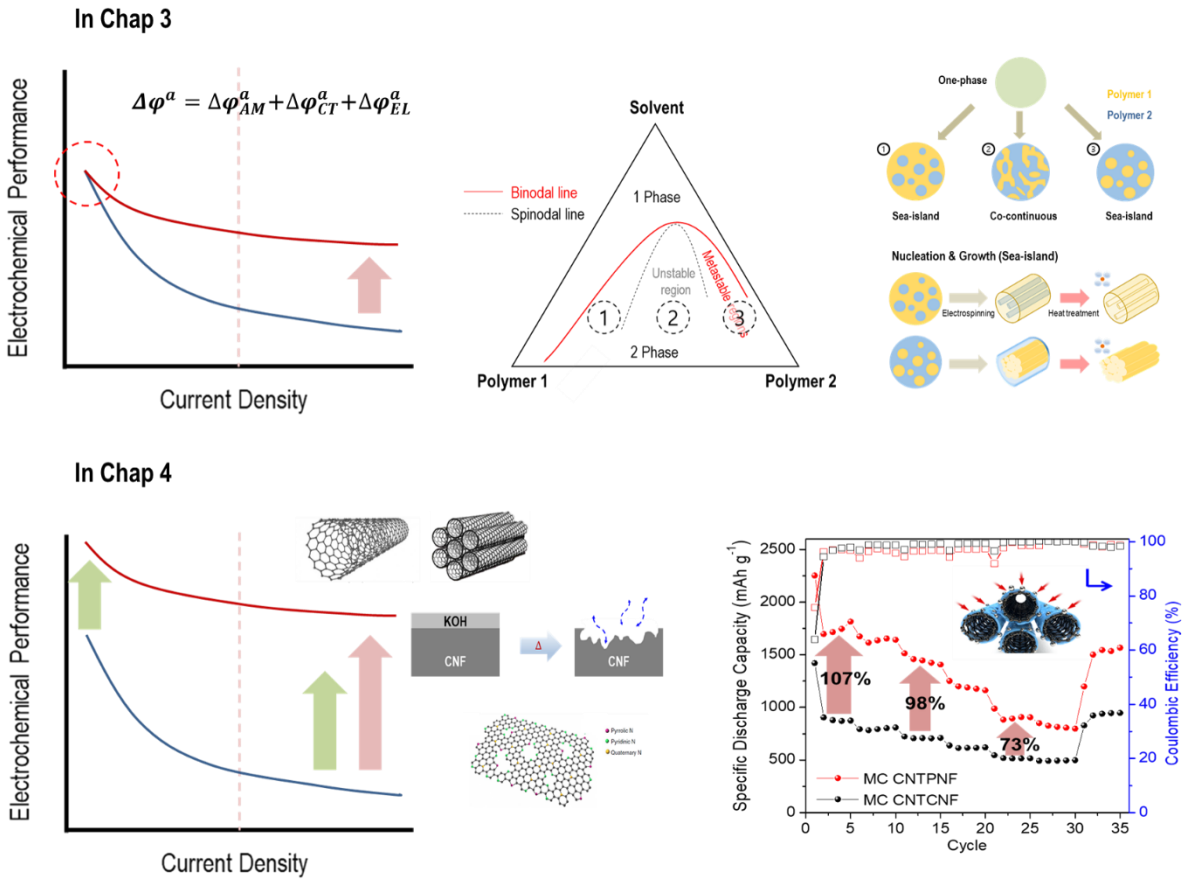

Figure 5.2 Summary of results in chapter 3 and chapter 4

From the point of view in material science, more diverse and versatile materials can be adjusted to be next-generation anode materials, advancing the design guidelines in this research such as the interpretation of the space characteristics in the active material and subsequent effects on the transport characteristics. Additionally, other nanomaterials such as CNTs in this research can be adopted successfully to an anode material considering the guidelines.

Furthermore, the rational design guideline for a fast charging electrode material should be made on a wider scale. Until the electrochemical reaction occurs in a battery system, there are various scales of steps from the region of a material such as the active material, electrolyte, and additives to a larger scale of region such as cell manufacturing and charging protocols (Fig. 5.3). In addition to the rational material design that can lower the kinetic limits which was conducted in this study, research that can control variables in other scales of battery design that may occur under the fast charge conditions is needed; furthermore, an integrated study that brings these different scale studies together is also needed to ultimately achieve a next-generation energy storage system. From the most foundational materials to the most practical applications, research must span every aspect of the battery, aiming to enhance cycle life and safety and reduce the cost and charging time. I hope that, with the suggested views, corresponding design guidelines, and experimental methods for fast-charging anode materials, this research could spark new groundbreaking research in this important field.

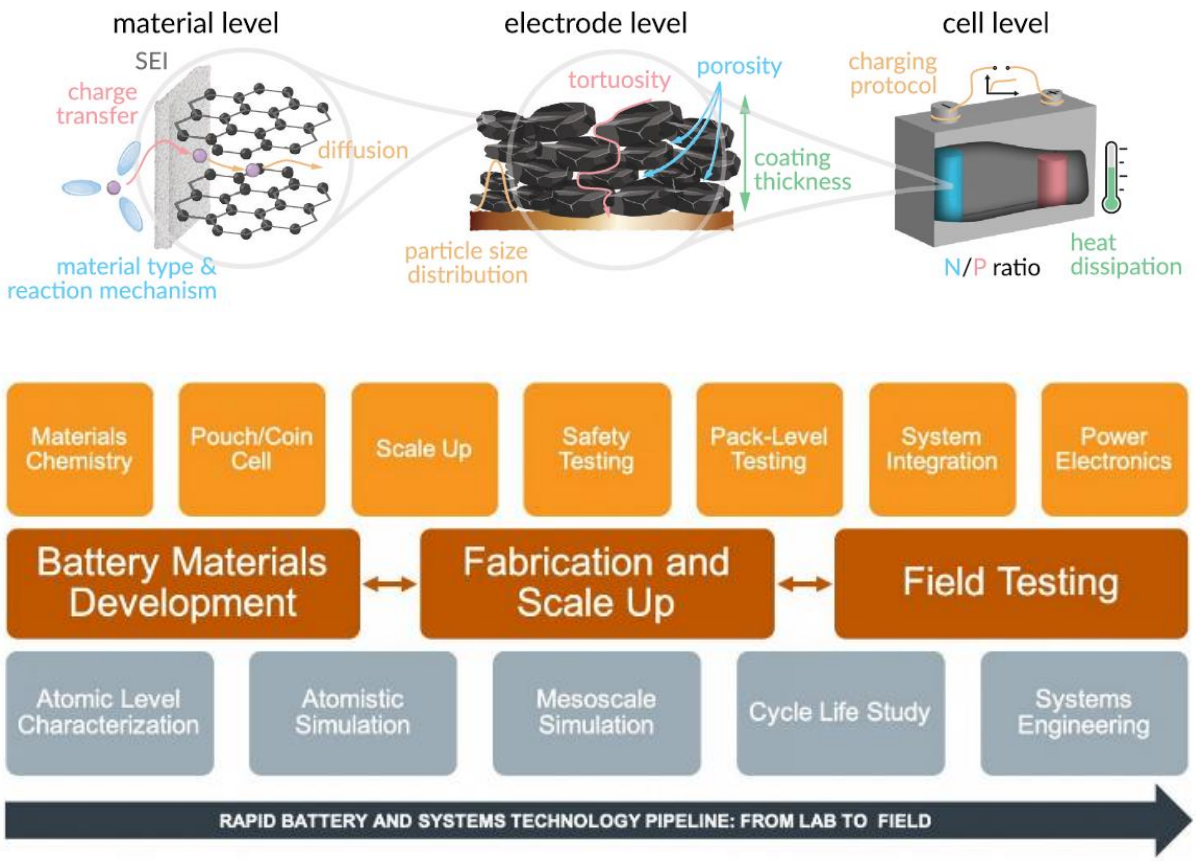

Figure 5.3 Various scale in battery science; from material level to cell level

References

[1] K.-H. Chen, V. Goel, M.J. Namkoong, M. Wied, S. Müller, V. Wood, J. Sakamoto, K. Thornton, N.P. Dasgupta, Enabling 6C Fast Charging of Li-Ion Batteries with Graphite/Hard Carbon Hybrid Anodes, Advanced Energy Materials 11(5) (2021) 2003336.

[2] T. Gao, Y. Han, D. Fraggedakis, S. Das, T. Zhou, C.-N. Yeh, S. Xu, W.C. Chueh, J. Li, M.Z. Bazant, Interplay of Lithium Intercalation and Plating on a Single Graphite Particle, Joule 5(2) (2021) 393-414.

[3] L. Borchardt, D. Leistenschneider, J. Haase, M. Dvoyashkin, Diffusion: Revising the Concept of Pore Hierarchy for Ionic Transport in Carbon Materials for Supercapacitors (Adv. Energy Mater. 24/2018), Advanced Energy Materials 8(24) (2018) 1870108.

[4] M. Weiss, R. Ruess, J. Kasnatscheew, Y. Levartovsky, N.R. Levy, P. Minnmann, L. Stolz, T. Waldmann, M. Wohlfahrt-Mehrens, D. Aurbach, M. Winter, Y. Ein-Eli, J. Janek, Fast Charging of Lithium-Ion Batteries: A Review of Materials Aspects, Advanced Energy Materials 11(33) (2021) 2101126.

국문 초록

무분별한 화석 연료의 사용과 그로 인한 자원 고갈에 따라 화석 연료를 대체할 수 있는 에너지를 효율적으로 저장, 관리할 수 있는 고성능 에너지 저장 시스템의 개발은 현 세대의 핵심 과제로 꼽혀왔다. 다양한 에너지 저장 시스템 중 리튬 이온 이차 전지로 대표되는 전기화학 기반 에너지 저장 시스템은 그 응용 분야가 다양하여 가장 널리 연구되고 있다. 그러나, 스마트폰과 같은 소형 전자 기기에서 거대한 전기 저장 스테이션 및 전기 자동차로 그 응용 분야가 확대되어가는 기로에서, 더 짧은 시간에 더 많은 용량의 에너지를 공급하는 급속 충전은 해결해야 할 가장 중요한 문제 중 하나이다. 급속 충전 조건에서는 활물질 내 전기화학종의 이동능 저하로 인해 특히 음극에서의 성능 저하가 심각하다. 지금까지 음극 재료로 널리 사용되고 있는 흑연은 낮은 산화 환원 전위에 의한 여러 부 반응, 느린 확산 속도와 높은 굴곡도 등으로 인해 속도 특성과 사이클 안정성이 좋지 못하고 이론 용량 또한 높지 않아 차세대 급속 충전용 음극재로 적합하지 않다. 이에 따라, 급속 충전 조건에서도 높은 전기화학적 성능을 발현하기 위한 음극재 개발에 많은 노력들이 있어왔다.

1부에서는 에너지 저장 시스템 및 소재 개발에 대한 기본적인 이론들을 정리하였다. 전기화학종의 이동 특성과 음극재의 공간 특성 간의 상관관계의 관점으로 기존에 보고된 연구결과들에 대한 재해석을 통해 현재의 접근 방식의 한계점을 도출하고 이를 극복하기 위한 시도로써 본 연구의 목표와 범주를 설정하였다. 이를 통해 1차원 구조의 탄소 나노 섬유를 설계하여 급속 충전 조건에서 전기화학

종의 재료 내 이동능을 개선하는 방안을 제안하였으며, 빠른 전기화학종의 이동에 용이한 형태학적 특성으로 기공이나 이온 채널과 같은 다양한 ‘공간’을 탄소 나노 섬유에 도입하는 방안을 제시했다.

2부에서는 빠른 전기화학종의 이동이 가능한 탄소 나노 섬유를 합리적으로 설계하기 위한 이론적 접근을 다루었다. 이동 특성을 향상시키기 위해 충전 환경에 따른 리튬 이온의 동적 크기를 계산하고 용매화된 리튬 이온이 이동하는 공간의 유효한 크기와 접근 용이성과 같은 공간 특성에 대해 다루며, 급속충전 환경에서의 전기화학종의 특성과 음극재의 공간 특성 간의 상관관계를 밝혔다.

3부에서는 2부에서 제시된 재료 설계 가이드라인에 따라 탄소 나노 섬유를 설계 및 제조하고, 실제 공간 특성과 이동 특성, 그리고 전기화학 성능 간의 상관관계를 도출하여 앞선 이론을 검증하였다. 제3장에서는 빠른 전기화학종의 이동이 가능한 공간 특성을 탄소 나노 섬유에 도입하기 위해, 비혼화성 고분자 블렌드 전기방사법을 제시하였다. 고분자 블렌드에서의 상분리 거동을 플로리-허긴스 상호작용 파라미터 기반의 상분리도를 통해 예측하였으며, 예측된 각각의 상이 전기방사되어 나노 섬유로 연신 되었을 때의 형태를 음극재 관점에서 해석하여 빠른 전기화학종 이동이 가능한 공간 특성을 설계하였다. 준안정 상을 극대화하여 섬유 내 용매화된 리튬 이온 채널을 만드는 획기적인 방법이 제안되었으며 이러한 공간 특성과 실제 이동 특성 간의 상관관계 도출을 통해 급속 충전에 적합한 음극재 설계 가이드라인을 제시하였다.

제4장에서는 이전 장에서 도출된 효율적인 이온 이동이 가능한 형태에서 더 나

아가, 빠른 전자 이동과 그에 따른 전기화학 반응의 극대화까지 이끌어 낼 수 있는 재료로써, 탄소 나노 튜브 (CNT)가 고밀도로 정렬된 다공성 탄소 나노 섬유 복합체를 구현하여 재료의 공간 특성과 이온, 전자에 의한 전기화학 성능 간의 상관관계를 탐구하였다. 전기화학종의 이동을 위한 채널에서 반응을 위한 표면까지, 공간을 계층적으로 나누어 접근하여 각각 코어 쉘 구조에 의한 채널 형성과 활성화를 통한 표면 개질을 통해 공간 특성이 전기화학 반응에 미치는 영향을 도출하였다. 또한, 탄소 나노 튜브의 도입을 전기 전도도 향상뿐만 아니라 재료의 공간 특성 개질 관점에서 새로운 관점으로 분석하였다.

요약하면, 본 연구는 급속 충전 환경에서 에너지 저장 재료의 성능 발현과 관련된 변수와 이에 영향을 줄 수 있는 재료의 공간 특성에 대한 이론적 고찰을 통해 빠른 전기화학 종 이동이 가능한 음극재 설계 가이드라인을 제시하였다. 이를 적용하여 빠른 이온과 전자 전달이 가능한 탄소 나노 섬유를 설계하였고, 실제 공간 특성과 이동 특성의 상관관계, 그리고 전기화학 성능으로의 영향까지 검증하였다. 본 연구에서 제시한 음극재 설계 가이드라인은 전기화학종의 이동과 저장 반응의 극대화를 통해 이론적으로 예측되는 에너지 저장 성능과 급속 충전 환경에서의 성능 간의 간극을 극복하고 전기화학능을 향상시킬 수 있는 차세대 에너지 저장 재료 연구에 학문적으로나 실용적으로 큰 의의가 있다.

주요어: 에너지 저장 재료, 전기화학, 배터리, 전기 방사, 상 분리, 탄소 나노 섬유

학번: 2015-20864